War Against Biofilms: Magnetic Nanoparticles as Effective Shield Breakers

by

Jie Li

A Thesis Submitted to the Faculty of Graduate Studies of the University of Manitoba

in Partial Fulfillment of the Requirements of the Degree of

Master of Science

Department of Biosystems Engineering

University of Manitoba

Winnipeg, Manitoba, Canada

Table of Content

Acknowledgement

Foremost, I would like to express my sincere gratitude to my advisor Dr. Song Liu for the continuous support of my Master study and research, for his patience, motivation, enthusiasm, and immense knowledge. His guidance helped me in all the time of research and writing of this thesis. His trust and faith in my abilities made me successfully finish this Master program. I am appreciated the encouragement he gave to me and helped me built the strong confidence. It is very fortunately to have such a dedicated advisor, who worked with me, providing his scientific advice, effective training, and consistent patience throughout the whole study process.

Besides my advisor, I would like to thank my thesis committee: Dr. Johan van Lierop and Dr. David Levin for their encouragement, insightful comments, and beneficial suggestions on my project.

I thank my co-work lab mate, Rachel Alexandra Nickel for her effort in synthesizing iron-oxide magnetic nanoparticles, helpful assistance and the stimulating discussions through the whole experimental process.

My sincere thanks also goes to Dr. Jiandong Wu for his efforts in confocal microscopy test used in this study.

Experimental Acknowledgments

I would like to thank my co-work partner Rachel Alexandra Nickel for her assistance in nanoparticle synthesis and helped with collection and analysis of the TEM and XRD results. She also contributed to test the hyperthermia curve of the alternating magnetic field. And she gave me a lot of useful help during the whole project process as well as many stimulating discussions; she was key to the success of our project.

I would like to thank Dr. Jiandong Wu, for the many hours spent helping us to do the confocal microscopy tests. Finally, I would like to thank Dr. Kim Seungil for the zeta-potential measurements of the nanoparticles samples.

Abstract

Biofilm formation on medical devices can cause persistent infections. The main feature of biofilms is their self-produced extracellular polymeric substances (EPS) that act as a protective shield to prevent biocide penetration. Iron oxide magnetic nanoparticles (MNPs), synthesized through a simple process, were used as "shield breakers" to damage the biofilm matrix and cause biofilm detachment. The Methicillin-resistant *Staphylococcus aureus* (MRSA) strain was used to demonstrate the efficacy of MNPs. The highest logarithmic reduction (4.71 log) of *S. aureus* biofilm was achieved after treatment with 30 mg/mL of 11 nm MNPs under rotating magnetic field for 15 minutes. MNPs caused strong mechanical disruption to the matrix and led to biofilm dispersal. Both alternating and rotating magnetic fields improved the effect of MNPs on biofilm damage. The increased MNPs solution temperature produces by hyperthermic effect in the AC field while the MNPs caused physical damage on biofilms in rotating magnetic field.

List of Tables

List of Figures

clinical strains cultured biofilms. The first and second columns from the left show biofilms that were washed three times with 200 μL DI water before contact with 0.1% crystal violet solution; the third columns biofilms show without washing and the biofilms in the last columns were gently immersed in water three times before staining.

Figure 18. The image (a) presents the crystal violet stain results for three standard and one non-standard biofilm after incubating for 48 hours with 2 mL 1% glucose TBS and (b) of four kinds non-standard biofilms CV test results. The first column (on the left) shows staining results of biofilms that were gently immersed in DI water for three times before contact with 0.1% crystal violet solution. The second column shows biofilms without washing and the last two columns biofilms that were washed three times with 200 μL DI water before treatment.

Figure 19. Image of crystal violet staining test of MRSA (ATCC 33592) stain after 24-hour growth and three washes

Figure 20. The ESEM images of control biofilm (without being exposed to MNPs). Note: The biofilm strain is MRSA. (ATCC 33592), and cultured with 1% glucose TSB and grown for 24 hours. The concentration of the bacteria is around 10^9 cfu/mL.

Figure 21. (a) The treatment solutions were collected of the 2 mL nanoparticles solution after contact with biofilm for 15 min under no field condition, alternating and rotating magnetic field. After treatment with the biofilms and collection of the treatment solution, the films were washed six times by using 200 μL DI water to remove the residual nanoparticles. (b) These washing solutions (~1.2 mL) were collected in 15 mL test tubes.

1. Introduction

1.1. Healthcare Associated Infections (HAIs)

Healthcare-associated infections (HAIs) are a most serious public health problem globally. The European Centre for Disease Prevention and Control (ECDC) estimates that approximately 4 million patients annually in all EU Member States acquire HAIs. Approximately 37,000 deaths result directly from these infections in the EU each year. An estimated 25,000 of deaths are due to the most common multidrug-resistant bacteria, *Staphylococcus aureus*, *Enterobacteriaceae,* and *Pseudomonas aeruginosa* [1]. In 2002, the Centers for Disease Control (CDC) estimated approximately 1.7 million HAIs (5 to 10 percent of hospitalized patients) occurred in U.S. hospitals each year, resulting in 99,000 deaths [2], making HAIs the fifth leading cause of death in US acute-care hospitals [3].

HAIs are not only one of the leading causes of death in the United States, but also a significant economic concern, as the overall direct cost of HAIs to hospitals in the USA ranges from US $28 billion to $45 billion [4]. The most commonly reported HAIs involve ventilator-associated pneumonia (VAP) and lower respiratory tract infections (22.8% of cases), catheter-associated urinary tract infections (CAUTIs; 17.2% of cases) and surgical-site infections (SSIs; 15.7% of cases) [5]. Moreover, the medical equipment or devices are the second most common sources of infectious agents causing HAIs, described in a scientific review of 1,022 outbreak investigations [6]. Biofilms are at the core of the problems of medical device related HAIs. To decrease the risk of HAIs from

medical devices, it is important to develop highly efficient methods to disinfect medical devices after use.

1.2. Biofilms

1.2.1. Structure

Biofilms have been defined as communities of microorganisms attached to a surface, producing extracellular polymeric substances (EPS) and exhibiting an alternate phenotype compared to corresponding planktonic cells [7]. Through biofilms, bacteria and fungi adapt to their environment, allowing them to attach to surfaces in a complex three-dimensional structure. The self-produced EPS of the biofilm act as a shield to protect the biofilm-associated microbial cells so they become tolerant and resistant to external threats, including antibacterial agents [8]. The genotypic and phenotypic characteristics of cells in biofilms are different from those of their free-floating counterparts, and these differences make them strongly tolerant and resistant to antibiotics which resulting in the failure of standard antibiotics to penetrate the biofilms fully [9], or to eradicate or harm bacteria of all species and metabolic states [10].

Depending on the bacteria type, micro-colonies consist of 10-25% of cells and 75-90% of EPS matrix [11]. The EPS matrix consists mainly of polysaccharides, proteins, and lipids. However, contrary to common belief, the EPS also includes extracellular deoxyribonucleic acid (DNA)[12]. EPS biopolymers are highly hydrated and the matrix keeps the biofilm cells together, retains water and determines the life conditions of the biofilm cells, affecting their porosity, density, water content, sorption properties,

hydrophobicity, and mechanical stability [13].

Between micro-colonies, the matrix has been found to contain channels that help distribute nutrients and water [14]. This matrix also interacts with the environment, e.g., by attaching biofilms to surfaces through its sorption properties, and allows sequestering of dissolved and particulate substances from the environment, providing nutrients for biofilm organisms [15]. Additionally, the EPS matrix can protect the biofilm cells from various negative environmental conditions, such as Ultraviolet (UV) radiation, abrupt changes in pH values, and dessication [16]. If biofilms could be metaphorically called a "city of microbes" [17], the EPS represents the "houses of the biofilm cells."

1.2.2. Biofilm development

Biofilm formation and maturation are sequential, dynamic, and complex processes, that depend on the substratum, the medium, the intrinsic properties of the cells, signaling molecules, cellular metabolism, and genetic control [18, 19]. The process of biofilm formation begins with a conditioning layer of organic or inorganic matter on a surface. This conditioning layer alters the surface characteristics of the substratum and eventually favors microorganisms colonizing a surface [20]. The biofilm formation process comprises five distinct steps (see Figure 1):

(i) Initial reversible attachment of bacterial cells via weak interactions (such as van der Waals forces) with an abiotic or biotic surface [18, 21];

(ii) Irreversible attachment to the surface via hydrophilic/hydrophobic interactions by means of several attachment structures (flagella fimbriae, lipopolysaccharides, or adhesive proteins) [18, 21];

(iii) Proliferation and production of a self-produced EPS matrix composed mainly of polysaccharides, proteins, and extracellular DNA, and ultimately the biofilm architecture [22, 23];

(iv) Formation of a mature biofilm that contains water channels that effectively distribute nutrients and signaling molecules within the biofilm [24];

(v) Detachment of biofilm cells individually or in clumps due to intrinsic or extrinsic factors. This dispersal enables biofilms to spread and colonize new surfaces [25].

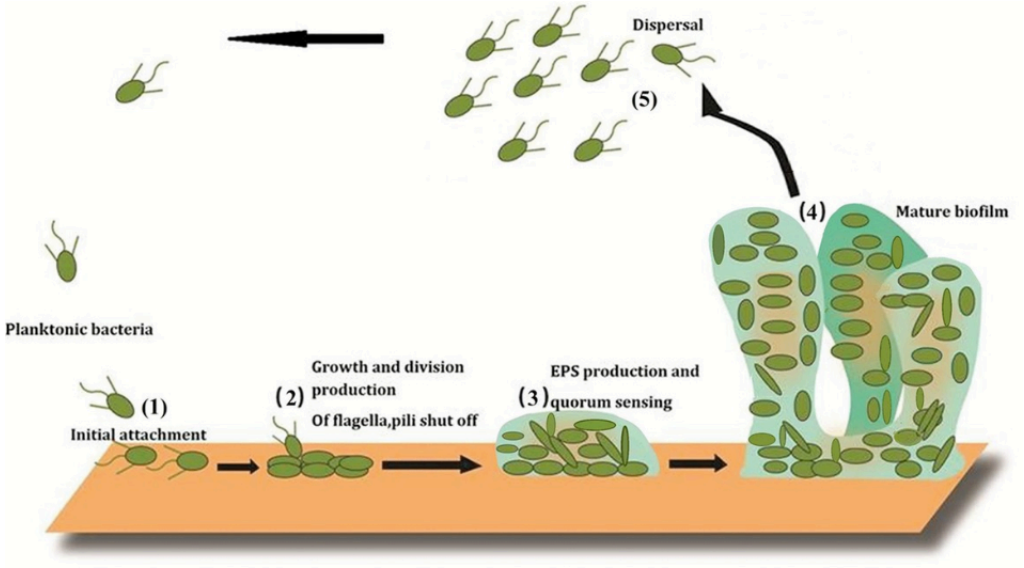

Figure 1. Representation of a developmental model of biofilm formation. Biofilm formation comprises five distinct stages identified as: 1) initial attachment; 2) growth;

division and production of flagella, pili shut off; 3) EPS production and quorum sensing; 4) mature biofilm formation; and 5) dispersal. From Sadekuzzaman et al. [32].

Biofilms are affected by environmental factors, such as nutrient availability and hydrodynamics. They are polymorphic and can adjust their structures to changes in the level of nutrients, as demonstrated by experiments with different glucose concentrations [26]. When glucose concentrations are high, micro-colonies grow quickly and the biofilm thickness increases significantly. When glucose concentrations are decreased, biofilm biomass is reduced and the former structure is restored. The excess carbon provided by the increased number of sugar molecules promotes synthesis of the biofilm matrix in the outer layer of the biofilm [18].

1.2.3. Disinfecting biofilm contaminated reusable medical devices

Biofilms play a pivotal role in HAIs, especially those related to the medical devices, such as intravascular catheters and urinary catheters. HAIs occur as a result of infection by a number of agents, most commonly bacteria, but also fungi, parasites, viruses and prions; the most widely publicized source of HAIs is the hospital 'superbug' Methicillin-resistant *Staphylococcus aureus* (MRSA), which is a common cause of septicaemia or bacteraemia in clinical settings [27].

The prevalence of healthcare-associated MRSA continues to increase. A 2006 study found healthcare-associated MRSA in the U.S. to be 46.3 per 1000 hospital inpatients [28]. In 2005, the number of hospital HAIs due to MRSA in the United States alone was 368,600—a 10-fold increase from 1995 [29]. Importantly, MRSA is responsible not only

for localized infections, such as wounds or postoperative infection, but also for prosthetic infection through the use of catheters, endotracheal tubes, and other biomaterials [30]. Several conventional approaches have been used to combat biofilms including physical and/or mechanical removal, chemical removal, and antimicrobials, sanitizers, or disinfectants to kill biofilm organisms [31].

However, one of the most important characteristics of biofilms is their increased tolerance to antimicrobial agents [32]. It has been shown that biofilms can tolerate concentrations of antibiotics and disinfectants up to 100-1000 times higher than planktonic cells can tolerate [33]. The mechanisms involved in the increased drug resistance of biofilms presumably relates to the slow or incomplete penetration of antimicrobial agents through the biofilm matrix [34]. Thus, the presence of the matrix undoubtedly retards the diffusion of antimicrobial agents. Additionally, cells deep within the EPS show reduced metabolic activity as a defense mechanism to chemical agents [35]. Overall, the unique physiological adaptions of biofilms make them extremely difficult to eliminate.

The incidence of HAIs increase as more medical devices are associated with biofilm growth. Although there are guidelines that highlight procedures for high-level disinfection and reprocessing of medical devices, as emphasized by different institutions and agencies such as the Public Health Agency of Canada and Canadian Association of Gastroenterology [36], biofilms on the surface of reusable medical devices cannot be easily removed. The design features commonly associated with these devices are

complex, creating significant challenges for cleaning. Also, many of these devices have optics and electrical components that must be considered in both cleaning and sterilizing techniques, as these components cannot be immersed in cleaning or disinfection solutions [37].

Additionally, the complex design features of reusable medical devices provide an increased opportunity for biofilm accumulation: the primary risk factor for infection. For example, digestive endoscopy is an important technique for the diagnosis and treatment of digestive system diseases. As with many other high-precision medical devices, a digestive endoscope is a complex, reusable device, made of special materials [38]. The device must undergo high-level disinfection after each use to ensure medical safety. However, according to current literature, biofilm formation on endoscopic examination tubes has led to failure of the cleaning and disinfecting processes and has been the cause of infection. According to a study conducted by Lijun Qiu et.al claimed that a polluted pancreatic and biliary endoscope was cleaned and disinfected multiple times after surgery using the standard procedure, but still tested positive for *Pseudomonas aeruginosa* culture [39].

1.2.4. Currently state-of-art of treating biofilm

As mentioned above under the protection of biofilm, microbial cells in the biofilm become tolerant and resistant to antibiotics, which increases the difficulties for the clinical treatment of biofilm infections. Clinical observations and experimental studies indicated clearly that antibiotic treatment alone is in most cases insufficient to eradicate

biofilm infections [40]. Therefore, to effectively treat biofilm infections currently becomes important and urgent for clinicians. As a result, novel therapeutic solutions other than the conventional antibiotic therapies are in urgent need. Below, we list a few of the recent researches in the discovery of alternative approaches to prevent or treat biofilms.

1.2.4.1. Biosurfactants (BSs)

Biosurfactants (BSs) have become a novel choice to disinfect the biofilm formation on medical devices. The strong dispersal, high antimicrobial, and anti-adhesive properties of BSs make them suitable agents for eradication of biofilms [41]. BSs can modify the surface characteristics of bacterial cells and reduce their adhesive properties. Microbial surfactants or biosurfactants are a low-molecular-weight heterogeneous group of amphiphilic surface-active compounds (produced by microbes) containing a hydrophilic moiety (polar or nonpolar) and a hydrophobic moiety (lipid or fatty acid), either on the cell surface or secreted extracellular [32].

Lipopeptides are one of the largest groups of biosurfactants that can effectively disperse microbial biofilms. This group includes surfactins, polymixins, fengycins and fusaricidins [42, 43]. Most interestingly, the polymixins were able to inhibit the formation of mixed species biofilms such as self-assembling marine biofilm (SAMB) in co-incubation assays by 99.3 % and disrupt previously established mixed SAMB by 72.4 % [44]. Fengycin-like peptides have been reported to be involved in the inhibition of biofilms causing up to 90% dispersion of Gram-positive *S. aureus* biofilms [45] and up to 97% dispersion of Gram-negative *Escherichia coli* biofilms [46].

Other biosurfactants, like pseudofactin and surfactin, have also been documented to produce an effective dispersal of biofilms grown on untreated surfaces, and has been shown to cause a marked inhibition of biofilms growth [47]. BSs offer several advantages over synthetic surfactants: BSs are diverse, biodegradable, have low toxicity and the potential for highly selective, specialized functions [42]. However, production of BSs is still restricted by the high cost of production [43].

1.2.4.2. Silver nanoparticles (AgNPs)

Silver nanoparticles have recently received an increased attention for their antimicrobial effects and possible clinical applications. The antibacterial properties of silver have long been known and nanoparticles of this metal (AgNPs) are believed to be less toxic than silver ions [48]. Silver nanoparticles probably have multiple mechanisms of antibacterial action, among them the most important one was suggested that AgNPs release Ag+ ions in the presence of water, and nanosilver affects bacterial membrane permeability by attaching to the cell membrane surface and modifying the cell potential. Furthermore, AgNPs have been shown to interact with bacterial membrane proteins, intracellular proteins, phosphate residues in DNA, and to interfere with cell division, leading to bacterial cell death. According to Kalishwaralal's group reported using 100 nM of AgNPs against *P. aeruginosa* and *S. epidermidis* biofilms found resulted in a 95–98 % reduction in biofilm [49].

Despite the strong anti-biofilm effect of AgNPs they still have challenges for the anti-biofilm application. The application of AgNPs as an effective antimicrobial agent

should not cause microbial resistance even after long-term usage. However, there have been reports concerning bacterial resistance to silver compounds determined by genes carried on plasmids. The widespread usage of silver nanoparticles (e.g. as a component of disinfectants) might promote the spread of silver-resistant bacterial strains [50]. One the other hand, it should be noted that the biosafety of silver nanoparticles is currently uncertain. Some of the mechanisms mediating the biological activity of AgNPs are not specific for the cells of bacteria or fungi, but are conserved in many organisms, potentially also in humans. So far, there have been very few reports on the effects of AgNPs on human health [142].

1.2.4.3. Photo-inactivation

The other novel approach to treat biofilms is the use of photo-inactivation where light is used to either directly damage bacteria by exciting intracellular porphryins, which release reactive oxygen species, or to activate an inert photo-sensitive dye that releases toxic reactive oxygen species [132]. This approach promises to be relatively cheap and non-toxic as a therapy such as blue light (wavelengths between 400 and 470 nm) is able to exert an antimicrobial effect [133]. One particular advantage of the use of light-based antimicrobial therapies is equivalent activity against both drug resistant and sensitive pathogens, as the mechanisms of antibiotic resistance do not affect the efficacy of photo inactivation [134]. Blue light in particular has been studied for activity against a range of bacteria and fungi and has been found to be efficacious [135]. There is *in vitro* evidence for activity against *S. aureus,* including methicillin resistant *S. aureus* (MRSA) strains, *E.*

coli, *S. epidermidis* and *P. aeruginosa*. [135,136].

A recent study specifically looked at the efficacy of blue light against biofilms and found 405 nm light was effective at killing the bacteria of a range of important nosocomial pathogens within biofilms *in vitro* [137]. The time taken to achieve a significant reduction in viable cells within the biofilm varied between species with illumination times between 15 and 60 min being required [137]. However, although UV light has long been known to be antimicrobial and have many advantages, it is still not suitable for application to humans due to mutagenic properties [138].

1.2.5. Characterization of biofilms

1.2.5.1. Crystal violet

The Gram staining method, named after the Danish bacteriologist who originally devised it in 1882 (published 1884), Hans Christian Gram, is one of the most important staining techniques in microbiology. It is almost always the first test performed for the identification of bacteria. The primary stain of the Gram method is crystal violet (CV), a basic protein dye that stains the surface of negatively charged molecules (i.e., peptidoglycan) and the extracellular matrix of polysaccharides [51].

Gram staining is based on the ability of the bacteria cell wall to retaining the crystal violet dye during solvent treatment. The cell walls for Gram-positive microorganisms have a higher peptidoglycan and lower lipid content than gram-negative bacteria. After the bacteria cell walls are stained by the crystal violet, Iodine is added as a mordant to form a crystal violet-iodine complex so that the dye cannot be removed easily. Cells that

die lose their adherence and are subsequently lost from the population of cells, reducing the amount of crystal violet staining in a culture [52].

1.2.5.2. Ultraviolet and visible spectroscopy

Spectroscopy is a technique that measures the interaction of molecules using electromagnetic radiation. Light in the near-ultraviolet (UV) and visible (vis) range of the electromagnetic spectrum has energy of about 150 – 400 kJ/mol. The energy of the light is used to promote electrons from the ground state to an excited state [53]. A spectrum is obtained when the absorption of light is measured as a function of its frequency or wavelength. Molecules with electrons in delocalized aromatic systems often absorb light in the near-UV (150–400 nm) or the visible (400–800 nm) region [54].

Absorption spectroscopy is usually performed with molecules dissolved in a transparent solvent, such as in aqueous buffers. The absorbance of a solute depends linearly on its concentration and therefore absorption spectroscopy is ideally suited for quantitative measurements [55]. The wavelength of absorption and the strength of absorbance of a molecule depend not only on the chemical nature but also on the molecular environment of its chromophores. Absorption spectroscopy is therefore an excellent technique for following ligand-binding reactions, enzyme catalysis and conformational transitions in proteins and nucleic acids [55]. Spectroscopic measurements are very sensitive and nondestructive, and require only small amounts of material for analysis.

Absorbance at 260 nm. The concentrations of nucleic acids in solution are routinely

determined from their strong absorbance at 260 nm. Nucleic acids absorb UV light at 260 nm due to the aromatic base moieties within their structure. Purines (thymine, cytosine and uracil) and pyrimidines (adenine and guanine) both have peak absorbance at 260 nm, thus making it the standard for quantifying nucleic acid samples [56].

Absorbance at 280 nm. The 280 nm absorbance is measured because this is typically where proteins and phenolic compounds have a strong absorbance. Aromatic amino acid side chains (tryptophan, phenylalanine, tyrosine and histidine) within proteins are responsible for this absorbance. Similarly, the aromaticity of phenol groups of organic compounds absorbs strongly near 280 nm [57].

Absorbance at 230 nm. Many organic compounds have strong absorbance near 225 nm. In addition to phenol and chaotropic salts, the peptide bonds in proteins absorb light between 200 and 230 nm [58].

1.2.5.3. Confocal laser scanning microscopy

A Confocal Laser Scanning Microscope (CLSM) is an optical microscope equipped with a laser beam that is particularly useful in biology and life sciences to study thick samples. Confocal laser scanning microscope technology makes it possible to scan a thick biological sample, e.g. a microbial biofilm, by processing images, line by line, in X, Y and Z axes so confocal microscopy is the method of choice to study interfacial biofilms and acquire three-dimensional data of the biofilm structure [59].

For confocal microscopy, the BacLight Live/Dead bacterial viability kit (L-7007; Molecular Probes, Eugene, OR) was used to stain bacteria in biofilms grown on glass

coverslips. The kit contains (i) Syto 9, a membrane-permeable fluorophore that stains both living and dead cells in green by intercalation in their DNA, and (ii) propidium iodide, which enters only damaged cells, causing an attenuation of the Syto 9 signal in dead cells only and making them appear red when a dual-emission filter is used [60].

1.3. Iron-oxide Magnetic Nanoparticles

The efficient treatment of biofilm infections needs a well-established multidisciplinary collaboration. Over the past decade, interest in nanomedicine-based approaches to combat difficult biofilm infections has grown rapidly due to their many advantages over conventional treatments. Nanomaterial development is now viewed as a promising strategy for controlling or treating biofilms on medical devices and implants [61]. Recently, iron oxide magnetic nanoparticles (MNPs) (diameters between about 1 and 100 nanometers [62]) have attracted extensive interest due to their unique properties, such as superparamagnetism, high specific surface area, easy separation methodology, and their potential applications in many fields [63].

The surface area-to-volume ratio of nanoparticles has a significant effect on nanoparticle properties. An increase in surface area, leads to an increase in chemically reactiveness. Magnetic nanoparticles, having sizes between 2 and 20 nm, tend to display superparamagnetism, meaning their magnetization is zero in the absence of an external magnetic field, and they can be magnetized by an external magnetic field source [64]. This property provides additional stability for magnetic nanoparticles in solutions.

MNPs also have very good biocompatibility and low cytotoxicity [65]. Due to their

low toxicity, superparamagnetic properties, and simple separation methodology, magnetic iron oxide (Fe_3O_4 and γ-Fe_2O_3) nanoparticles have attracted much attention and are especially interesting in biomedical applications such as diagnostic magnetic resonance imaging (MRI), thermal therapy, and drug delivery [66].

Due to their special superparamagnetic property, MNPs can be controlled and concentrated in the presence of a magnetic field so that they can be immobilized close to a target [67]. Superparamagnetic iron oxide nanoparticles are proposed as a potential treatment against antibiotic-resistant biofilms. These nanoparticles can be targeted to a treatment site using an external magnetic field, causing deep penetration in biofilm, spatial disruption and possible elimination of biofilm. Additionally, using an alternating magnetic field (AC field), the MNPs could act as a heat source to produce an effect of hyperthermia, potentially reducing the viability of the bacterial community [68]. On the other hand, the movement of MNPs on the biofilms under rotating magnetic field could lead to biofilm detachment and cause mechanical damage to the film matrix. In additional, MNPs are inexpensive to produce, physically and chemically stable, biocompatible, and environmentally safe [69].

1.3.1. Preparation of Iron-oxide Nanoparticles

MNPs with appropriate surface chemistry can be prepared by various methods, such as wet chemical, dry processes, or microbiological techniques [70-73]. Among these methodologies, chemical-based synthesis methods are adopted mainly due to low production costs and high yields. In general, magnetites are synthesized by adding a base

to an aqueous mixture of Fe^{2+} and Fe^{3+} chloride at 1:2 molar ratios, resulting in black color precipitate [74]. The chemical reaction of Fe_3O_4 precipitation is given in equations 1 and 2. The overall reaction is written as follows [75]:

$$Fe^{2+} + 2Fe^{3+} + 8OH^- \rightarrow Fe_3O_4 + 4H_2O \qquad (1)$$

Under oxygen-free environment, a complete precipitation of Fe_3O_4 is likely between pH 9 and 14, maintaining a molar ratio of Fe^{3+}: Fe^{2+} (2:1). Fe_3O_4 might also be oxidized as:

$$Fe_3O_4 + 0.25O_2 + 4.5H_2O \rightarrow 3Fe(OH)_3 \qquad (2)$$

The physical and chemical properties of nanoparticles may vary depending upon the conditions. To prevent iron nanoparticles from oxidation and agglomeration, Fe_3O_4 nanoparticles are usually coated with organic or inorganic molecules [76].

1.3.2. Surface coating of Iron-oxide magnetic nanoparticles

Stabilization of the surface coating of iron oxide nanoparticles is an important issue because the iron oxides with bare surface tend to agglomerate due to strong magnetic attraction among particles and van der Waals forces [77]. The high surface area to volume ratio of nanoparticles usually results in high rates of reactivity and colloidal instability compared to their bulk counterparts. Nanoparticles exhibit a tendency to agglomerate by strong magnetic dipole-dipole interactions [78]. Hence, one of the main problems of producing stable magnetic nanoparticles is to prevent agglomeration during the synthesis, and require a coating process by a shell on the MNPs surface. These coatings can consist of various types of molecules, for example inorganic molecules,

small organic molecules, polymers and proteins [79–82]. In this study we chose silica to coat the iron-oxide nanoparticles via alkaline hydrolysis of tetraethyl orthosilicate (TEOS) in the presence of MNPs. The advantages of silica coating are: 1) compatibility with many chemicals and molecules for bioconjugations; 2) ability to incorporate small molecules such as dyes and drugs, and even quantum dots; 3) ability to stabilize the nanoparticles; and 4) easy dispersion in aqueous or organic solution, even without surfactants [56].

1.3.3. Size of Nanoparticles

Small nanoparticles, in the range of 10 to 50 nm, are the best selection for biomedical applications. These nanoparticles have several benefits [83]:

(i) It is possible to improve colloidal stability and avoid aggregation by reducing magnetic interaction of nanoparticles. To obtain this, NPs should have superparamagnetic features. The particle size required to achieve superparamagnetism in Fe_3O_4 nanoparticles is widely estimated to be below 20 nm [123, 124]. Therefore reduction of size is necessary to achieve superparamagnetic properties;

(ii) The strength of the dipolar interaction depends on the distance between the spins. The effect is inversely proportional to the third power of distance ($1/r^3$). Therefore by reducing size, the dipolar interactions become small and the particle aggregation is decreased;

(iii) Small nanoparticles can avoid the precipitation;

(iv) Small nanoparticles have larger surface area for a certain volume, thereby improving the efficiency of the coating and targeting process;

(v) Small nanoparticles can be stable in water at pH = 7 [83].

1.3.4. Characterization of Magnetic Nanoparticles

For a better understanding of surface properties, comprehensive surface characterization techniques are necessary to measure such as surface morphology, size distribution of nanoparticles, and chemical composition [84]. Techniques employed to investigate MNPs include: X-ray diffraction analysis (XRD), Fourier transform infrared spectroscopy (FT-IR), transmission electron microscopy (TEM), scanning electron microscopy (SEM), zeta-potential measurements, and thermal gravimetric analysis (TGA) [84]. Detailed properties and advantages of some techniques are summarized in Table 1.

Table 1. The analytical techniques for the assessment of the physicochemical properties of MNPs

Modalities	Analyzed physical and chemical properties	Advantages
Zeta-potential	Stability concerning to charge on surface	Concurrent measurement of numerous particles.
IR ATR-FTIR	Bioconjugate Surface properties such as structure and conformation.	Rapid and cheap measurement. No or minimal sample preparation demands. Irrespective of sample thickness enhanced reproducibility.
SEM	Size and size distribution.	Simultaneous measurement of the size navigation and shape of NMs.
TEM	Shape heterogeneity. Size and size navigation. Dispersion. Accumulation.	With higher spatial resolution than SEM, direct measurement of the size transportation and shape of nanomaterials (NMs) occurs. For investigation of chemical composition and electronic structure of NMs. A lot of analytical techniques are paired off with TEM.
XRD	For crystalline materials, shape, size, and structure determination.	Well-organized modalities. At atomic level, high spatial resolution.

1.3.5. Magnetic hyperthermia

MNPs have also been proposed for hyperthermia applications, especially in cancer therapy. This new therapeutic concept, called magnetic hyperthermia (MH) [85] relies on the heat released by the MNPs exposed to an externally applied alternating magnetic field (AC) that is used to increase the temperature of the cancer cells to a level at which apoptosis can be initiated [125]. In fact, different approaches have been used to apply hyperthermia in tumor regions, but with harmful secondary effects in the healthy tissues. This is the case of many techniques involving laser, ionizing radiation and microwaves as tools to heat up malignant body tissues. Although these techniques are able to increase the intracellular temperature to cellular death, they can also provoke harmful side effects such as ionization of genetic material or lack of selectiveness in radiation and microwave therapies, respectively, and so affect the surrounding healthy tissues [86].

However, nanotechnology has just provided a novel and original solution to this problem using MH. Through MH, localized heat can be induced remotely through the magnetic energy losses of MNPs under an oscillating magnetic field [86]. In other words, the ability of some MNPs to transform electromagnetic energy into heat allows the temperature increase in a well-defined region of the human body, for example, where tumor cells and the nanoparticles are located.

The specificity of this technique is achieved by the higher sensitivity of the tumor cells to temperature increases above 42°C, temperatures at which the natural enzymatic processes that keep the cells alive are destroyed, hence allowing their selective killing

[87]. This allowing a more localized treatment and eradication of the malign cells whereas the harmful secondary effects induced on the healthy ones would be significantly reduced.

Among all types of MNPs developed so far, Fe_3O_4 superparamagnetic iron oxide nanoparticles are the only type of MNPs approved for clinical use by the US Food and Drug Administration [88] and have already been tested *in vivo* for clinical MH therapy [89] due to their excellent biocompatibility and stability. Figure. 2 shows a schematic representation of the important parameters (i.e. optimization of the magneto-structural properties of MNPs, magnetic dipolar interaction effects, reliability of the methods used in magnetic hyperthermia measurements) that need to be addressed in designing iron-oxide MNPs with optimized heating efficiency for various MH applications (e.g. magnetic imaging-guided hyperthermia, magnetic actuated drug delivery, thermal cancer therapy, biofilm eradication) [90].

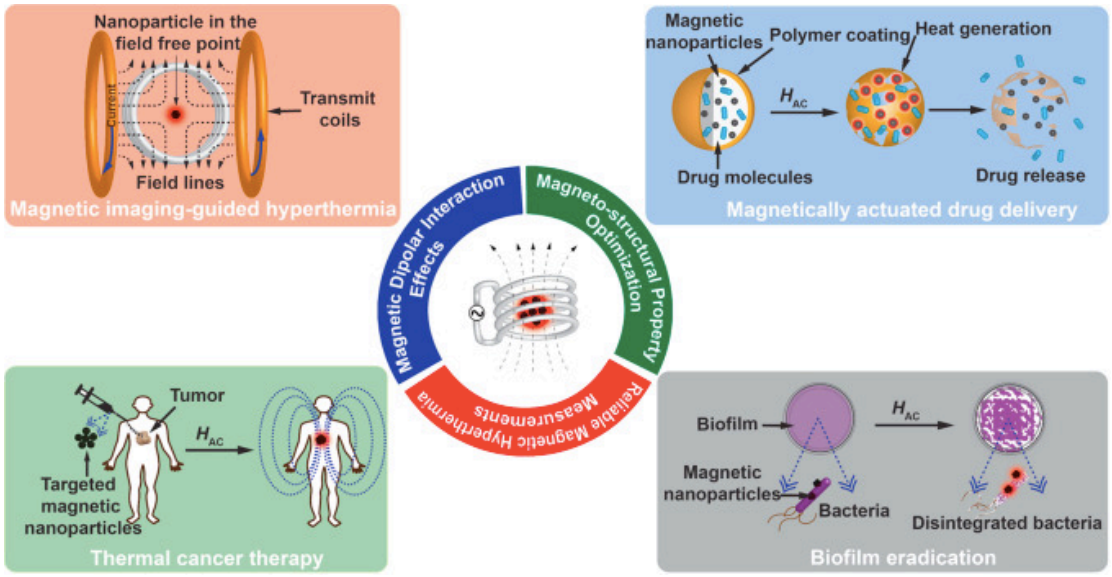

Figure 2. Schematic diagram illustrating the important parameters affecting the

efficiency of magnetic hyperthermia treatment and the different types of biomedical magnetic hyperthermia applications. From Abenojar et al. [80].

While MH has been clinically approved for brain tumor treatment in Europe, it is still not widely utilized in clinics [91]. In particular, MH has not been approved as a treatment approach in hospitals in the USA and other parts of the world. The lack of widespread adaptation of this treatment modality can be partly attributed to gaps in the development of optimized magnetic nanoparticles hyperthermia agents [90].

1.4. Quaternary Ammonium Compounds

Quaternary ammonium compounds (QACs) were first introduced in 1917 and are probably the best known cationic surface-active agents [92]. Their general formula is shown in Figure 3. The R groups may be the same or different alkyl or aryl groups; also, the R groups can be connected [92].

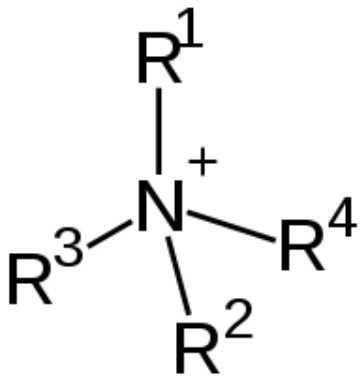

Figure 3. General structure of quaternary ammonium compounds

The enhanced efficacy of substituting long-chain alkyl moieties to quaternary ammonium cations (quats) was reported by Domagk in 1935 [93]. The recognition of the potential to alter antimicrobial and toxicological properties through chemical substitution

has led to the development of a range of quats structures. The two types of quats that are most prevalent in disinfectants are alkyldimethylbenzylammonium chloride (ADBAC), and dialkyldimethylammonium chloride [94]. The efficacy of quats against specific bacteria varies with the hydrocarbon chain length. Maximum efficacy for ADBAC quats is obtained with chain lengths between C12 and C16, while for dialkyl quats this occurs at C8 and C10 chain lengths. Most of the commercially available quats fall within this range [95].

QACs as the active ingredient are among the most extensively used. The advantages of quats are good stability and less toxicity, surface activity and compatibility with cleaner formulation ingredients, and lack of odor [96]. QACs are considered low-level disinfectants, as defined by the US Centers for Disease Control and Prevention. They are effective against most vegetative bacteria and enveloped viruses, and some fungi [97]. The conditions necessary to attain disinfection with quats depend on concentration and contact time. Typical end-use concentrations will have from 0.05 to 0.2% quats, and require 10 min to achieve disinfection [98].

QACs are cationic biocides with a broad-spectrum antimicrobial activity that are widely used as antiseptics, disinfectants, and preservatives. The primary interaction between QACs and bacteria is electrostatic in nature. Cell membranes contain phospholipids which impart an anionic character to bacteria at pH above 3–4. Thus the negatively charged cellular membranes of most bacteria can be used as the target site of cationic biocides [99-101]. The antibacterial mechanism of biocide QACs, a class of

membrane-active cationic biocides, is believed to be through interference with the function of the cell membrane, resulting in leakage of intracellular components or disruption of the cell [102, 103].

1.4.1. Cetrimonium bromide

Cetrimonium bromide (CTAB) is one kind of quaternary ammonium salt. Their general structure is shown in Figure 4. It has been widely used in the synthesis of nanoparticles as a surfactant. As a surfactant, it plays a key role in nanoparticles synthesis by adsorbing to the surface of the forming nanoparticle and lowering its surface energy [104, 105]. Surfactants also help to prevent aggregation. CTAB is also one of the components of the topical antiseptic cetrimide [106]. The cetrimonium (hexadecyltrimethylammonium) cation is an effective antiseptic agent against bacteria and fungi.

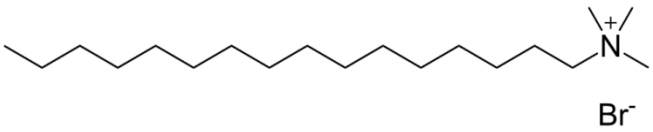

Figure 4. Structure of CTAB.

1.5. *N*-Chloramine

Currently, antibiotic resistance is a growing public health crisis. To address the development of bacterial resistance, the use of antibiotics have to be preserved for systemic applications in humans, and their use need to be minimized for topical application in wound infection control or for promoting animal growth. Possible

substitutes with low potential for developing resistance are active chlorine compounds that have been in clinical use for over 180 years [107]. *N*- chloramines have long-term stability in aqueous solution, effectiveness toward a broad spectrum of microorganisms, and are less corrosive than sodium hypochlorite. They are particularly efficacious, safe to humans, relatively cheap to synthesize, and environmentally friendly [108].

N-chloramine compounds contain one or more chlorine atom covalent bonds that are usually formed by the chlorination of imide, amide, or amine groups [109-110]. *N*-chloramine with nitrogen-chlorine covalent bonds in its structure is a typical oxidative agent, and the chlorine with "+1" oxidation state possesses a strong tendency to kill bacteria [111]. The antimicrobial action is considered to be a manifestation of a chemical reaction involving the transfer of oxidative chlorine from the *N*-chloramine to bacterial cells, followed by inhibition or even destruction of the bacteria's enzymatic and/or metabolic cell processes, resulting in the death of the bacteria [112]. Consequently, *N*-chloramine is used for this purpose in a wide variety of fields, including water purification systems, food storage and packaging, medical devices, hospitals, hygienic products, dental office equipment and household sanitation. [113].

2. Hypothesis and Objectives

Our hypothesis is that MNPs can cause mechanical disruption of the biofilm matrix and lead to the film dispersal. We also propose to increase the damage to the biofilm matrix using alternating and rotating magnetic field. Under an AC magnetic field, MNPs could act as a heat source to increase the temperature of the particle solution and produce a hyperthermia effect causing damage and detachment of the biofilm matrix. Additionally, because the biofilms are quite sensitive to shear stress, a rotating magnetic field could help the MNPs move around on a biofilm, causing mechanical damage and physical disruption. In addition, since the MNPs are nano-scale, they should be friendly to the surface of the medical device, leaving no visible damage after treatment.

It is predicted that the MNPs can damage the matrix of persistent biofilms, and the mechanical disturbance caused by MNPs, spatially manipulated by the alternating and rotating magnetic field could lead to not only effective physical disruption, but also biofilm dispersal. After the “shield” is broken, the biocide could kill not only the exterior but also the interior of the biofilm to increase the efficiency of the process.

The specific objectives of this study are:

1. Synthesize different sizes and shapes of MNPs;
2. Test the MNPs anti-biofilm efficiency by using 8 nm, 11 nm, and 70 nm MNPs coated with silica under alternating and rotating magnetic fields against MRSA (ATCC 33592) strain;
3. Design an antibacterial experiment using 0 °C, room temperature (RT), and 50 °C

MNPs coated with QACs and chlorinated with *N*-chloramines to treat the MRSA (ATCC 33592) strain;

4. Determine the mechanism of the positive effect of MNPs on biofilm treatment.

3. Materials and Methods

3.1 Chemicals and reagents

All reagents and solvents were used without further purification. The reagents used were iron (II) chloride tetrahydrate (Alfa Aesar, 98%), triethylamine (Alfa Aesar, 99%), hexadecyltrimethylammonium bromide (CTAB, Fisher, 98%), N,N-dimethylformamide (DMF, Sigma-Aldrich, ACS reagent), ammonium hydroxide (NH4OH, Sigma-Aldrich, ACS reagent, 28.0−30.0%), tetraethyl orthosilicate (TEOS, Fisher, 98%), (3-chloropropyl)- triethoxysilane (CPTES, Sigma-Aldrich, 98%), hydrochloric acid (Fisher, ACS grade), N-(trimethoxysilylpropyl)-ethylenediaminetriacetate, trisodium salt, sodium thiosulfate (Ricca Chemical Company), potassium bromide (KBr, Fisher, ACS reagent), iodine (Macron Fine Chemicals), acetic acid (Acros, 99.8% for analysis), acetone (Fisher, ACS reagent), ethyl alcohol (Fisher, ACS reagent), methanol (Fisher, ACS reagent), and chloroform (Fisher, ACS reagent).

3.2. Synthesis of Amine-Functionalized nanoparticles

$FeCl_2 \cdot 4H_2O$ (2.99 g) was dissolved in 30 mL of deionized water (DI water) by stirring magnetically. Triethylamine (3 mL) was added to the solution once the Fe salt dissolved fully. The solution turned greenish immediately, then blue-green, and finally black. The stirring was continued for another 6 hours (h) at RT. The nanoparticles were washed with DI water, acetone, chloroform, methanol, and ethanol multiple times until the supernatant became clear. Finally, the particles were dried in a box furnace at 60 °C. The synthesis was also performed at 0 °C (using an ice bath), and 50 °C to vary the size

of the particles.

3.2.1 CPTES functionalization

Ethanol (35 mL) and NH_4OH (4 mL) were added to the nanoparticle solution. The resultant mixture was sonicated for 5 minutes (min) and then transferred to a stir plate. Four grams of CPTES was added drop-wise, and the solution was stirred for 3 h. The functionalized nanoparticles were washed three times each with DI water and ethanol and once with DMF. The nanoparticles were then suspended in 120 mL of DMF.

3.2.2 SiO_2 coating

Ethanol (160 mL) and NH_4OH (5 mL) were added to the above-mentioned nanoparticle solution. The resultant mixture was sonicated for 5 min and then transferred to a stir plate. Under stirring conditions, TEOS was added drop-wise in aliquots of 5 + 2 + 2 g with additions every 2 h. After the final addition, the solution was covered and stirred overnight (≈ 16 h). The particles were washed three times with DI water. The volume of the modified particles was then adjusted to 35 mL in DI water for CPTES functionalization. The presence of silica coating on the nanoparticles was verified with XRD and TEM measurements.

3.3 Synthesis of DMH–CH_2–N $(CH_3)_2$

5,5-dimethyl hydantoin (6.6 g), dimethyalamine hydrochloride (4.1 g), formaldehyde (37%) (4 mL) and methanol (20 mL) were added into a round bottom flask. Then 2 g sodium hydroxide was added to the mixture and stirred at room temperature for 2 h. After that the organic solvent was evaporated under vacuum

conditions. The residual product was diluted with DI water and extracted with dichloromethane (DCM). The solvent was evaporated and dried under vacuum to produce the product.

3.4 Biocide coating.

The nanoparticle solution was poured into a round-bottom flask, and 5 g each of KBr and DMH−CH_2−$N(CH_3)_2$ (DMH−QACs) was added to it. The mixture was then stirred overnight at 80 °C. The biocide-coated nanoparticles were washed three times each with DI water and ethanol and re-suspended in DI water for storage.

3.5 Chlorination and titration

More than 30 mL commercial bleach solution was added to a 100 mL beaker with a stir bar. The pH value of bleach solution was adjusted to pH 8 by adding a few drops concentrated HCl with a Pasteur pipet. Then 23.5 mL of the pH-adjusted bleach solution was added into a 100 mL volumetric flask, and DI water was added up to 100 mL. Twenty (20 mL) of DI water and the MNPs were transferred into a 100 mL beaker, and the mixture was stirred until a uniform solution was achieved. Twenty (20) mL of the pH-adjusted bleach solution (6000 ppm) was added to the suspension, covered with parafilm, and stirred for 1 h at room temperature. The particles were washed three times with DI water.

To quantitatively assess the loaded active chlorine [Cl^+] on MNPs, titration was performed. The MNPs were added into a solution consisting of 10 mL sodium thiosulfate (0.001 N) and 30 mL DI water. The mixture was stirred for 1 h at room temperature. Then

2 mL of 5% acetic acid was added, and the remaining sodium thiosulfate was titrated using 0.001 N iodine solution.

3.6 Synthesis of 8 nm diameter Fe-oxide particles

$FeCl_3$-$6H_2O$ (8.67 g) and $FeCl_2$-$4H_2O$ (3.14 g) were dissolved into 25 mL of 0.4 M HCl. The Fe solution was added drop-wise into 250 mL of 1.5 M NaOH over 30 min. The nanoparticles were isolated using a strong magnet and washed three times with DI H_2O and once with 0.01 M HCl. The nanoparticle solution was brought to a total volume of 50 mL using DI H_2O.

3.7 Synthesis of 11 nm diameter Fe-oxide particles

$FeCl_3$-$6H_2O$ (8.11 g) and $FeCl_2$-$4H_2O$ (2.98 g) were dissolved into 150 mL of DI H_2O and the solution was heated to 74 °C. 150 ml of 1.5 M NaOH was added rapidly to the Fe solution and stirred under heated conditions for 1 h. The nanoparticles were isolated using a strong magnet and washed thrice with DI H_2O and once with 0.01 M HCl. The nanoparticle solution was adjusted to a total volume of 50 mL using DI H_2O.

3.8 Synthesis of 70 nm diameter Fe-oxide particles

$FeCl_2$-$4H_2O$ (8.95 g) was added to 180 mL of 50 °C DI H_2O and stirred until just dissolved. Eighteen (18) mL TEA was added rapidly and the solution was stirred under heated conditions for 6 h. The nanoparticles were isolated using a strong magnet and washed with DI H_2O until the supernatant became clear. The nanoparticle solution was brought to a total volume of 50 mL using DI H_2O.

3.9 SiO_2 coating of 8 and 11 nm Fe-oxide particles

Ethanol (160 mL) and ammonium hydroxide (4 mL) were added to the particle solution and stirred for 5 min. TEOS (5 g) was added drop-wise, and the mixture was stirred at room temperature for 16 h.

3.10 SiO_2 coating of 70 nm Fe-oxide particles

Ethanol (160 mL) and ammonium hydroxide (4 mL) were added to the particle solution and stirred for 5 min. 5 g + 2 g + 2 g of TEOS were added drop-wise with 2 h of stirring between each addition. Mixture was then stirred for 16 h.

3.11 Antibacterial test.

3.11.1. Preparation of TSA

Fourty (40 g) Tryotone Soya Agar (TSA) (OXOID CM0131) was dissolved in 1 L DI water. The mixture was heated to around 170 °C on a hot plate with a stirring bar until fully dissolved. The solution was autoclaved at 121 °C for about 20 min. The solution was carefully poured into the sterile petri dishes; each TSA plate required about 15 mL TSA solution. The dishes cooled to room temperature without a lid. After covering, plates were stacked upside down and stored in the fridge at 4 °C.

3.11.2. Preparation of TSB

Thirty (30) g Tryptone Soya Broth (TSB) (OXOID CM0129) was dissolved in 1 L DI water into the desired final container (labeled glass jar). The solution was autoclaved at 121 °C for about 20 min. The glass jar was then removed from the autoclave and carefully placed in the fume hood, allowing the container to cool to room temperature. A

sterile lid was screwed on and placed in the fridge at 4 °C.

3.11.3. Cell culture preparation

A bead was taken from the vial and rubbed on the agar using a sterile cotton tip as an applicator. Bacteria were spread all over the agar plate, and the plate was put in the incubator at 37 °C for 24 h.

3.11.4. Broth inoculation procedure

Three test tubes were first prepared and labeled. PBS (1.8 mL) was added to Test tube 1 (T1), while 900 µL of PBS was added to both test tubes 2 (T2) and 3 (T3). Using a cotton swab, isolated colony was isolated from an MRSA (ATCC 33592) cell culture and mixed into T1 and vortexed for a few seconds. Visually compare the turbidity to a reference solution using a Wickerham card to ensure a McFarland standard of 0.5 (10^8 cfu/mL) had been achieved. 100 µL of the bacterial solution from T1 was transferred to T2. Then T2 was vortexed and 100 µL of its contents was added into T3. After the last dilution, 15 µL of the T3 solution was added into a falcon tube filled with 45 mL of TSB solution, and then vortex for few seconds and incubated for 18 h.

3.11.5. Treatments applied to bacterial solution

After culturing at 37 °C for 18 h, the bacterial solution was removed from incubator and 1 mL bacterial solution was transferred into 2 mL Eppendorf tubes to centrifuge the suspensions for 4 min at 5000 xg, then the supernatant was removed and the cells were re-suspended in 1 mL PBS (pH 7.4). The necessary amounts of MNPs solution were added to the bacterial suspensions and the mixtures vortexed for 10 seconds (s), then the

MNPs contacted the bacterial suspension for predetermined times under no magnetic field, alternating and rotating magnetic fields. The same procedures were applied to the blanks, as the controls used DI water instead of MNPs samples.

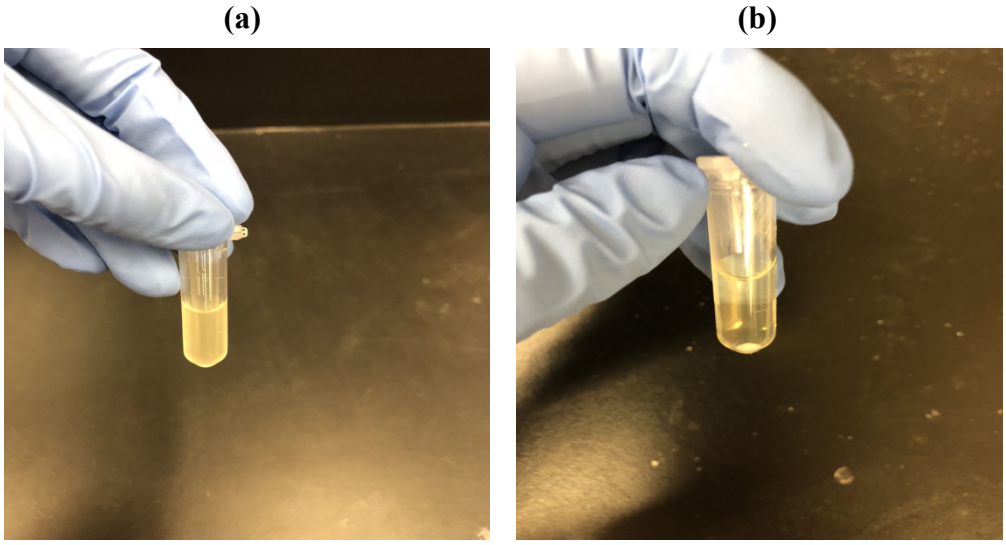

Figure 5. The bacterial solution (a) before being centrifuged and (b) after centrifuged 4 min at 5000 xg, the white pellet is the bacteria.

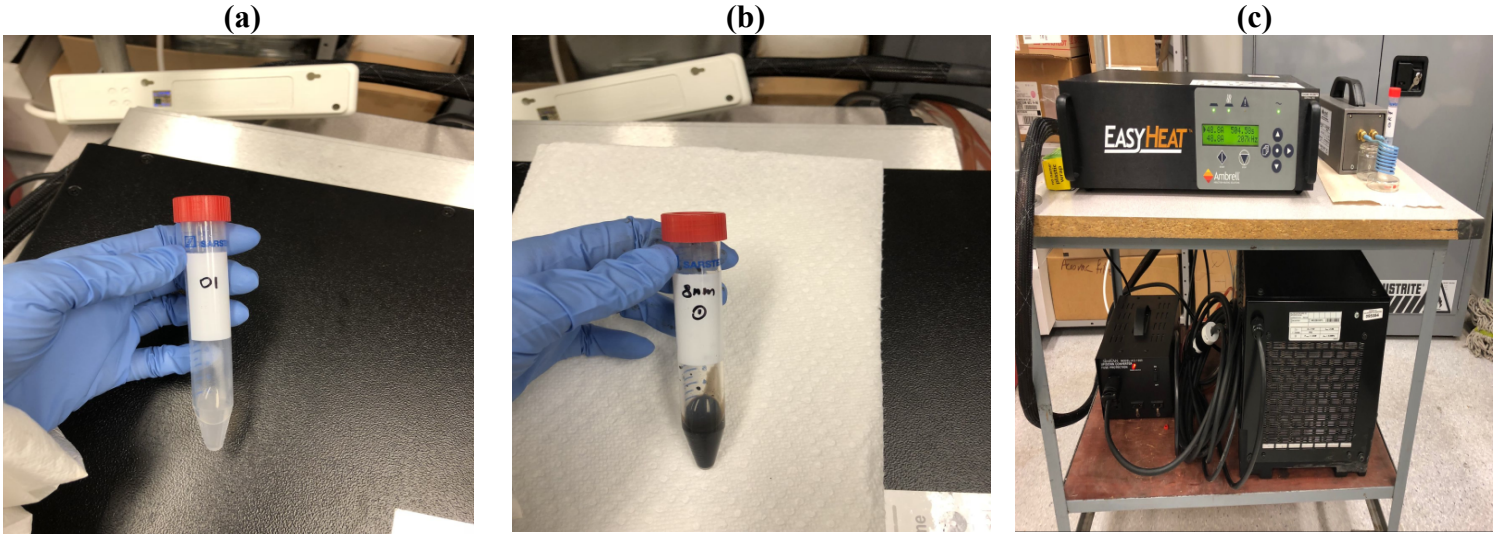

Figure 6. (a) The bacteria were re-suspended in 1 mL PBS after centrifuging; (b) bacteria suspension treated with 1 mL 30 mg/mL MNPs under no magnetic field; and (c) samples was treated in AC magnetic field.

3.11.6. Quantifying the bacteria—series dilution

The treated suspension was then serially diluted in PBS. Each time, 30 μL quenched suspension was transferred into 270 μL PBS to make a 10-fold dilution, and 50 μL of each dilution was placed on the agar plates. The bacterial colonies on the agar plates were put in the incubator at 37 °C overnight. Percentage reduction of bacteria (%) = (A-B)/A × 100; log(reduction) = log(A/B) where A is the bacterial concentration of controls (cfu/mL), and B is the bacterial concentration under the effect of MNPs.

3.12 Anti-biofilm Test

3.12.1. Preparation of 1% TSB

Thirty (30) g Tryptone Soya Broth (OXOID CM0129) and 5 g glucose were dissolved in 1 L DI water into the desired final container (labeled glass jar). The solution was autoclaved at 121 °C for 20 min, and the glass jar was removed from the autoclave and carefully placed in the fume hood, allowing the container to cool to room temperature. A sterile lid was screwed on and the glass jar was placed in the fridge at 4 °C.

3.12.2. Biofilm preparation procedure

Fourteen (14) mL of 1% TSB solution was poured into a large test tube, and then 14μL of incubated bacterial solution was transferred into the large test tube, and the test tube was vortexed for 10 s. Two (2) mL of the solution was added to the 35 mm diameter petri dish.

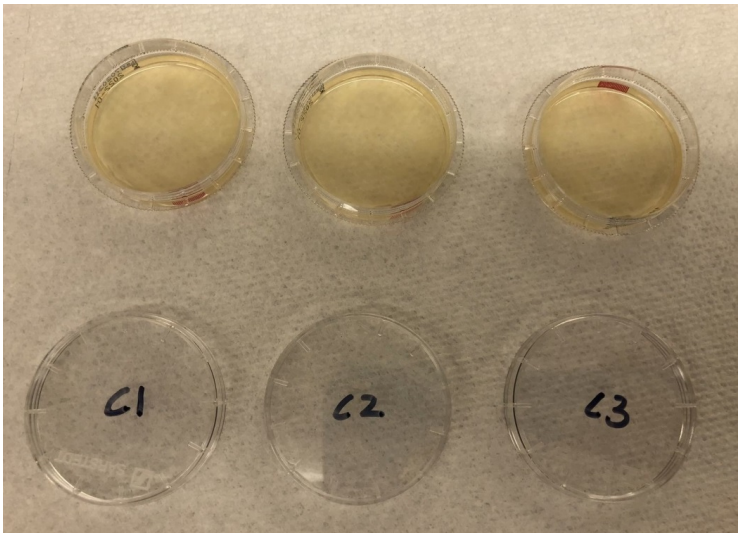

Figure 7. The biofilm after 24 h incubation. The yellow solution is the mixture of bacterial solution and 1% TSB solution, which needs to be poured off before treatment.

3.12.3. Treatments applied to biofilm

All the bacterial solution in petri dish was poured out and the biofilm was washed three times with 200 μL DI water to remove residual planktonic cells. A necessary amount of MNPs was placed on the biofilms to allow the compounds to interact for a predetermined time interval (see Figure 8). Three treatment conditions were tested: no magnetic field, the plates of biofilm treated with MNPs were just left in the fume hood; a low frequency rotating magnetic field; and a high frequency alternating current (AC) magnetic field.

The rotating magnetic field consisted of neodymium permanent magnets rotating at 0.021 Hz under a platform containing the MRSA biofilms. The direction of rotating magnetic field was changed every five minutes. The AC magnetic field setup consisted of a 2.4 kW Ambrell Easyheat operating with a 191 kHz 15.8 kA/m magnetic field. The

biofilms were placed inside the work-head coil such that the applied field was perpendicular to the surface of the film (see Figure 9) to maximize the effect of interparticle interactions.

When the determined time was reached, the treatment solution was poured out and the biofilms were washed six times with 200 µL DI water. If the biofilm treatment contained biocide, after contact for the predetermined time, 1 mL neutralizer was added to the treatment solution and petri dishes with quench were allowed to sit undisturbed for about 10 min before moving to the next step. For the controls, the same procedure was followed using DI water instead of MNPs solution.

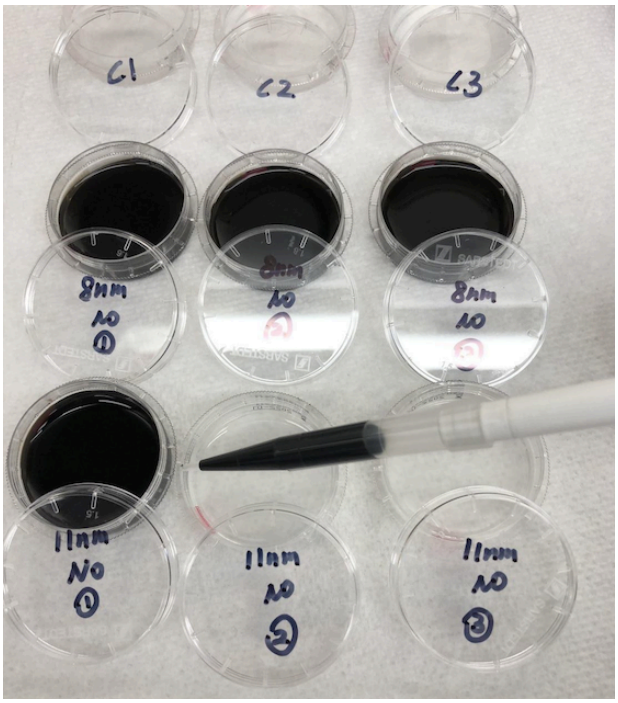

Figure 8. The biofilms were treated with 2 mL 30 mg/mL of different sizes iron-oxide nanoparticles solutions. For the control biofilms, 2 mL of DI water was used for treatment instead of nanoparticles solutions.

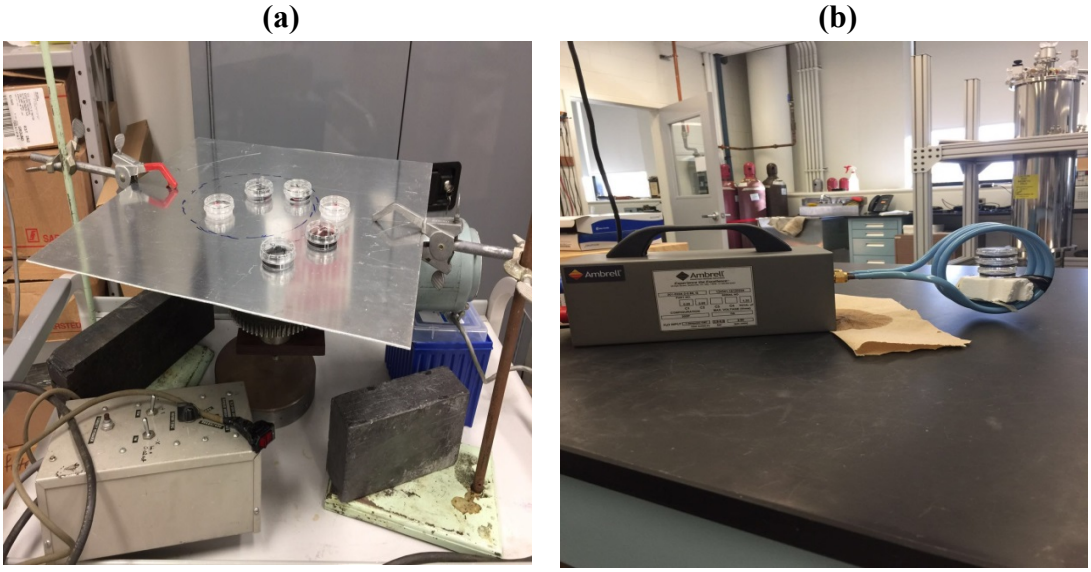

Figure 9. The biofilms were treated with the nanoparticles under (a) high frequency alternating magnetic field and (b) low frequency rotating magnetic field.

3.12.4. Remove biofilm from cell dish

Treatment solutions were removed out by turning the plate over and shaking excess liquid into a waste container. The petri dish was carefully angled over the tray and 200 µL autoclaved DI water was used to wash six times around the edge of the dish. Dishes were allowed to dry at room temperature for 5 min (Figure 10a). A cell scraper was used to remove as much biofilm as possible from each petri dish and the removed biofilm was placed in a test tube containing 2 mL of PBS, then a further 1mL PBS was added to the dish. Any remaining biofilm was scraped and added to the test tube.

(a) **(b)**

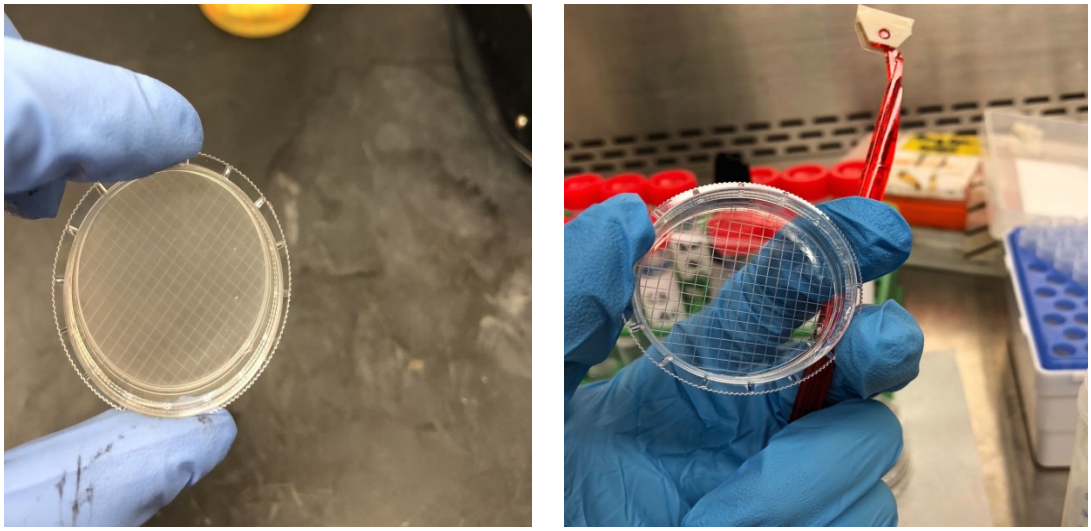

Figure 10. (a) The biofilm after drying around 5 min before scraping off; and (b) the biofilm was scraped off, after scraping the petri dish looked pretty clear.

3.12.5. Quantifying the biofilm

The solution in the test tubes was then serially diluted in PBS. Each time, 30 µL biofilm solution was transferred into 270 µL PBS to make a 10-fold dilution, and 50 µL of each dilution was placed on the agar plates for each zone (Figure 11). The bacterial colonies on the agar plates were put in the incubator at 37 °C overnight.

(a)

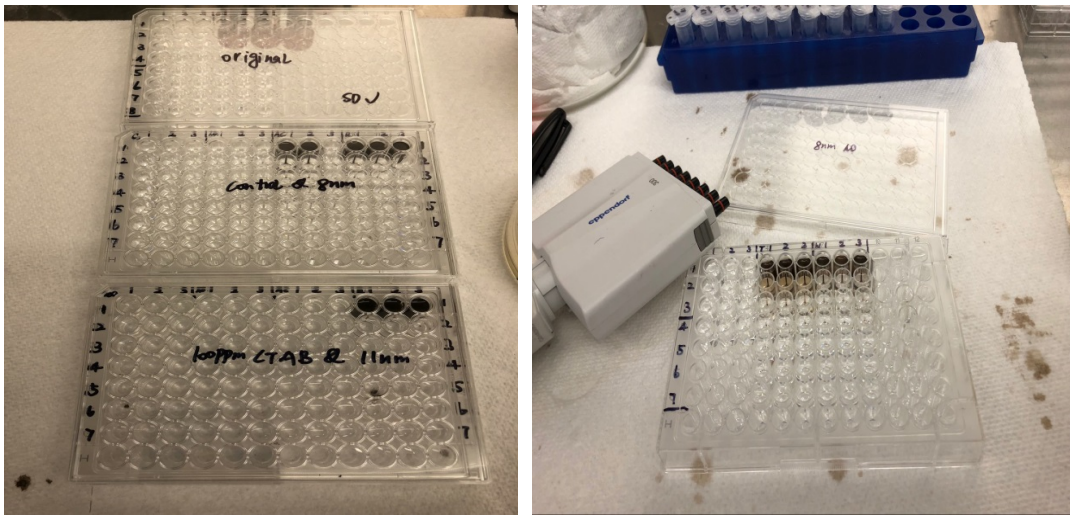

(b)

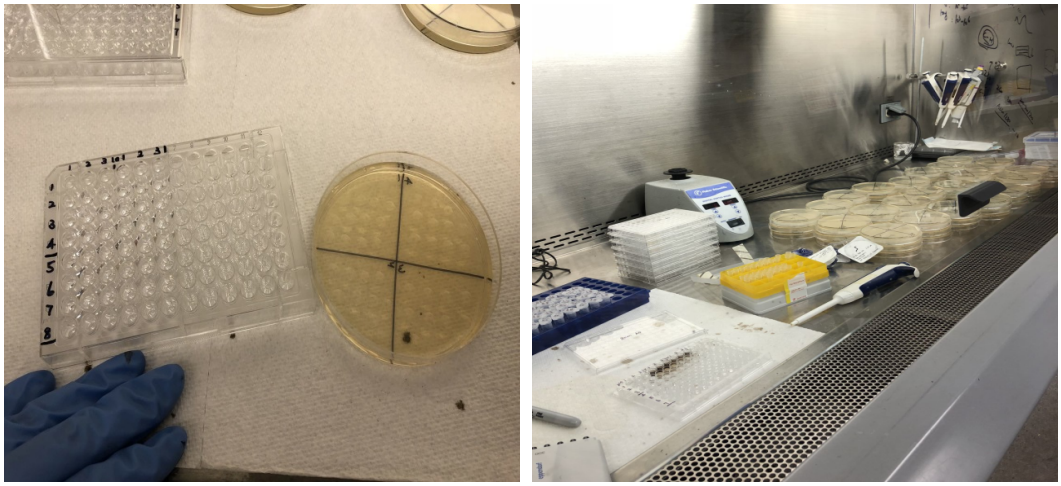

Figure 11. (a) The biofilm solution was serially diluted in PBS by using the 96-well, and (b) 50 µL of each dilution was placed on the agar plates for each zone.

3.12.6. Crystal violet stain test

After incubation, the bacterial solution was dumped out by turning the plate over and shaking out the liquid. Two hundred (200) µL DI water was used to wash biofilms three times. This step helps remove any unattached cells and media components that can be stained in the next step, and significantly lower background staining. After that, 100µL

of 99% methanol was used for fixation of the biofilms. The supernatant fluid was removed and 250 μL of 0.1% crystal violet solution was added to the petri dish and allowed to dry for 30 min at room temperature. The plate was rinsed 3-4 times with 0.9% NaCl solution to remove non-adherent crystal violet stain. Steps were repeated as necessary and then the petri dish was placed upside down on a stack of paper to air dry at room temperature. Several photos of the stained biofilm were taken for comparison.

3.12.7. Confocal laser scanning microscopy

Biofilm was cultured on 35 mm petri dish with glass for 24 h at 37 °C in an incubator. The bacterial solution was poured out, then the biofilms were washed three times with 200 μL DI water and the biofilm was treated with a determined amount MNPs for 15 min under ambient, alternating and rotating magnetic field. When the determined time was reached, the MNPs solution was poured out and the biofilm was washed six times again with 200 μL DI to remove the residual MNPs. Equal volumes of Component A and B (LIVE/DEAD BacLight Bacterial Viability Kit, for Microscopy) were combined in a microfuge tube and mixed thoroughly in an Eppendorf tube. One (1) mL PBS was added to the biofilm together with 3 μL of the dye mixture. The solution was mixed thoroughly and incubated at room temperature in the dark (by covering the dishes with tin foil) for 15 min. At the dark incubation step, live bacteria were stained with Syto 9 to produce a green fluorescence. The bacteria with compromised membranes were stained with propidium iodide to produce a red fluorescence. Both green and red fluorescence

were provided with an argon laser (488 nm laser excitation).

3.12.8. UV/Vis Test

All the treatment solutions were collected and separated into 2 mL centrifuge tubes (each test tube contains ~1 mL solution, see the Figure 12). These tubes were then centrifuged for 5 min at 5000 xg. A 0.45 μm filter was used to filter all the supernatant for each sample and re-collected in a 15 mL test tube. After that, approximately 600 μL of each filtered solution was transferred into a quartz cuvette to do the UV/Vis measurement. The UV wavelength was scanned from 200 to 700 nm.

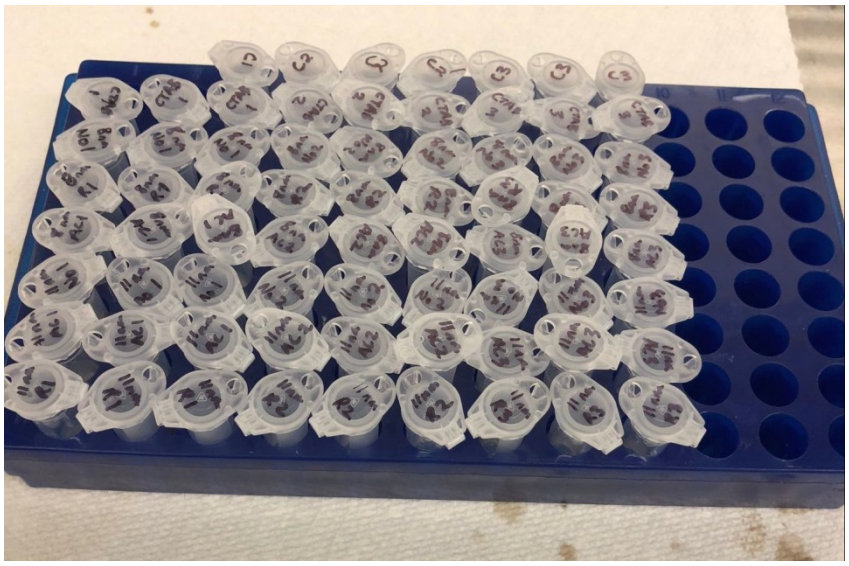

Figure 12. The treatment solutions were separated into 2 mL tubes to prepare for centrifuging.

3.12.9. Zeta-potential

Zeta-potential of the MNPs was characterized using ZetaPALS (Brookhaven Instrument, Holtsville, NY, USA). 0.1 mg/mL of NPs suspension was prepared in distilled water using a probe sonicator (Sonifier 150, Branson, MO, U.S.A.) for 30 s at 40

kHz and 5 root mean square (RMS). The Smoluchowski model was automatically applied for calculation of the surface charge.

3.13. Statistical Analysis

All data are expressed as mean standard deviation (SD) of the triplicate experimental data. A two-tailed Student's t-test was used to determine the differences in biofilm formation between control and each group. The P value of < 0.05 was taken as significant.

3.14. Instruments

For every measurement made to test the coated MNPs, a fresh sample was prepared from the same original lot used for study, after vortex mixing to ensure homogeneity and avoid issues such as change in concentration due to chaining or interaction with container and contamination. Transmission electron microscopy (TEM) images were collected using an FEI Talos F200X S/TEM operating at 80 keV. Nanoparticle samples were diluted with ethanol and a droplet was placed and dried on carbon-coated TEM grids. Powder X-ray diffraction (XRD) measurements were carried out on a Bruker D8 Discover with DaVinci in Bragg–Brentano geometry using Cu Ka radiation with a rotating stage and a zero-background sample holder. Hyperthermia measurements were acquired using a 2.4 kW Ambrell Easyheat equipped with FLIR AX8 infrared camera. Biofilm viability was visualized using a confocal laser scanning microscope (CLSM 700, 63x1.4 N.A. Plan Apo oil objective; Nikon, Tokyo, Japan). Z-stacks were acquired at 0.5

μm intervals across the full biofilm thickness. The area occupied by live (green) and dead (red) bacteria was quantified image by image across the biofilm volume from binary images using ImageJ.

4. Results and Discussion

4.1. Iron oxide Nanoparticles to Treat Bacteria

4.1.1. The morphologies and size distribution of MNPs synthesized at 0 °C, RT and 50 °C.

The size and morphology of the nanoparticles are evident from the TEM images (Figure. 13 a-c). The nanoparticles synthesized at 0 °C appeared to be round discs having a mean diameter and thickness of 40 ± 6 nm and 5 ± 1 nm, respectively, using the Fiji program [143]. From the images, it can be seen that the RT particles included a mixture of hexagonal, cubic, and spherical shapes. When the synthesis temperature was increased to 50 °C, the particles were larger with a size distribution of 94 ± 4 nm, and polyhedron shaped. In all cases, the particle size distributions were log-normal.

X-ray diffraction patterns of 0 °C, RT, and 50 °C iron oxide nanoparticles produced under ambient conditions are shown in Figure 14. In the case of spherical nanoparticles, the crystallite size determined from the XRD pattern is generally very close to the particle size determined from the TEM images. This is because the equation for the determination of crystallite size from the Lorentzian isotropic size parameter assumes the particles to be spherical. In our case, the presence of a noticeable mismatch reconfirms that the particles are non-spherical.

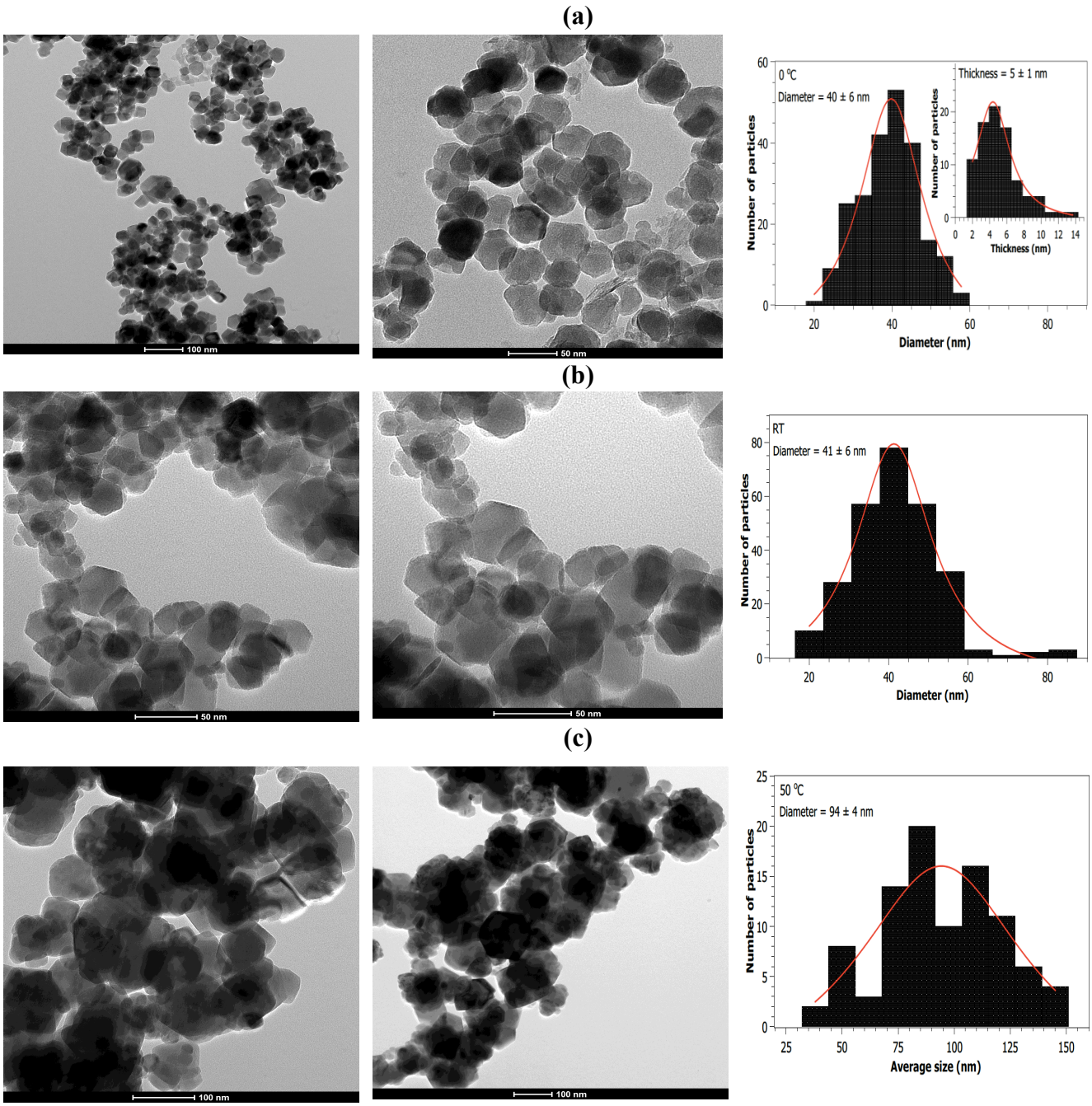

Figure. 13. Representative TEM images and size distributions of the diameter of Fe_3O_4 nanoparticles synthesized at: (a) 0 °C; (b) RT; and (c) 50 °C. In the inset, the typical size distribution of the thickness of the 0 °C nanodiscs is shown. The solid lines are the fitted curves assuming a log-normal distribution.

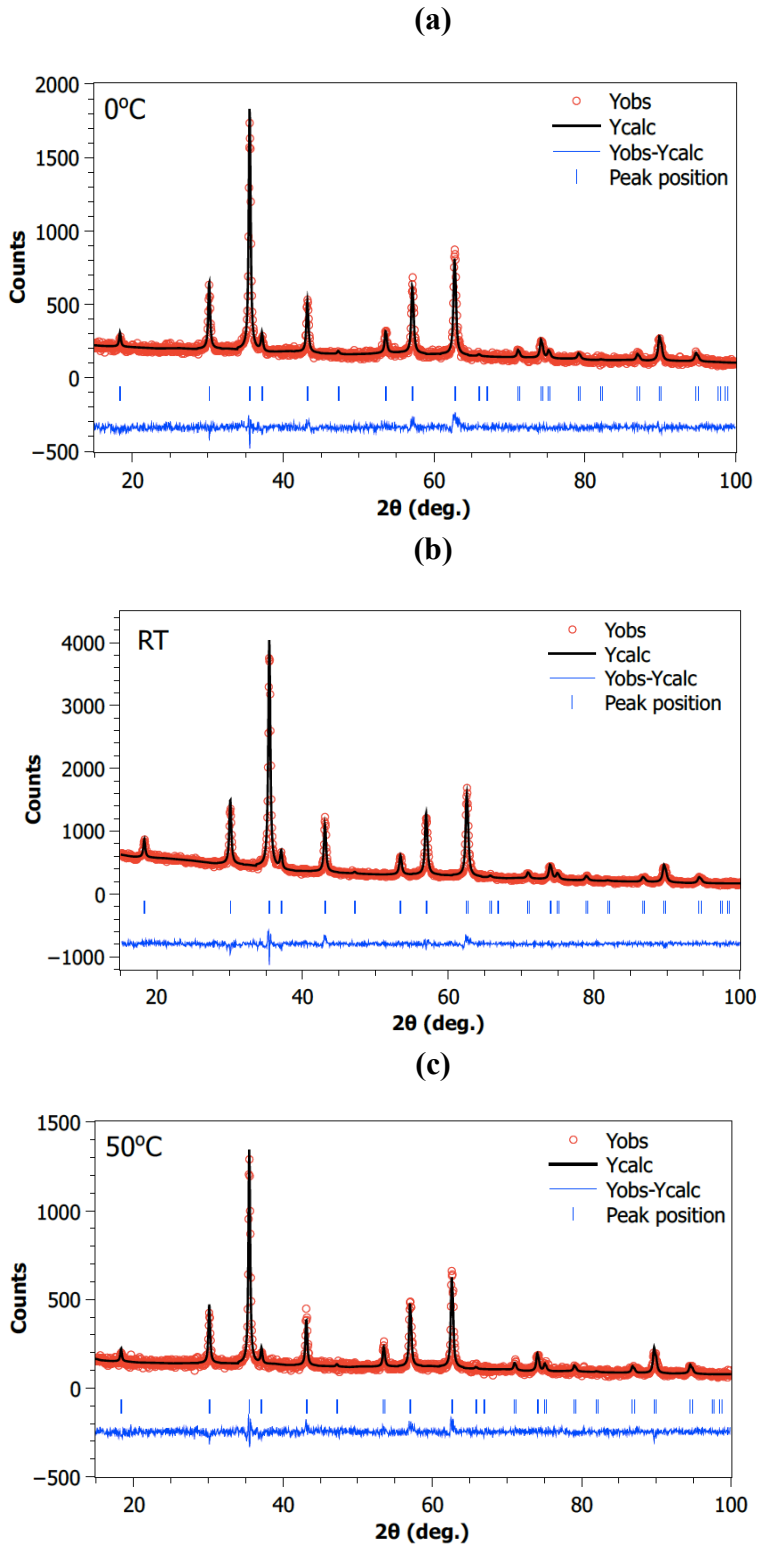

Figure 14. Rietveld-refined room temperature XRD patterns of Fe_3O_4 nanoparticles synthesized at: (a) 0 °C; (b) RT; and (c) 50 °C. The red circles represent the data and solid line is the refinement. Bragg markers identify the reflections of the Fd-3m Fe-oxide phase, and blue lines are the residuals of the refinement.

4.1.2. Anti-bacterial Efficacy of MNPs

Microbial infections and antibiotic resistance of pathogenic bacteria have become a serious public concern. Since the QACs display positive charges and most bacterial cell walls are negatively charged, there should be an electrostatic interaction between them that will promote the antibacterial process [9]. Consequently, the adsorption of QACs onto the cell surfaces is favored over small molecule cations because of their much higher charge density. *N*-chloramine, an effective potent biocide, has a broad antimicrobial spectra, high antibacterial efficacy, and low toxicity [114–117]. *N*-chloramines attack multiple targets in bacterial cells causing irreversible damage to vital sites of the cells from the +1-oxidation state of the chlorine N–Cl bond. For this reason, *N*-chloramines are less likely to induce bacterial resistance [118]. Considering the different merits of these two antibacterial mechanisms, it might be good to combine QACs with *N*-chloramine to take the best parts of both approaches.

MNPs have their special properties, such as easy synthesis, small size, non-toxicity, and good biocompatibility [119]. These nanoparticles could be coated with highly efficient biocides and be easily removed via application of an external magnetic field due to their highly magnetic response. The nanoparticles synthesized under different temperatures (0 °C, RT, and 50 °C) were coated with silica and QACs as well as functionalized with *N*-chloramine to generate antibacterial MNPs. The as-prepared MNPs coating with QACs could attach to the surface of bacteria effectively via electrostatic interaction and kill them by QACs and oxidative chlorine. The activation of antibacterial

functions (conversion of N–H to N–Cl) with sodium hypochlorite is a crucial step prior to an antimicrobial test. Activation permits the loading of oxidative chlorine onto the surface of the MNPs. The activation process was performed by chlorinating MNP@QAC with sodium hypochlorite, which leads to the transfer of active chlorine (Cl^+) from ClO^- to the hydration function groups on the surface of the MNPs through electrophilic substitution. The antimicrobial performance of *N*-chloramine and *N*-chloramine-modified materials is directly proportional to the active chlorine loading and the contact time.

Chlorination of the nanoparticles varied greatly with particle size and shape. The concentrations of *N*-chloramine MNPs were adjusted to get the same concentration [Cl+] (50 ppm) in the bacterial suspension to allow examination of the effects of the MNPs. The bacterial strain mainly responsible for wound-associated infections was chosen as representative for the antibacterial test: Gram-positive bacterium MRSA (ATCC 33592). Table 2 presents the quantitative results of active chlorine loading ([Cl+] in ppm) on different kinds of nanoparticles. As might be expected, the 50 °C sample with the largest particle size (and thus the smallest surface area per unit mass) had the lowest loading of active chlorine; whereas, the smallest particles synthesized at 0 °C had the highest loading.

Table 2. Particle and Active Chlorine Concentrations used for the Antibacterial Test

Sample	MNPs concentration (mg/mL)	[Cl+] (ppm)
0 °C nanoparticles	79	224 ± 32
RT nanoparticles	96	468 ± 58
50 °C nanoparticles	141	103 ± 49

The results of antimicrobial efficacy are summarized in Table 3. The starting bacterial concentration was around 10^6 cfu/mL. All three kinds MNP@QACCl exhibited the same trends, showing a total kill of MRSA (> 6 log reduction) after 2 hours of contact time. These results indicate clearly the positive effect of the QACs and *N*-chloramine incorporated into the MNPs coating structure for antimicrobial efficacy. The 50 °C particles in particular showed bacterial reduction of 99.96% after 1 hour contact which was better than the other two types of particles for the same contact time, so it was chosen for the next anti-biofilm experiments.

The outstanding antimicrobial efficacies of these three kinds of nanoparticles also indicate an improvement of the antimicrobial efficacy with the incorporation of positive charge at the surface. The enhancement of the antibacterial activity of the MNPs is absolute with the introduction of the cationic *N*-chloramine onto the surfaces. Based on the results, a mechanism can be proposed to explain the origin of this boost. Since the bacteria are negatively charged, owing to the presence of the teichoic acid and phosphate on their membrane and cell walls, adding a positive charge on a support facilitates the

adsorption of MNPs onto bacteria for a faster oxidative chlorine transfer to the target sites, leading to a faster bacterial inactivation [120].

Table 3. Antimicrobial efficacy of 0 °C, RT and 50 °C MNPs against MRSA (ATCC 33592) after 2hr contact time

Sample	Particles volume (mL)	Log (reduction)
0 °C MNPs	3.0	6.55
RT MNPs	1.2	6.55
50 °C MNPs	3.5	6.55

* The control bacterial concentration was around 10^6 cfu/mL

It is known that when the particle size of material decreases to the nanometer range, its surface area will increase and its antibacterial activity will also increase [121]. Compared to bulk particles of the same compositions, extra-small sizes have many potential advantages, which include high response to magnetic field and penetration abilities. Therefore, for the next experiments, we moved to test whether the smaller size nanoparticles could have an antibacterial effect even without a biocide coating. Instead of synthesizing iron-oxide magnetic nanoparticles with large sizes (70 nm), we focused on core-shell magnetic iron-oxide nanoparticles of 8 nm and 11 nm in diameter, coated with only silica to prevent aggregation.

Due to their small size and large surface area, these nanoparticles exhibited unique electronic, optical, and magnetic properties, and high magnetic susceptibility. Thus, on application of a magnetic field, the nanoparticles provided a stronger magnetic response [57]. Moreover, once the applied magnetic field was removed, the magnetic particles

retained no residual magnetism at room temperature and hence were unlikely to agglomerate. The small size of MNP was also thought to be responsible for the enhanced permeability and disruption effect.

The antimicrobial efficacy of 30 mg/mL of 8 nm and 11 nm MNPs@SiO_2 against MRSA (ATCC 33592) after 15 min contact time is shown in Table 4. The concentration of the original bacterial solution was $1.6 \pm 0.4 \times 10^9$ cfu/mL and for control was $1.1 \pm 0.4 \times 10^9$ cfu/mL. We used the CTAB (a kind of QAC introduced discussed earlier) as positive control to ensure the experiment proceeded accurately. From the results, we can see that after 15 min of treatment with CTAB, the bacterial concentration decreased to 10^8 cfu/mL, and the bacterial reduction was 85%. However, after treatment with the 8 nm MNPs@SiO_2 under no field condition, alternating and rotating magnetic fields, the bacterial concentrations did not present significant differences from control ($p > 0.05$). Moreover, the 11 nm MNP also exhibited the same trends; treatment with 11 nm MNP@SiO_2 also resulted in no effective killing of the bacteria. Therefore, according to the above results, both the 8 nm and 11 nm MNPs@SiO_2 were ineffective in killing MRSA planktonic bacteria. In other words, they did not cause a significant bacterial reduction after 15 min contact time, regardless of the treatment conditions. Based on these results, we establish the MNPs have no effect on the planktonic bacteria.

Table 4. Antimicrobial efficacy of 8 nm and 11 nm MNPs@SiO_2 against MRSA (ATCC 33592) after 15 min contact time

Sample	Condition	Bacterial Concentration (cfu/ml)
Control		$1.1 \pm 0.4 \times 10^9$
Positive control (100 ppm CTAB)		$2.4 \pm 0.5 \times 10^8$
8 nm MNPs	No field	$1.5 \pm 0.2 \times 10^9$
	AC field	$1.2 \pm 0.3 \times 10^9$
	Rotation	$1.4 \pm 0.3 \times 10^9$
11 nm MNPs	No field	$9.5 \pm 2.2 \times 10^8$
	AC field	$8.4 \pm 2.5 \times 10^8$
	Rotation	$1.7 \pm 0.3 \times 10^9$

4.2. Iron Oxide Nanoparticles to Treat Biofilm

4.2.1. Phase purity and morphology of 8 nm, 11 nm and 70 nm iron-oxide nanoparticles.

Transmission electron microscopy images for the 8 nm, 11 nm and 70 nm Fe-oxide@SiO_2 MNPs are shown in Figure 15. The particle sizes were measured using ImageJ [145], and fitted with a lognormal distribution. The Fe-oxide core sizes of diameter for two kinds small particles are 8 $\pm$ 3 nm and, and 11 $\pm$ 5 nm, respectively. After the magnetic particles were coated with silica, a thin layer of SiO_2 was observed in TEM (Figure 15 c.) The 8 nm and 11 nm MNPs are considered spherical shapes, while the 70 nm MNPs have clear edges and formed polyhedrons such as cubes and hexagons.

Figure 16 presents typical X-ray diffraction patterns of Fe-oxide nanoparticles with SiO_2 coating. Diffraction patterns showed the reflection characteristics of the Fe-oxide spinel structure. All reflections are Scherrer, broadened by significantly different amounts between systems, indicating that the average crystallite sizes of the three Fe-oxide nanoparticle systems differed substantially. A Rietveld refinement of the patterns confirmed the spinel structure (Fd-3m) of the Fe-oxides Fe_3O_4 or γ-Fe_2O_3 as expected from Massart-based synthesis. Refined lattice parameters of a = 8.385 ± 0.001A for the 8 nm diameter MNPs, a = 8.374 ± 0.001A for the 11 nm diameter MNPs and a = 8.4031 ± 0.0003A for the 70 nm MNPs are also consistent with a spinel Fe-oxide (the bulk lattice parameter of Fe_3O_4 is known to be 8.397A and γ-Fe_2O_3 it is 8.336A [140]).

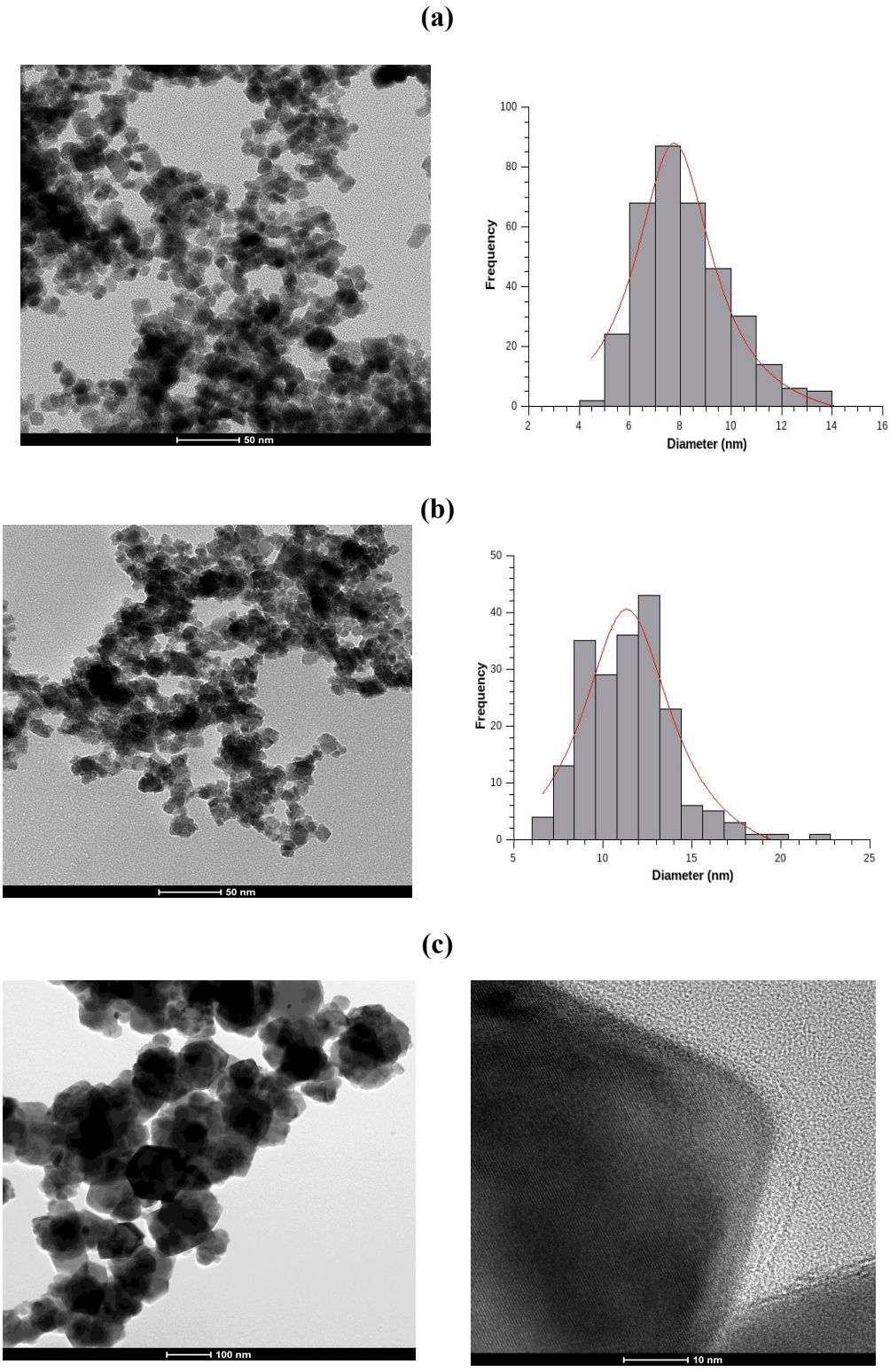

Figure 15. TEM images and the typical particle size distributions for (a) 8 nm MNPs, (b) 11 nm MNPs, and (c) of 70 nm Fe-oxide MNPs and high-resolution of silica coating edge.

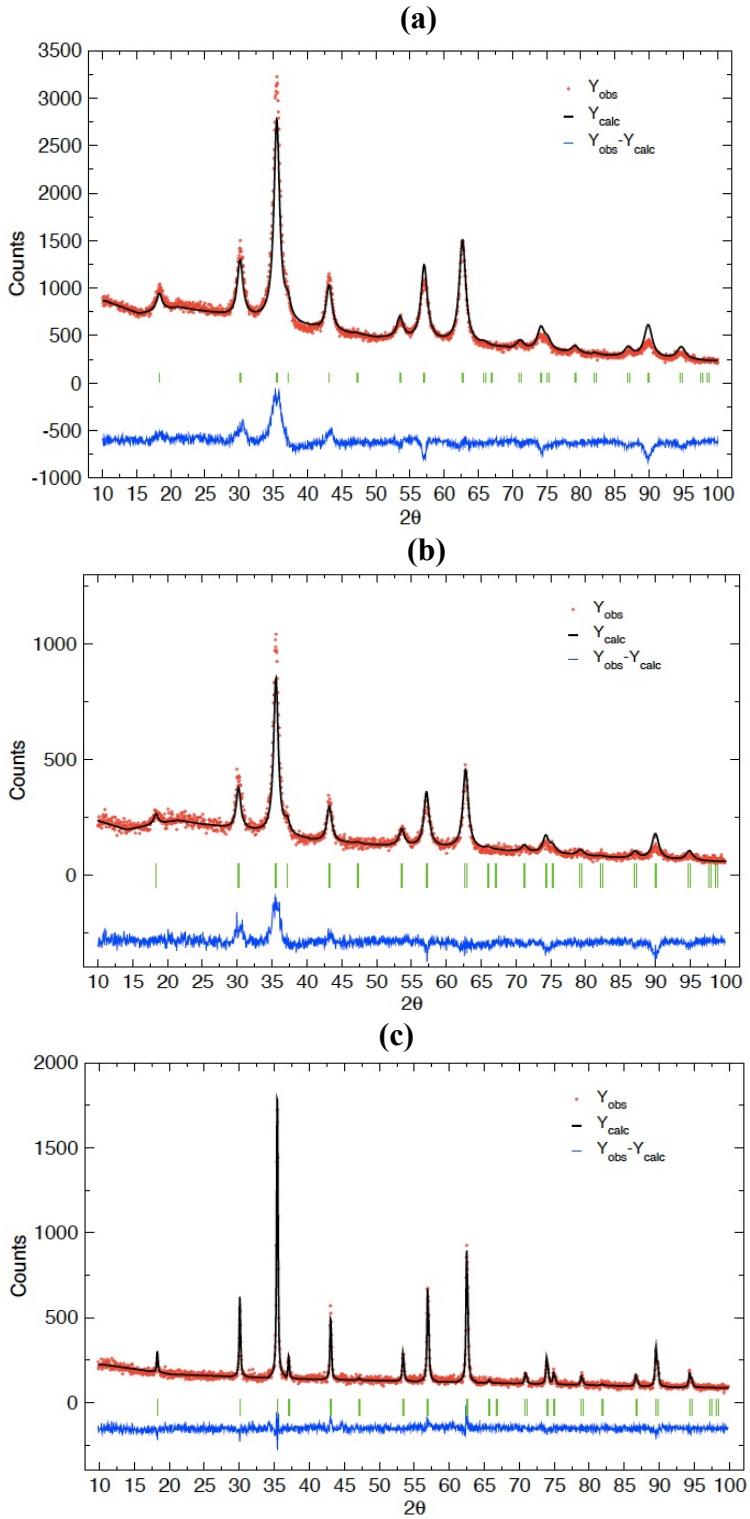

Figure 16. X-ray diffraction patterns of: (a) the 8 nm diameter Fe-oxide MNPs; (b) the 11 nm diameter Fe-oxide MNPs; and (c) the larger, 70 nm Fe-oxide MNPs. Red circles represent the raw data, Bragg markers identify the reflections of Fd-3m Fe-oxide and blue lines are fit residuals.

4.2.2. The Zeta—potential of iron-oxide nanoparticles

Zeta-potential is a critical parameter that is closely related to particle surface charge. It is related to interactions between particles and biomolecules and is thought to be an important factor for formation of aggregates [112]. Nanoparticles with a zeta potential between −10 and +10 mV are considered approximately neutral, while nanoparticles with zeta potentials of greater than +30 mV or less than −30 mV are considered strongly cationic and anionic, respectively [113]. In this study, at neutral pH (pH=7), all the particles presented negative surface charge as shown in Table 5 because the nanoparticles have a thin silica coating shell. The high absolute value ranging from 20.68 to 33.36 mV indicates good colloidal stability and low aggregation in aqueous solutions.

Table 5. The zeta-potential of different sizes iron-oxide magnetic nanoparticles

Sample	Zeta-potential (mV)
8nm MNPs@SiO_2	-33.36 ± 3.15
11nm MNPs@SiO_2	-20.68 ± 2.61
70nm MNPs@SiO_2	-31.37 ± 1.56

4.2.3. Verification of Biofilm Growth Under Static Conditions

The crystal violet stain test results of three standards (*S. aureus* (ATCC 29213 & 25923) and MRSA (ATCC 33592)) and five non-standard strains after incubating for 24 h in 37 °C incubator are shown in Figure 17, while Figure 18 shows the CV staining results for these biofilms grown for 48 h in 37 °C incubator. In order to compare whether

different washing conditions could damage the biofilm, for each strain, four biofilm samples were prepared under three different washing conditions: two were washed three times using 200 μL DI water before contact with the crystal violet solution; one had no washing; and the last sample was gently immersed in DI water three times before staining. The dark violet hue shows a healthy biofilm. Had the film failed to grow, the results of the staining would be a lighter color or none, since there would be no bacteria and EPS for the stain to adhere. The photos show that after the biofilms were grown for 24 h then stained with CV, all of the staining color on the washed biofilms seemed lighter compared to the color on the biofilms that were not washed. This is possibly because without washing, the planktonic bacteria were also stained by the crystal violet solution and caused the darker color. After 48 h growth time, the color of some of the biofilms looked a little darker than those grown for 24 h, but this did not have a big difference on the strain MRSA (ATCC 33592). Therefore, growth time and strain species have an influence on the growth of the biofilms. Thus, considering all the above factors, we have chosen the MRSA (ATCC 33592) strain to culture biofilm and incubate for 24 h to do our next experiments. Figure 19 shows the CV result of MRSA (ATCC 33592) strain cultured biofilm, the uniformly dark violet color indicates a healthy biofilm. The crystal violet staining gave us a rough visualization of biofilms. The next step was to develop a methodology that can be used to consistently, accurately and objectively measure the quality of a biofilm.

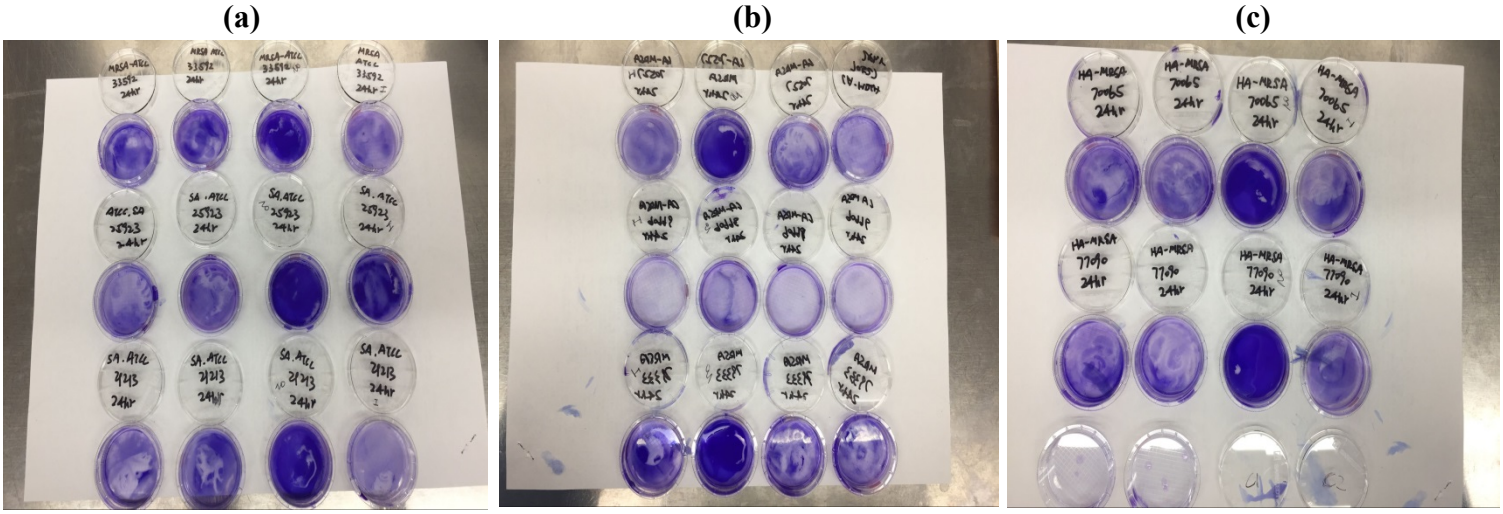

Figure 17. Crystal violet staining results of three standard biofilms after grown for (a) 24 hours with 2 mL 1% glucose TBS. (b) and (c) are the CV results of clinical strains cultured biofilms. The first and second columns from the left show biofilms that were washed three times with 200 µL DI water before contact with 0.1% crystal violet solution; the third columns biofilms show without washing and the biofilms in the last columns were gently immersed in water three times before staining.

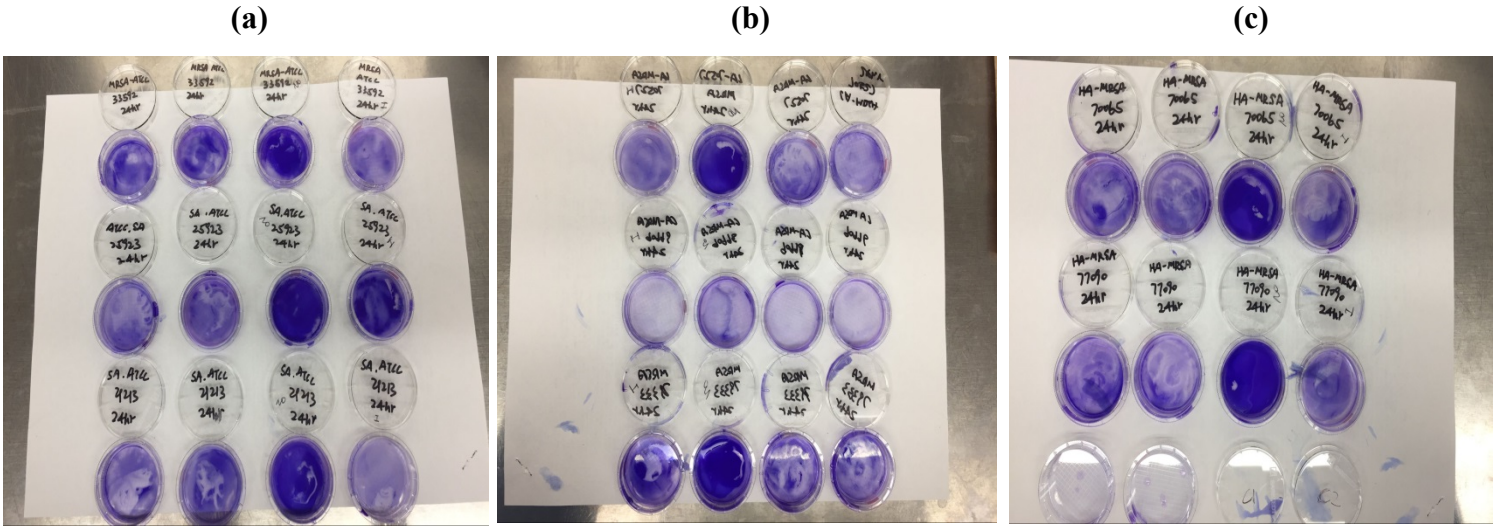

Figure 17. Crystal violet staining results of three standard biofilms after grown for (a) 24 hours with 2 mL 1% glucose TBS. (b) and (c) are the CV results of clinical strains cultured biofilms. The first and second columns from the left show biofilms that were washed three times with 200 µL DI water before contact with 0.1% crystal violet solution; the third columns biofilms show without washing and the biofilms in the last columns were gently immersed in water three times before staining.

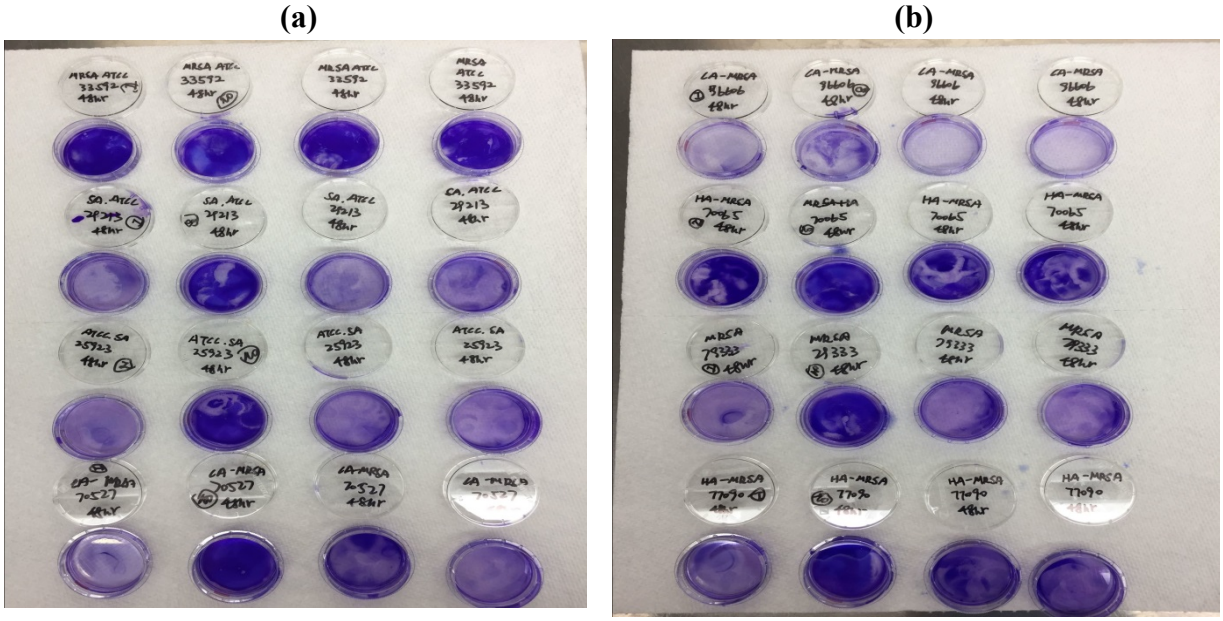

Figure 18. The crystal violet stain results for (a) three standard and one non-standard biofilm after incubating for 48 hours with 2 mL 1% glucose TBS and (b) of four kinds non-standard biofilms CV test results. The first column (on the left) shows staining results of biofilms that were gently immersed in DI water for three times before contact with 0.1% crystal violet solution. The second column shows biofilms without washing and the last two columns biofilms that were washed three times with 200 µL DI water before treatment.

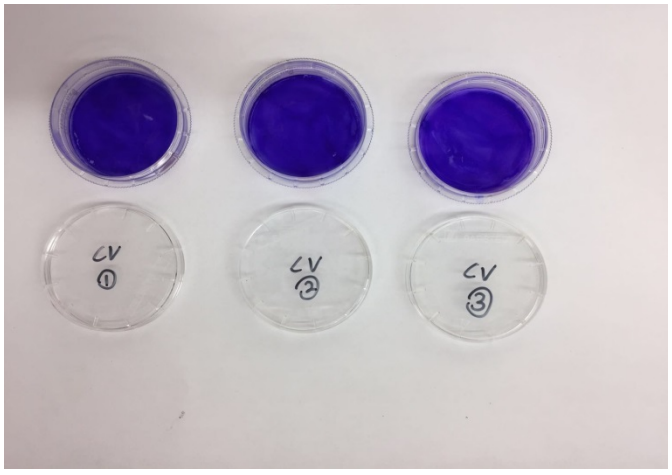

Figure 19. Image of crystal violet staining results for MRSA (ATCC 33592) biofilm after 24 hours growth in 37 °C incubator and three washes.

SEM has proven to be a powerful tool for the study of crystalline biofilms. However, a drawback of SEM is the need to process samples before viewing. This involves fixation and dehydration, followed by coating with conductive materials such as gold or platinum. The processing can potentially alter the structure of the biofilms and introduce artifacts. The environmental scanning electron microscope (ESEM) can avoid these problems and show details of the surface morphologies of microbial biofilms and their structures. From Figure 20, direct ESEM observations clearly reveal the fibrous or amorphous matrices, which represent the EPS, and the uniform growth of bacteria within the biofilms.

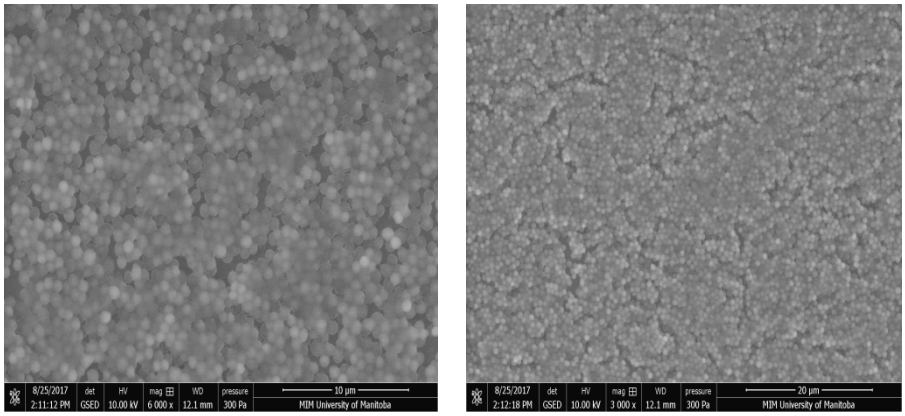

Figure 20. The ESEM images of control biofilm (without being exposed to MNPs). Note: The biofilm strain was MRSA (ATCC 33592), and cultured with 1% glucose TSB and grown for 24 hours. The concentration of the bacteria is around 10^9 cfu/mL.

4.2.4. The Anti-biofilm Efficacy of Iron-oxide Nanoparticles

The anti-biofilm efficacy of 8 nm, 11 nm and 70 nm MNPs@SiO_2 against MRSA (ATCC 33592) biofilm was tested under three different conditions: no field condition, alternating, and rotating magnetic field. Before we used these nanoparticles to treat the biofilms, we needed to ensure the alternating and rotating magnetic field would not damage the control biofilm (the biofilm not being exposed to MNPs). From our quantifying results, the control biofilm concentrations were $7.5 \pm 0.8 \times 10^8$, $7.5 \pm 0.7 \times 10^8$ and $7.4 \pm 0.9 \times 10^8$ cfu/mL for the controls (no magnetic field), alternating, and rotating magnetic field, respectively.

According to the t-test analysis of these three controls, the concentrations under the AC field and rotation had no significant differences compared to the controls ($p > 0.05$). This means the AC and rotating magnetic fields on their own do not cause any damage on the biofilms. The next step in testing the anti-biofilm efficacy of the nanoparticles used the 8 nm, 11 nm, and 70 nm MNPs@SiO_2 to treat the MRSA biofilm

The antimicrobial activities of 8 nm, 11 nm, and 70 nm MNPs@ SiO_2 were tested using AC and rotating magnetic field. The initial concentration of bacterial solution used to culture the biofilms was $1.1 \pm 0.1 \times 10^9$ cfu/mL, and the control biofilm (not being exposed to MNPs) concentration was $7.5 \pm 1.5 \times 10^8$ cfu/mL.

Table 6 presents the antimicrobial efficacy of three different sizes of silica coated MNPs against MRSA biofilm. The results show that both particle sizes and treatment conditions affected the efficacy of the nanoparticles. The MNPs under no field condition

were not as effective as AC field or rotation in causing biofilm reduction. The 11 nm MNPs had the highest efficiency among all the three sizes of nanoparticles. After 15 min contact with 30 mg/mL of 11 nm MNPs under no field condition, the log reduction was 3.54 log; while the MNPs under AC magnetic field exhibited a directional increase, and a log reduction of 3.62 log. The 30 mg/mL of 8 nm and 70 nm MNPs@SiO_2 also showed this trend that achieved a directional increase after 15 min of contact time under AC field compare with no field condition. What's more, compared to no field condition, under rotation condition for the 8 nm and 11 nm nanoparticles showed a significant improvement and all the three sizes of nanoparticles achieved the highest log reduction among all the three conditions; the log reductions under rotation were 4.71, 4.00 and 2.69 log for 11 nm, 8 nm and 70 nm nanoparticles, respectively.

Because of their similar size, the 8 nm and 11 nm nanoparticles have similar effects, However, the 8 nm nanoparticles had slightly less effect than 11 nm nanoparticles, while the 70 nm MNPs were the least effective among all the three sizes of nanoparticles. The comparative results indicate the positive effect of MNPs size in relation to the anti-biofilm efficacy. The better performance of the smaller sized MNPs can be attributed to the dispersion of the particles. From the above results, it is seen that the MNPs under AC field achieved a directional increase; whereas, under rotation obtained a significant improvement over the MNPs under no field condition. These comparative results demonstrate that the anti-biofilm efficacy of MNPs is improved with the incorporation of AC and rotating magnetic field; however, AC field gave not as much improvement as

rotation.

Table 6. Anti-biofilm efficacy of MNPs@SiO_2 against MRSA (ATCC 33592) biofilm for 15min under different conditions

Sample	Particle	Bacterial log reduction under various conditions		
	(mg/mL)	No field	AC Field	Rotation
8nm MNPs	30	3.40 ± 0.01	3.49 ± 0.06	4.00 ± 0.04
11nm MNPs	30	3.54 ± 0.07	3.62 ± 0.06	4.71 ± 0.05
70nm MNPs	30	0.98 ± 0.22	1.12 ± 0.20	2.69 ± 0.13

Following the encouraging anti-biofilm effect of MNPs, we looked to investigate the mechanism causing the biofilm reduction. We hypothesized that there were two main reasons for the impressive efficiency of the MNPs. First, the reduced biofilm was killed by our nanoparticles; second, the nanoparticles led to the dispersal of the biofilm. However, from the previous results of antibacterial efficacy of 8 nm and 11 nm MNPs against MRSA (Chapter 3, Table 4) showed that neither of these sizes negatively impacted the viability of the planktonic bacteria. Taken together, these data strongly suggested that the impressive anti-biofilm effect of the MNPs is because they cause biofilm cell detachment, and possibly cause damage to the biofilm matrix. As for anti-biofilm test we only quantified the bacterial number of left film, the detached bacteria could also be existed in treatment and washing solution. Therefore, to test this hypothesis, in the next experiments we collected all the treatment and washing solutions after treatment with nanoparticles to quantify the live cell numbers on nutrient agar

dishes and compare with the control.

The bacterial numbers of treatment and washing solution quantify results are shown in Table 7. The total bacteria number is a combination of the bacteria number of remaining film, in the treatment solution and the washing solution, while T+W is the sum of bacteria in the treatment and washing solutions. Figure 21 shows the collected treatment and washing solution.

(a) **(b)**

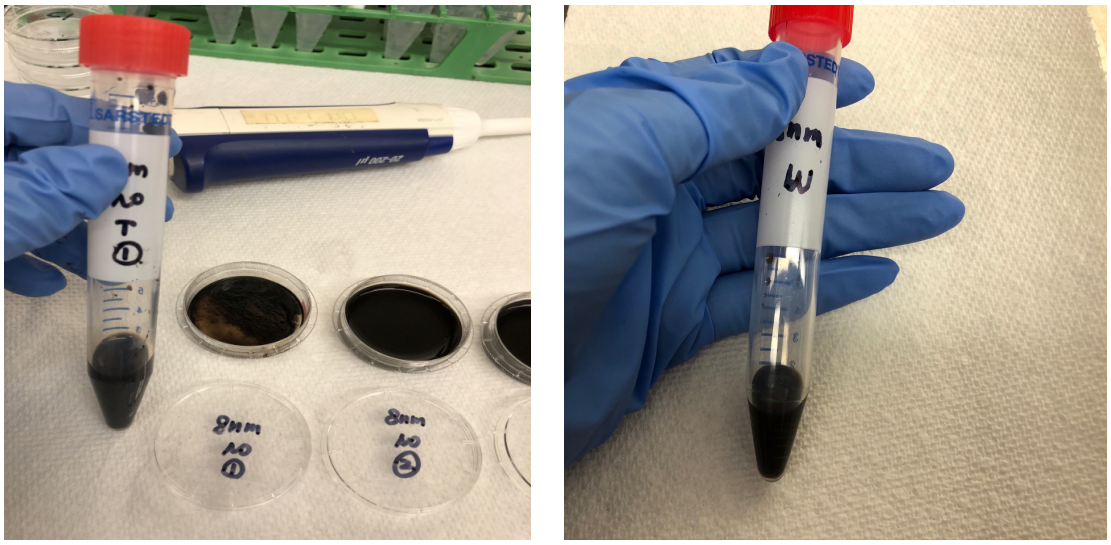

Figure 21. (a) The treatment solutions were collected of the 2 mL nanoparticles solution after contact with biofilm for 15 min with no magnetic field, compared with alternating and rotating magnetic fields. After treatment with the biofilms and collection of the treatment solution, the films were washed six times by using 200 µL DI water to remove the residual nanoparticles. (b) The washing solutions (~1.2 mL) were collected in 15 mL test tubes.

Table 7. Quantified results of treatment and washing solution after treated with 8nm and 11nm MNPs @SiO_2 under different conditions

Samples	Condition	Remaining film (cfu)	Treatment sol'n (cfu)	Washing sol'n (cfu)	Bacterial number (T+W)	Total (cfu)
Control		$2.2 \pm 0.4 \times 10^9$	$1.1 \pm 0.2 \times 10^8$	$2.0 \pm 0.2 \times 10^8$	$3.0 \pm 0.1 \times 10^8$	$2.5 \pm 0.5 \times 10^9$
8nm MNPs	No field	$8.8 \pm 0.3 \times 10^5$	$4.1 \pm 0.3 \times 10^8$	$1.9 \pm 0.1 \times 10^9$	$2.3 \pm 0.07 \times 10^9$	$2.3 \pm 0.07 \times 10^9$
	AC field	$7.3 \pm 0.1 \times 10^5$	$1.7 \pm 0.08 \times 10^9$	$1.3 \pm 0.2 \times 10^9$	$3.0 \pm 0.3 \times 10^9$	$3.0 \pm 0.2 \times 10^9$
	Rotation	$2.2 \pm 0.2 \times 10^5$	$3.1 \pm 0.4 \times 10^9$	$5.9 \pm 1.0 \times 10^9$	$3.1 \pm 0.4 \times 10^9$	$3.1 \pm 0.4 \times 10^9$
11nm MNPs	No field	$6.4 \pm 1.1 \times 10^5$	$1.2 \pm 0.2 \times 10^9$	$1.5 \pm 0.6 \times 10^9$	$2.7 \pm 0.2 \times 10^9$	$2.7 \pm 0.2 \times 10^9$
	AC field	$5.4 \pm 0.7 \times 10^5$	$2.4 \pm 0.3 \times 10^9$	$5.4 \pm 0.7 \times 10^8$	$3.0 \pm 0.2 \times 10^9$	$3.0 \pm 0.2 \times 10^9$
	Rotation	$4.3 \pm 0.5 \times 10^4$	$3.1 \pm 0.2 \times 10^9$	$5.7 \pm 0.7 \times 10^7$	$3.2 \pm 0.2 \times 10^9$	$3.2 \pm 0.2 \times 10^9$

(a)

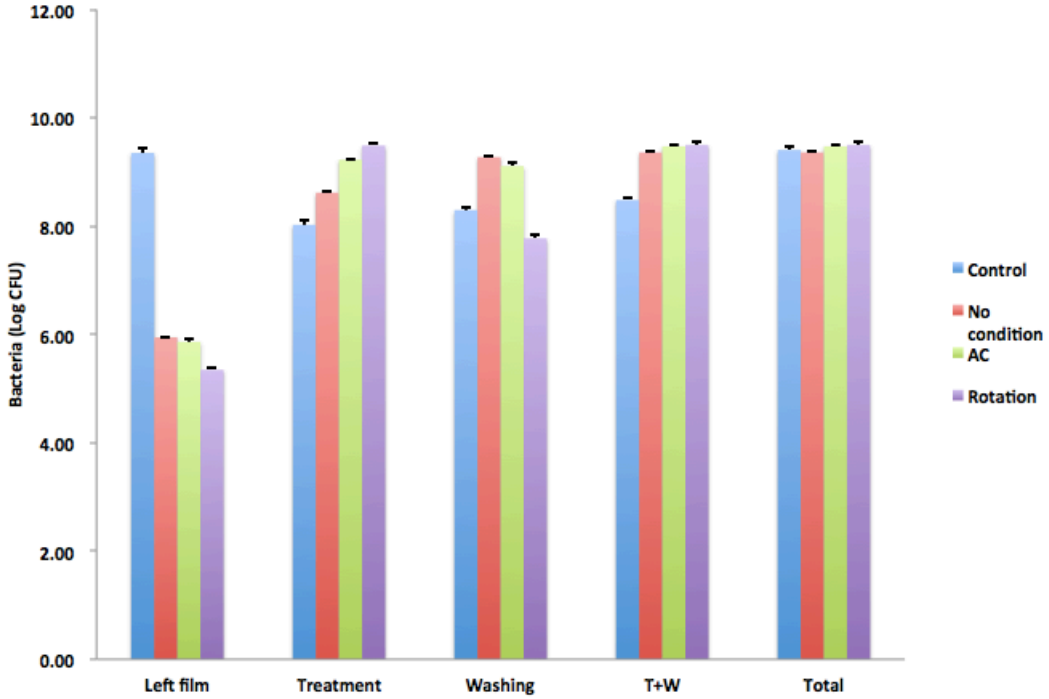

(b)

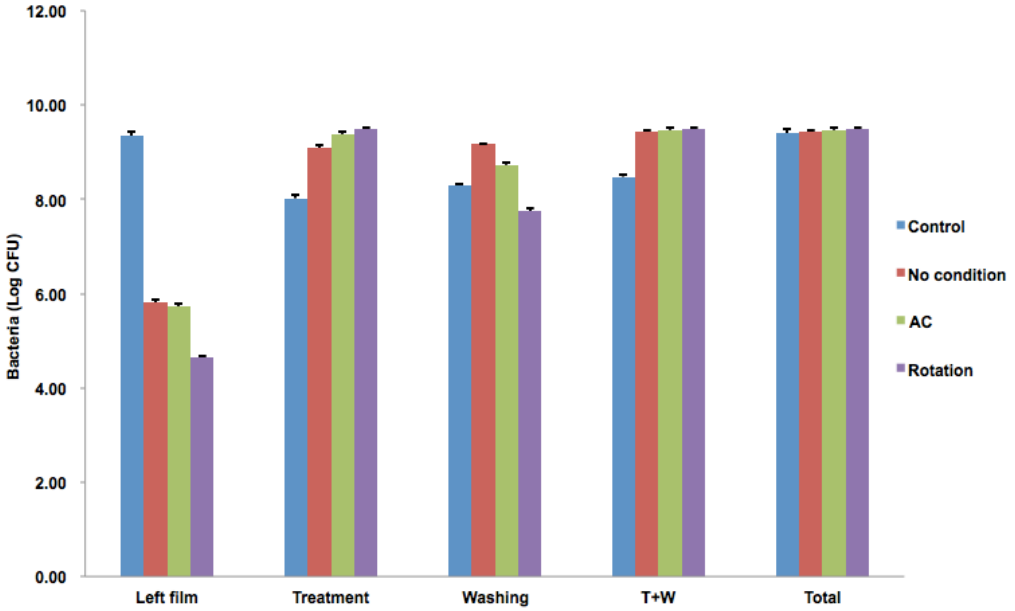

Figure 22. Graphs of quantified results of anti-biofilm test for (a) 8 nm and (b) 11 nm MNPs@SiO_2. The total bacteria number is the sum of bacteria in the remaining biofilm, in the treatment and washing solutions; T+W is the sum of bacteria in the treatment and washing solutions.

From the 8 nm and 11 nm nanoparticles results, we could clearly see that the total bacteria number (a combination of the bacteria number of remaining film, in the treatment solution and the washing solution) after treatment with nanoparticles under no field condition, AC field and rotation have no significant differences in the total bacteria number compared to the control ($p < 0.05$). This trend can also be seen clearly in Figure 22. Therefore, the total bacteria number of biofilm has not decreased after treatment with 30 mg/mL of 8 nm and 11 nm nanoparticles under different conditions, which demonstrates that the biofilm bacteria were not killed by the nanoparticles. These results are also consistent with our antibacterial test results.

When we compared the bacteria number of treatment solution and washing solution

(T+W) after treatment with 30 mg/mL of 8 nm and 11 nm MNPs, we found that no matter under which conditions, the bacteria number of samples (T+W) was always higher than the controls. The significantly increased bacteria number of treatment and washing solution ($p< 0.05$) clearly indicates that the nanoparticles could lead to biofilm dispersal, which means that the increased bacteria number in treatment and washing solutions is caused by the detached cells. Besides that, through Table 7 results we found for the 11 nm MNPs, the bacteria number of treatment solution was a directional increase from no field condition, AC and rotation had the highest bacteria number of their treatment solution; whereas, the opposite trend appeared in the case of washing solution. These results indicated that both the AC and rotation have the ability to lead to more cell detachment and floating into the treatment solution compared with no field condition; however, the rotation treatment had a better effect than AC to cause the biofilm dispersal.

More than this, for the 8 nm MNPs the bacteria number of treatment solution under no field condition was in the order of magnitude of 10^8 cfu, while 10^9 cfu appeared in the case of washing solution. When we compared the bacteria number of the control treatment and washing solution, we found they were in the same order of magnitude: both around 10^8 cfu. This suggests 8 nm MNPs under no field condition rendered biofilm weaker and more vulnerable to even minimal disturbance during gentle washing. However, this trend did not happen for 11 nm MNPs under no field condition, which also supported our previous results: the 11 nm have a better effect than the 8 nm MNPs. The 11 nm MNPs could lead to more biofilm detachment and floating into treatment solution

compared to the 8 nm MNPs under no field condition. Thus, to further evaluate the damage to the biofilm caused by MNPs treatment, we conducted the UV/Vis test.

4.2.5. Qualitative Analysis of Leakage in Components of Biofilm Matrix after MNPs treated

We analyzed the UV/Vis results of our samples at some important wavelengths based on the knowledge from the literature review (Chapter 1). As we know, the concentrations of nucleic acids in solution are routinely determined from their strong absorbance at 260 nm [49], while the absorption at 230 nm reflects contamination of the sample by substances such as carbohydrates, peptides, phenols or aromatic compounds [51]. Also, the absorption of near UV radiation by proteins is usually monitored at 280 nm since most proteins absorb strongly at that wavelength [50].

The UV/Vis absorbance of 11 nm MNPs treatment solution is shown in Table 8. All the treatment solutions were centrifuged for 5 min at 5000 xg after collection. A 0.45μm filter was used to filter all the supernatant for each sample and approximately 600 μL of each filtered solution was transferred into a quartz cuvette to do the UV/Vis measure. As the 11 nm MNPs had the best effect among all the three sizes of particles, we used the 11 nm MNPs here for a representative analysis. As mentioned in the previous paragraph, the MNPs have no effect on killing the biofilm, but they could have damage on the matrix, so all the absorbance should be caused by the components from the matrix.

For the 11 nm MNPs, treatment with rotation had the highest absorbance at 260 nm and 280 nm wavelength, while the no field condition showed the lowest absorbance at

these wavelengths. These results suggested that the leakage of nucleic acids and protein were most under rotation while least under no magnetic field. These UV/Vis absorbance results are also further corroborated by the treatment solution quantification results. For the 11 nm nanoparticles treatment quantification results, the rotation treatment solution had the highest bacterial number ($3.1 \pm 0.2 \times 10^9$ cfu), the no field condition had the lowest bacterial number of treatment solution ($1.2 \pm 0.2 \times 10^9$ cfu) and AC condition bacterial number lay between the two ($2.4 \pm 0.3 \times 10^9$ cfu). The absorbance of both 260 nm and 280 nm wavelengths for the 11 nm treatment solution increased with the increasing bacterial number left in solution. In other words, the more bacteria left in the treatment solution as a result of more cells being detached, accompanied with more matrix damage, resulted in more components such as nucleic acids and protein from matrix being detected.

Table 8. UV/Vis Results of MRSA (ATCC 33592) biofilm treatment solution after treated with 11 nm MNPs@SiO_2

Samples	Condition	Absorbance (230nm)	Absorbance (260nm)	Absorbance (280nm)	$A_{260/280}$	$A_{260/230}$
Control		0.631	0.209	0.208	1.005	0.331
11 nm MNPs	No Field	0.766	0.323	0.256	1.262	0.422
	AC Field	0.968	0.528	0.369	1.431	0.545
	Rotation	0.963	0.542	0.414	1.309	0.563

Moreover, it is common for nucleic acid samples to be contaminated with other molecules. The ratio of absorbance at 260 nm and 280 nm is usually used to assess the purity of DNA and RNA. A ratio of ~1.8 is generally accepted as "pure" for DNA; a ratio

of ~2.0 is generally accepted as “pure” for RNA. If the ratio is appreciably lower in either case, it may indicate the presence of protein, phenol or other contaminants that absorb strongly at or near 280 nm [141]. However, the 260/230 ratio is used as a secondary measure of nucleic acid purity. The 260/230 values for “pure” nucleic acid are often higher than the respective 260/280 values. Expected 260/230 values are commonly in the range of 2.0 ~ 2.2. If the ratio is appreciably lower than expected, it may indicate the presence of contaminants which absorb at 230 nm [141]. From the Table 8 results, the ratio of 260/280 is lower than 1.8 and 2.0 which means that no pure DNA or RNA existed; further, the ratio of 260/230 is much lower than the range of 2.0 ~ 2.2. Therefore, the treatment solutions probably involve protein, or other contaminants that absorb strongly at or near 280 nm and 230 nm resulting in the lower ratio than expected.

4.2.6. The Morphology of Biofilms after Treatment with 8 nm &11 nm MNPs

From the results so far, the nanoparticles seemed have an effect on leading the biofilm dispersal. However, we still need to verify further whether the biofilm dispersal is due to the nanoparticles causing damage to the matrix. The crystal violet test was conducted to observe the morphology of the biofilms after contact with 30 mg/mL of 8 nm and 11 nm nanoparticles under no field condition, AC field and rotation. In order to get comparative results, we also prepared a sample treated with 100 ppm CTAB as the positive control.

Crystal violet is a basic protein dye that stains not only cells, but also the extracellular matrix of polysaccharides [115], which supported that CV has an advantage

in measuring and observing biofilm. The three control sample results are shown in Figure 23a. The violet color of the negative control (without any treatment) biofilm looked quite uniform and dark, which means that the biofilm was healthy and had no damage. For the positive control (treated with 100 ppm CTAB), by visual observation, the film seemed still thick with some bare spaces; overall the stain color was lighter than the negative control. This phenomenon demonstrated that the 100 ppm CTAB has a positive effect against MRSA. The last control was an empty petri dish; because there was no biofilm, there was no color staining.

(a)

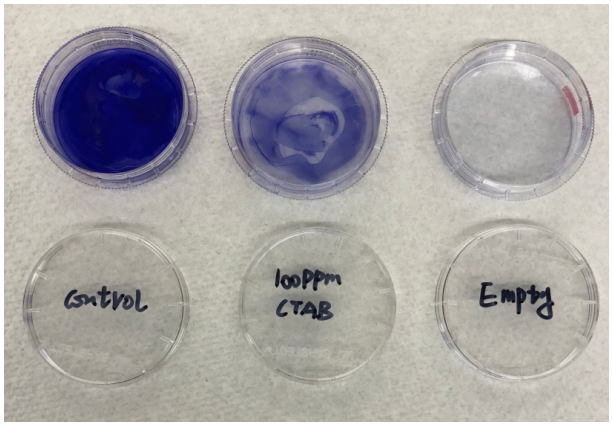

(b)

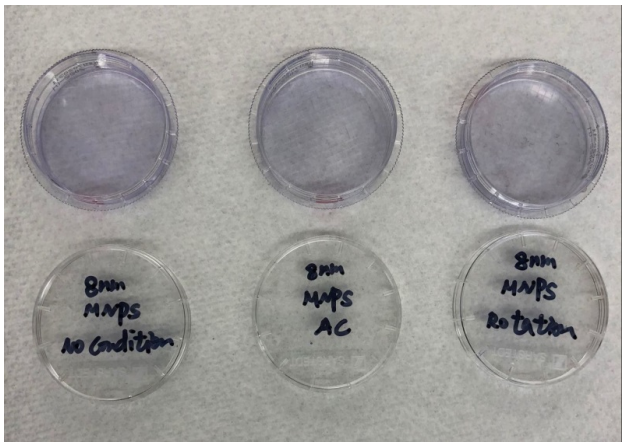

(c)

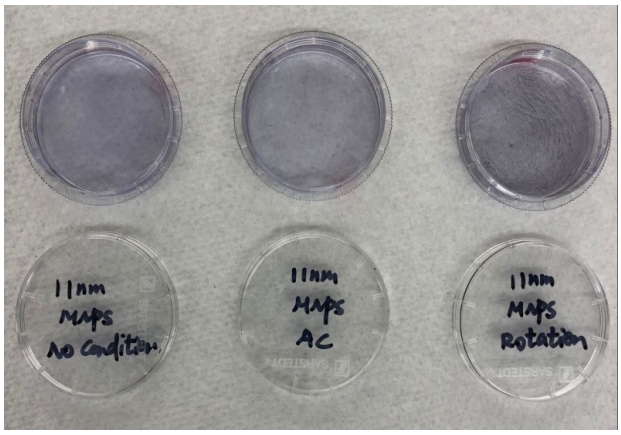

Figure 23. The crystal violet test results of (a) control MRSA biofilm; (b) biofilm after treatment with 30 mg/mL 8 nm MNPs@SiO_2; and (c) biofilm after treatment with 30 mg/mL 11 nm MNPs@SiO_2 for 15 min under no field condition, AC and rotation magnetic field

The CV results of the biofilms after exposure to the 8 nm (Figure 23b) and 11 nm (Figure 23c) MNPs under different conditions, then washed three times with 200 μL DI water were totally different than the controls. The stained colors were much lighter than both the negative and positive controls, and did not have any obvious spaces. By using the CV stain, we were able to observe a rough morphology of biofilm and that the films seemed much thinner than the controls after treatment with nanoparticles due to the very light color. This indicates the matrix might be damaged by the nanoparticles, in order to figure out the degree of biofilm matrix damage we conducted the confocal microscopy for the next.

4.2.7. Interaction Damage Effect of MNPs

Confocal laser scanning microscopy (CLSM) is an important method for the study of biofilm structure. Since its first application [116], CLSM has been widely used to improve the understanding of the biofilm architecture [117]. CLSM is a non-destructive and non-invasive method of study with the capability to provide time-resolved three-dimensional images of biofilms. In this study, as the further visualization of how nanoparticles interfere with biofilm was necessary, CLSM was performed to observe the morphology of biofilms after treatment (Control, CTAB, 11 nm MNPs, and 70 nm MNPs) for 15 min to help us understand how they interacted with biofilms (Figure 24).

As described previously, the nanoparticles could lead to biofilm dispersal and perhaps damage the matrix of biofilm. From the CLSM images, after 10 mg/mL and 30 mg/mL of 11 nm MNPs@SiO_2 treatment for 15 min, there were only bacterial cells left

(Figure 25 and Figure 26). No film was observed, and only a very few cells left for the AC and rotation conditions. To get the comparative effect between nanoparticles and biocide, we also took confocal images of biofilm after it was exposed to 100 ppm CTAB for 15 min (Figure 27), and DIC images of the control biofilm and the 100 ppm CTAB samples (Figure 28). These images show clearly that after contact with 100 ppm CTAB, the biofilm matrix obviously existed and still had a three dimension visual effect. The yellow color produced from the overlap of the green and red colors together, indicated that there were both live and dead bacteria after treatment with 100 ppm CTAB. Some spaces appeared because some cells had been killed by CTAB and washed off leaving the empty spaces.

In contrast, observation of the biofilm after treatment with 11 nm MNPs for 15 min showed that the matrix was definitely damaged and had disappeared because of the mechanical disruption. The three groups of CLSM images (control, biofilm treated with 11nm nanoparticles and CTAB), clearly indicated that the 100 ppm CTAB (a QAC biocide) did not have the ability to penetrate into the matrix and cause damage of the biofilm within 15 min, while the nanoparticles effectively overcame this difficult problem.

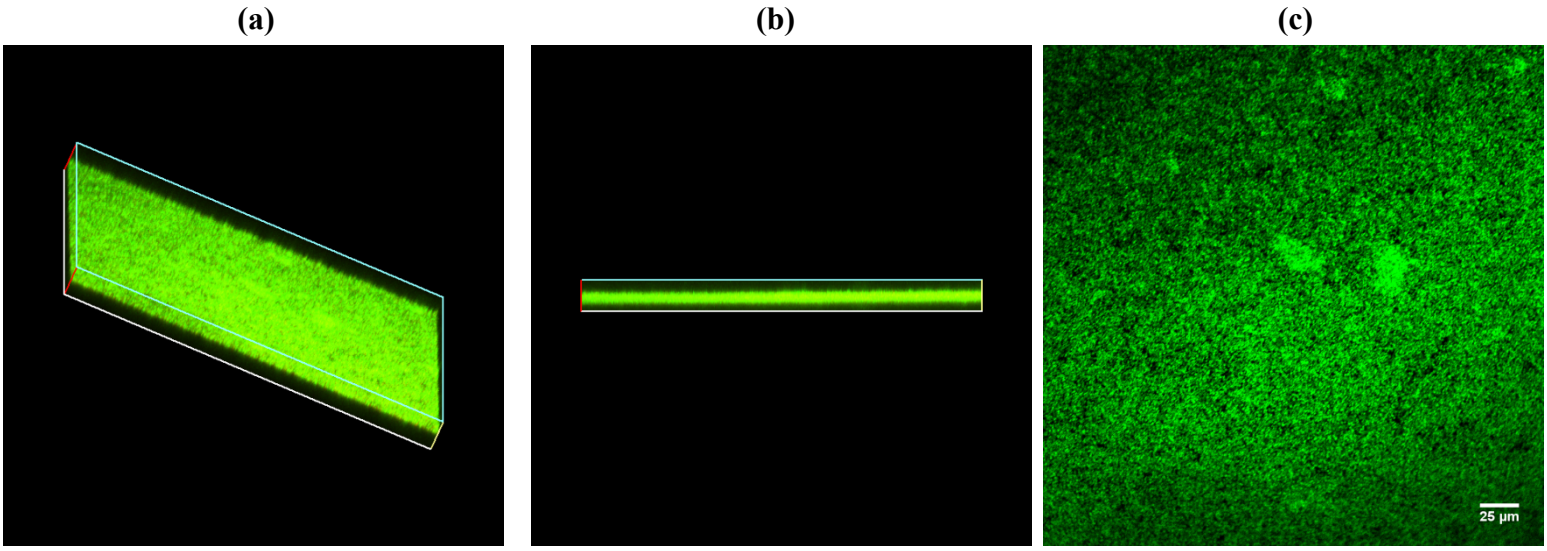

Figure 24. Three-dimensional confocal images of (a) control biofilm; (b) control biofilm cross-section. (c) Two-dimensional confocal images of control biofilm. The control biofilm was observed under 40X objective, and scanning 25 layers of 0.5 µm of each step. The total biofilm thickness is around 12.5 µm.

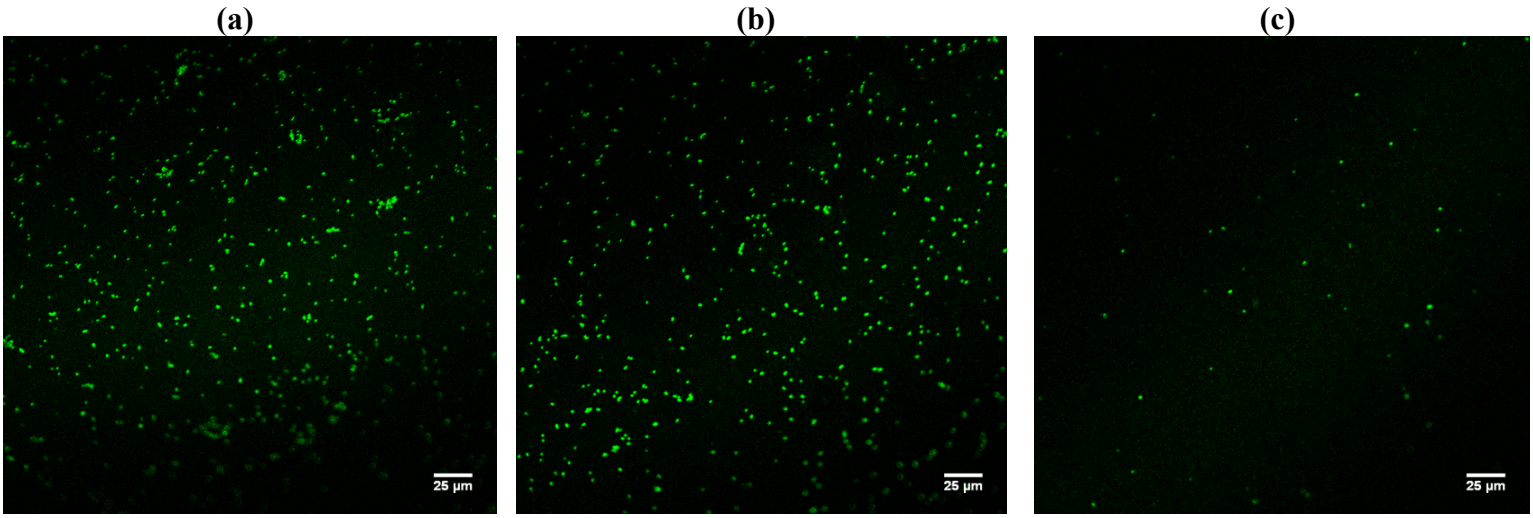

Figure 25. Two-dimensional confocal images of biofilm after treatment with 10 mg/mL 11 nm MNPs@SiO_2 under (a) no field condition; (b) AC magnetic field; and (c) rotating field. Biofilms were observed under 40X objective.

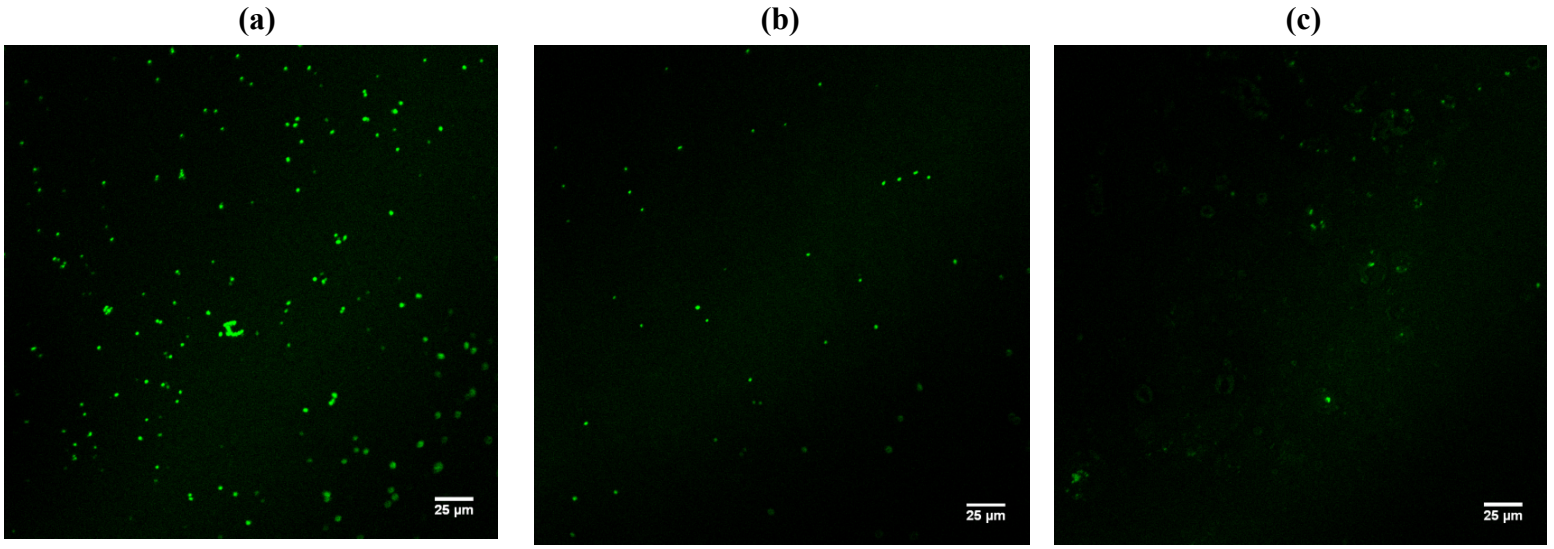

Figure 26. Two-dimensional confocal images of biofilm after treatment with 30 mg/mL 11 nm MNPs@SiO_2 under (a) no field condition; (b) AC magnetic field; and (c) rotating field. Biofilms were observed under 40X objective.

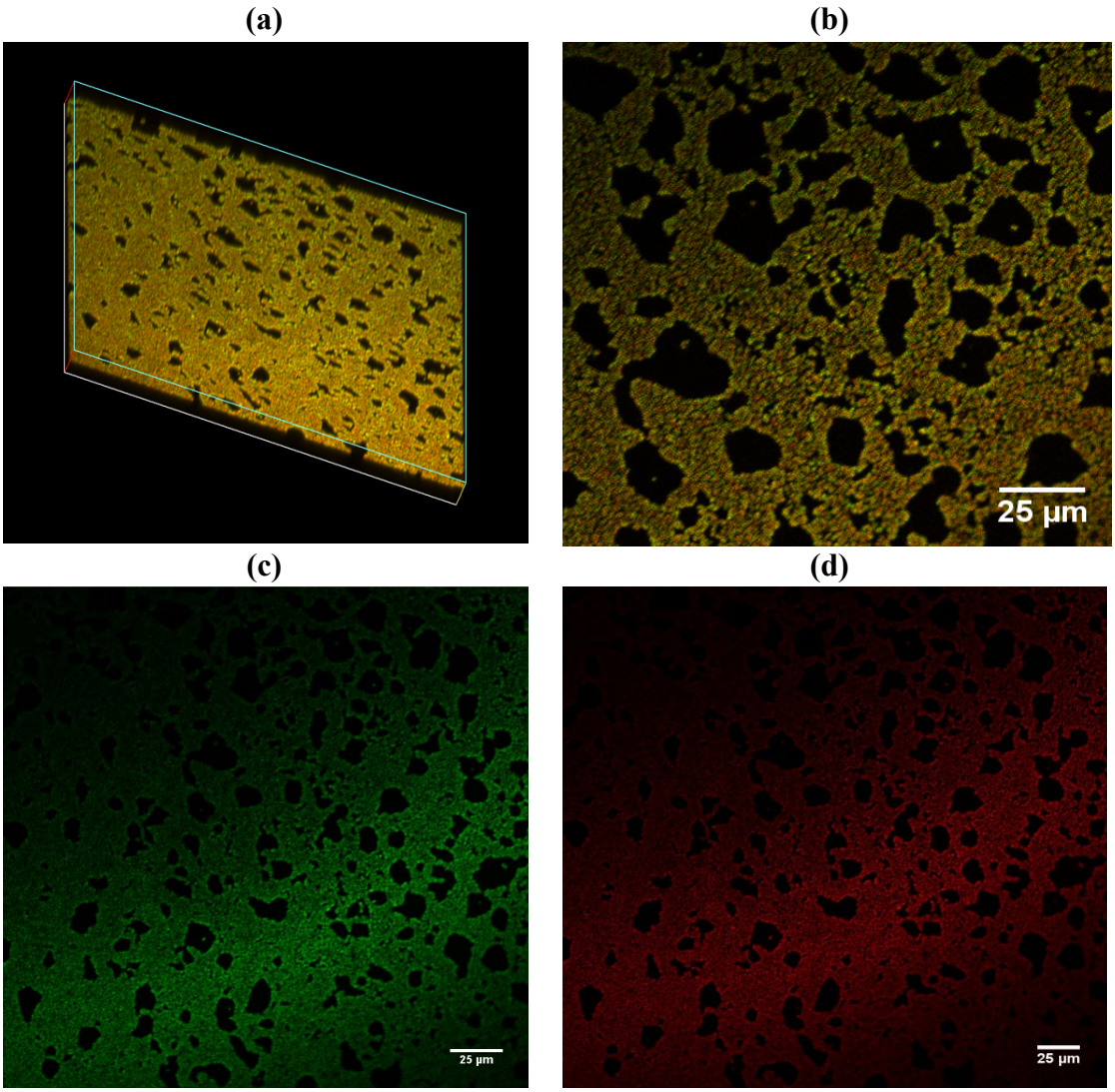

Figure 27. (a) Three-dimensional; and (b) two-dimensional confocal images of biofilm after contact with 100 ppm CTAB for 15 min; (c) the two-dimensional confocal images of live cells; and (d) the two-dimensional images of dead cells after treatment with 100 ppm CTAB for 15 min.

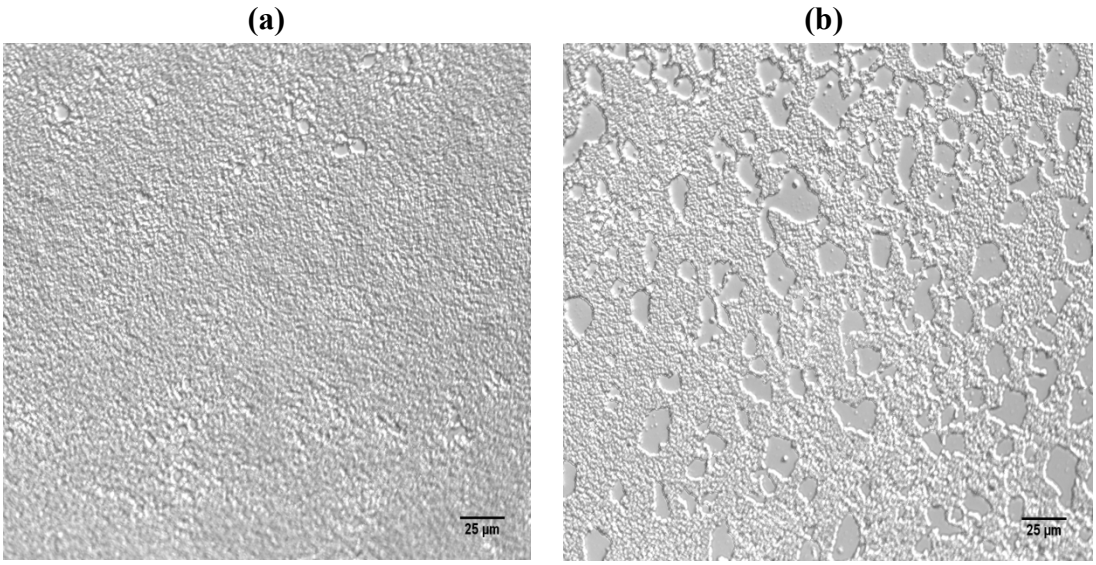

Figure 28. DIC 40X images of (a) control biofilm and (b) after treatment with 100 ppm CTAB

For further quantitative analysis, we used the ImageJ [118] software to quantify the pixels of green color cells (live cells) after 30 mg/mL 11 nm MNPs treatment, and through a series of calculations determined the bacteria number under each condition. There were 10,930 pixels; 1,692 pixels; and 1,342 pixels of live cells (green color) for no field condition, AC and rotation, respectively. The pixel shape was square; each side length was 0.31 µm, and each confocal image involved 1024 x 1024 pixels.

Therefore, after calculation, the live bacteria numbers were determined to be around 3.19×10^6 cfu; 4.94×10^5 cfu and 3.92×10^5 cfu for the no field condition, AC field, and rotation, respectively. This result of the CLSM assay was also consistent with the anti-biofilm test. For the antibiofilm test quantifying results, the live bacteria numbers were 6.40×10^5 cfu; 5.40×10^5 cfu; and 4.34×10^4 cfu for no field condition, AC, and rotation, respectively.

Following the confocal microscopy to observe the biofilms after treatment with 11 nm MNPs, we wanted to use the perspective of a three-dimensional visual to understand the gradual changes in thickness of the biofilm after treatment. Because the 11 nm nanoparticles have a strong effect, even after low concentration (10 mg/mL), the treatment damaged all the film matrices. The 8 nm particles had a very similar effect to 11 nm nanoparticles, so we chose the least effective — 70 nm nanoparticles— to determine the progression of the biofilm damage. Low (10 mg/mL), and high (30 mg/mL) concentrations of 70 nm MNPs were used to treat the biofilm.

Figure 29 and Figure 30 show the three-dimensional confocal images of biofilms after treatment with low concentration (10 mg/mL) and high concentration (30 mg/mL) of 70 nm MNPs@SiO_2 under no field condition and AC field. From these images, we can see that after treatment with these two different concentrations, biofilm particles under no field condition have no obvious difference from the control biofilms, while under AC condition, the biofilm became sparser. From the cross-sectional view, after treatment under AC field, the biofilm thickness was obviously thinner than no field condition. After contact with the high concentration nanoparticles (30 mg/mL), the biofilms looked much sparser than after contact with the low concentration. This result demonstrates that the increased concentration of 70 nm particles would have a better effect on biofilm dispersal and matrix damage. Furthermore, no matter which concentration was used, after treatment under rotation left no film (Figure 31), which means the 70 nm particles totally damaged the matrix and achieved the best effect under rotating magnetic field compared

with no field condition and AC field.

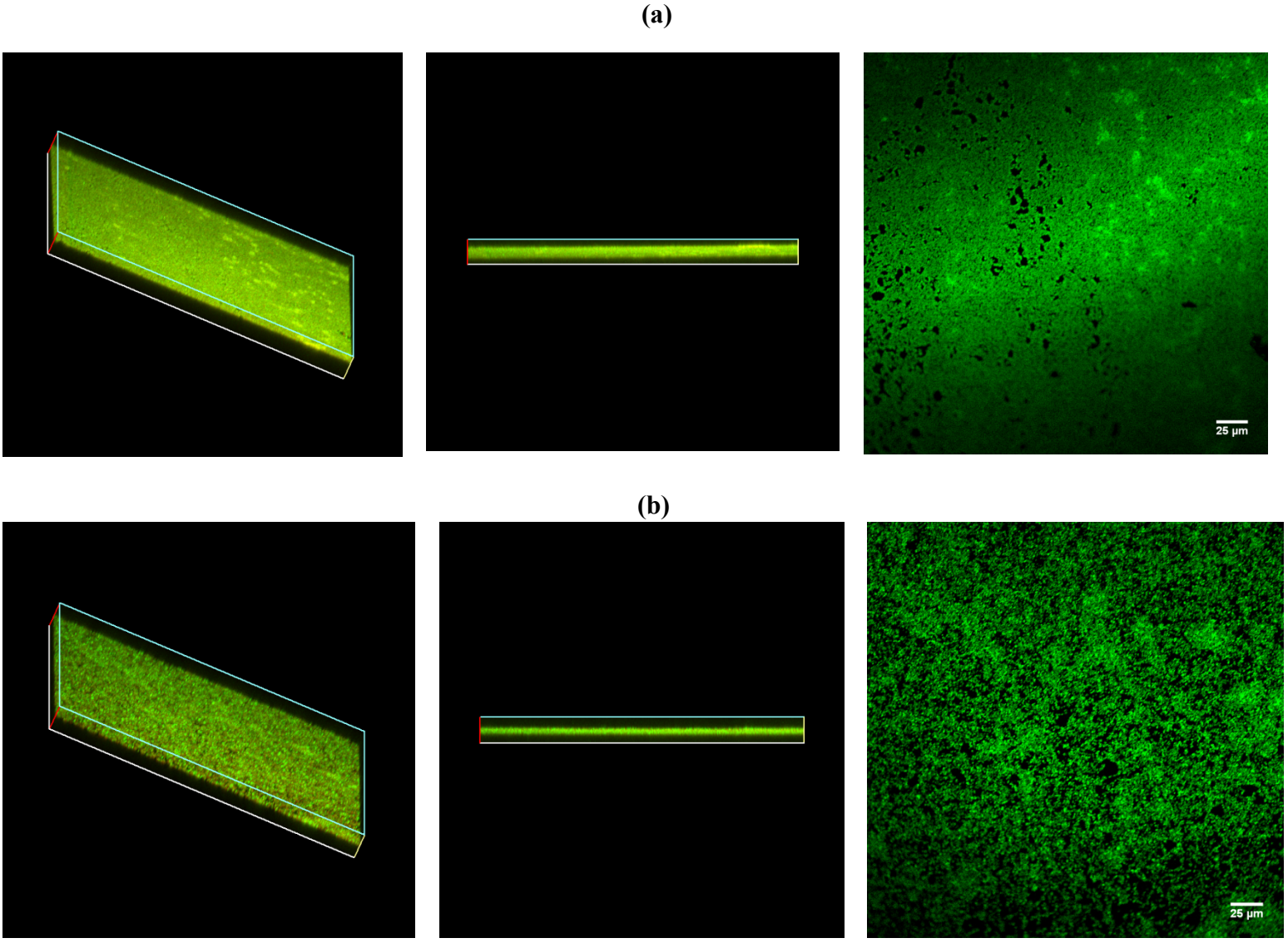

Figure 29. The three-dimensional and two-dimensional confocal laser scanning microscopy images of biofilms (a) after treatment with 10 mg/mL 70 nm MNPs under no field condition, (b) under AC magnetic field

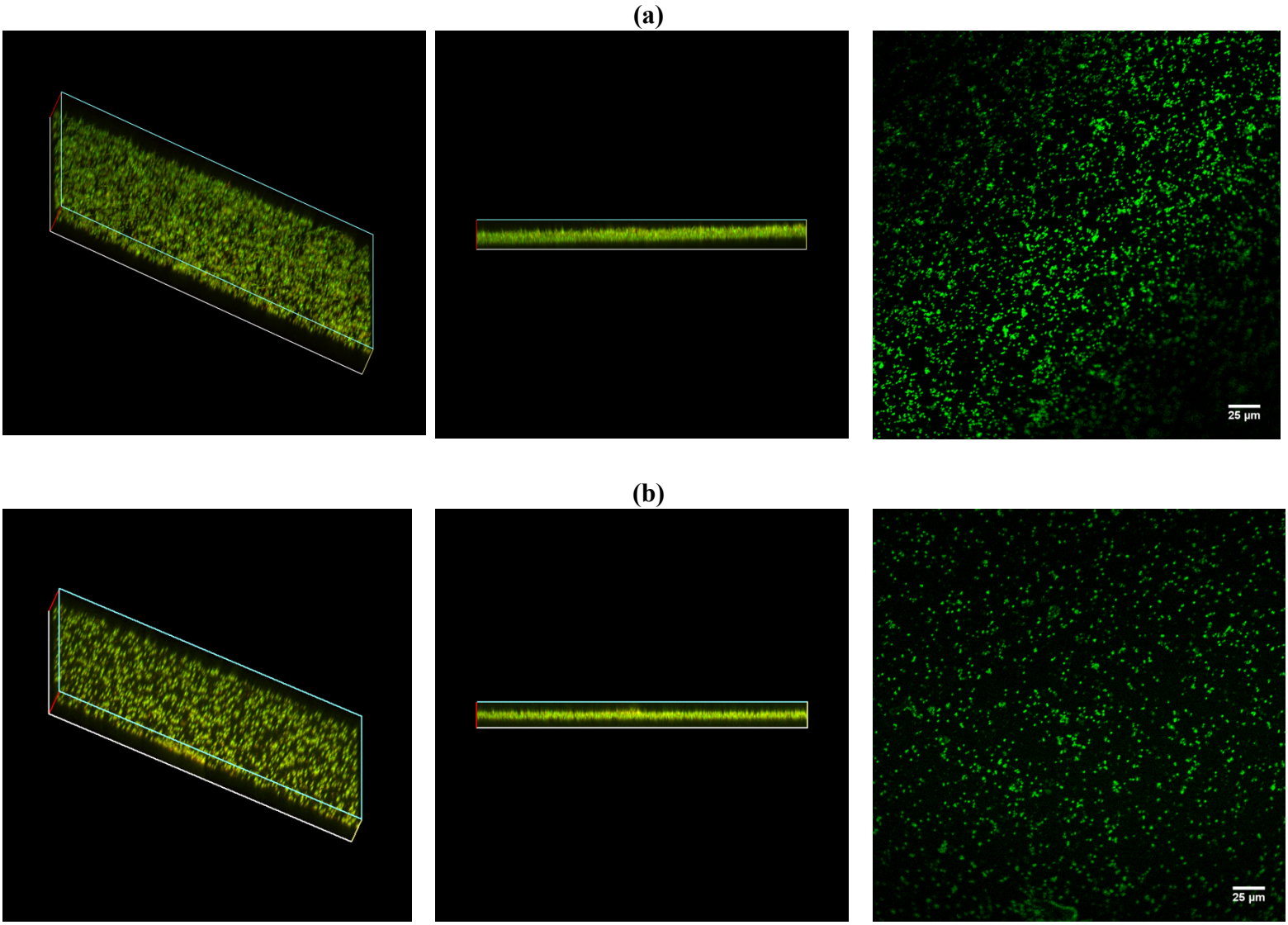

Figure 30. The three-dimensional and two-dimensional confocal laser scanning microscopy images of (a) biofilm after the treatment with 30 mg/mL 70 nm MNPs under no field condition and (b) under AC magnetic field

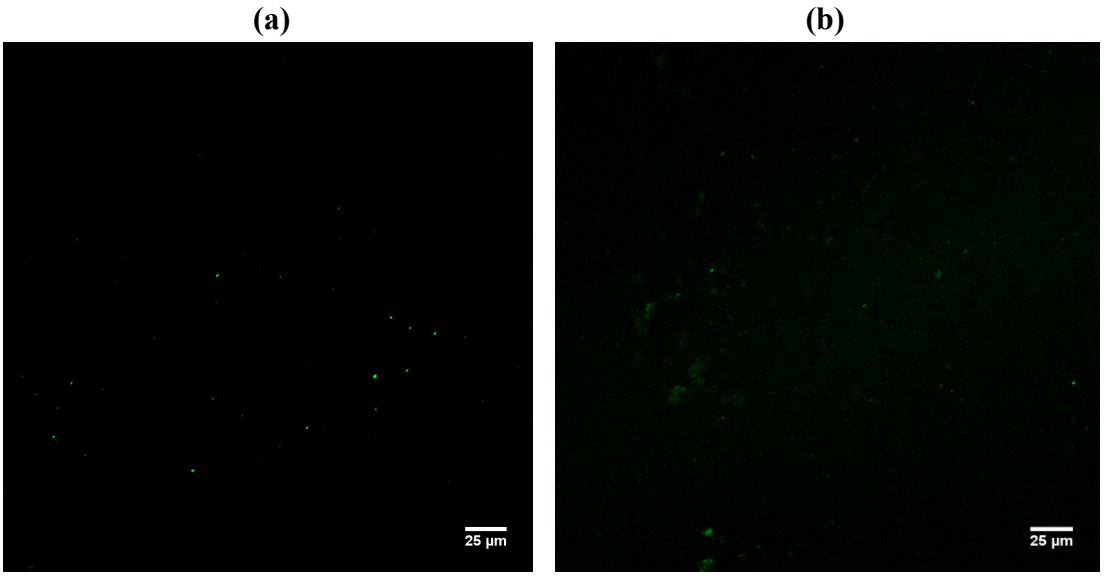

Figure 31. The two-dimensional confocal laser scanning microscopy images of (a) biofilm after treatment with 10 mg/mL and (b) 30 mg/mL 70 nm MNPs@SiO_2 under rotating magnetic field

4.2.8. The Effect of Alternating and Rotating Magnetic Field on MNPs

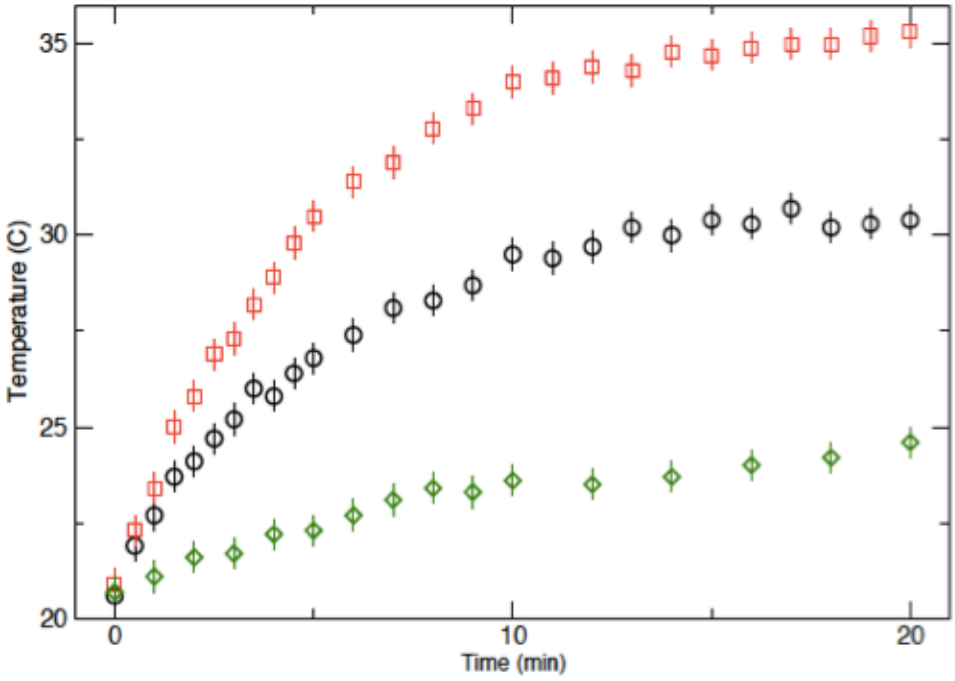

Figure 32. Heating curves of 8 nm (black circles), 11 nm (red squares) and 70 nm (green diamonds) nanoparticles in a 191 kHz, 15.8 kA/m AC magnetic field.

To determine how the alternating magnetic field helped the nanoparticles to cause biofilm dispersal, we measured the temperature curve of the AC field. Iron-oxide nanoparticles are inorganic nanomaterials with unique physical properties including high surface area to volume ratios and superparamagnetism for small size particles, which allows them to absorb the energy of an alternating magnetic field and convert it into heat. Based on this knowledge, we surmised that the iron-oxide nanoparticles acted as a heat source in the alternating magnetic field to induce a local hyperthermia effect and disperse the biofilms. The temperature changes on the biofilm were assessed by testing the heating curve of 8 nm, 11 nm and 70 nm nanoparticle solutions in AC field (Figure 32).

Hyperthermia measurements were done using a 2.4 kW Ambrell Easyheat and a FLIR AX8 infrared camera. To characterize the heating response of the nanoparticles utilized in the biofilm tests, similar conditions were utilized. The samples consisted of 30 mg/mL solutions of 8 nm, 11 nm and 70 nm nanoparticles. For each test, 2 ml of nanoparticle solution was added to a 35 mm diameter petri dish and placed in the induction coil using the same geometry as the biofilm test. Temperature measurements were acquired with respect to time while the AC magnetic field (191 kHz 15.8 kA/m) was applied. After 15 min in AC field, the solution temperature was increased to 24 °C, 30 °C and 35 °C for the 70 nm, 8 nm and 11 nm nanoparticle solutions, respectively. In order to get a comparative result, we also treated the control biofilms at 24 °C, 30 °C and 35 °C which are the exactly same temperatures as biofilms treatment with different sizes of MNPs in AC field, and collected both the treatment and washing solution to quantify

the bacteria number. The quantification results are shown in Table 9, from the result we could see that the bacteria numbers of the remaining film, treatment solution and washing solution after treatment under 24 °C, 30 °C and 35 °C were not significantly different from those of the room temperature (23 °C) control ($p > 0.05$).

Table 9. Quantified results of treatment and washing solution of control biofilms after treated under different conditions

Sample	Remaining film (cfu)	Treatment sol'n (cfu)	Washing sol'n (cfu)
RT (23 °C)	$2.1 \pm 0.2 \times 10^9$	$1.4 \pm 0.3 \times 10^8$	$6.2 \pm 0.9 \times 10^8$
24 °C	$1.8 \pm 0.4 \times 10^9$	$1.6 \pm 0.2 \times 10^8$	$6.1 \pm 1.0 \times 10^8$
30°C	$2.0 \pm 0.2 \times 10^9$	$1.6 \pm 0.2 \times 10^8$	$6.3 \pm 0.4 \times 10^8$
35°C	$2.0 \pm 0.3 \times 10^9$	$1.5 \pm 0.2 \times 10^8$	$5.9 \pm 0.8 \times 10^8$

However, when examining the correlation between the temperature increase caused by the MNPs in AC field and the quantification results of bacteria in the nanoparticles treatment solutions, in all cases we found that a higher temperature of nanoparticle solution correlated with more release of dispersal cells from the biofilm, as seen by increases in bacteria number in treatment solution. The 11 nm nanoparticles solution achieved the highest temperature and caused the most cells to detach from biofilm, as a result the 11 nm nanoparticles in AC condition showed the highest log reduction; for the same reason, the 70 nm nanoparticles had the lowest temperature as well as the lowest log reduction in AC condition. In addition, an increase of 5 °C from 30 °C to 35 °C of the biofilm surface temperature gave the 11 nm MNPs a stronger dispersal response in comparison to the 8 nm MNPs. The MNPs could cause the biofilm detachment under AC

field while simply increasing the temperature of the MRSA biofilm to 24 °C, 30 °C and 35 °C failed to lead to any detectable biofilm dispersal. We speculate that this might be because that the infrared camera only detected the temperatures of the surface of MNPs suspensions which might not accurately reflect the exact temperature of the local spot of MNPs. The monitored surface temperature (24 °C, 30 °C or 35 °C) of MNP suspensions might not be an accurate reflection of the actual temperature sensed by the biofilm and the actual temperature of biofilm treated with MNPs in AC field might much higher than that. Our nanoparticles have an ability to act as heat source and increase the MNPs solution to a quite high temperature to produce hyperthermic effect and lead to biofilm detachment. Although according to the infrared camera detection the highest temperature of MNPs system increases the solution is 35 °C, the large amount of energy transferred to the solution reveals the immediate vicinity temperature of the nanoparticles to be very high. The SLP is a measure of the instantaneous heat transfer per gram of nanoparticles. The 8 nm particles have a calculated SLP of 4.6 ± 0.5 W/g, the 11 nm particles have an SLP of 6.2 ± 0.4 W/g and the 70 nm particles is 0.8 ± 0.5 W/g. We can rearrange the general heat transfer equation, $\triangle Q/t = mc_p(\triangle T/t)$, where $\triangle Q/t$ is the heat transferred with respect to time, m and c_p are the mass and heat capacity of the Fe_3O_4 nanoparticles, and $\triangle T/t$ is the temperature increase with respect to time to SLP = $c_p \triangle T/t$ where $\triangle T/t$ is the rate of temperature increase. Using c_p = 0.65 J/g°C for Fe_3O_4 [144] the rate of temperature increases are 7.1°C/s and 9.5°C/s, for the 8 nm and 11 nm particles respectively. If these rates are constant for the first 30 s, the nanoparticles will increase

by 213 °C and 285 °C for 8 nm and 11 nm, respectively. Taken together, these data strongly suggest that the hyperthermic effect is a potent signal for biofilm dispersal. From Figure 33 we can see clearly the biofilm after treatment with 30 mg/mL of 11 nm MNPs and holding in AC field for 15 min, has significant condensation on the lid because of the increased temperature whereas no condensation was observed in the cases of no field and rotation magnetic field.

(a) **(b)**

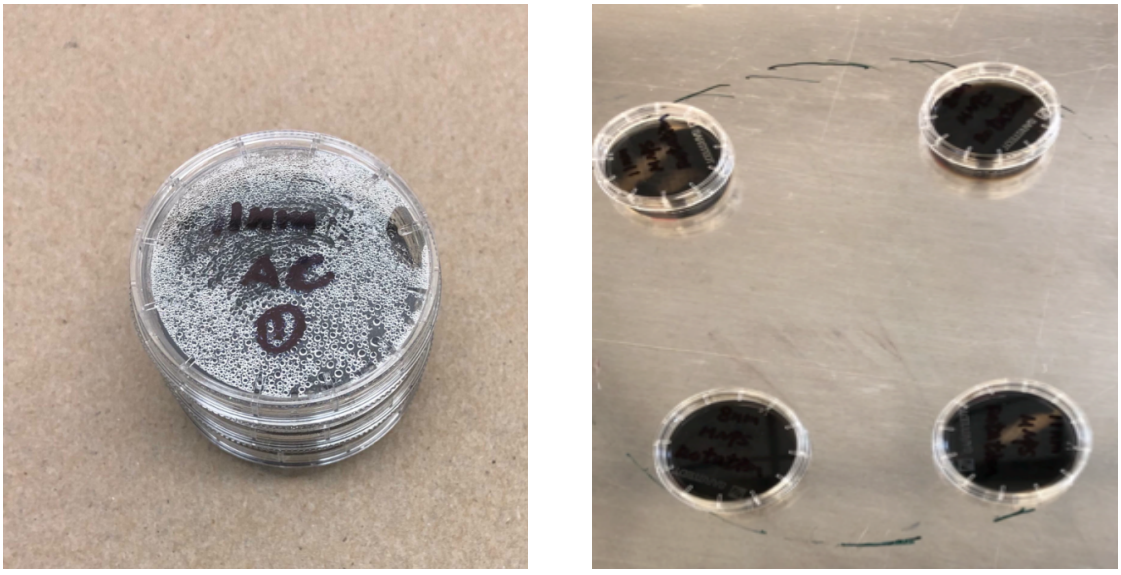

Figure 33. Photos of 30 mg/mL 11 nm MNPs solution after (a) holding in the AC field for 15 min. There was a lot of condensation on the lid because of the increased temperature, while (b) petri dishes treated with MNPs under rotation condition did not have this phenomenon.

On the other hand, compared to heating, the rotating magnetic field shows another mechanism for damaging the biofilms. Due to the nanometric size, the force generated by MNPs is smaller than the force required for disrupting key components of cells. For this study, we observed that under the rotating magnetic field the nanoparticles assembled

together and moved on the biofilm as elongated aggregates to mechanically impact on the integrate of the biofilm. Under a low frequency rotating magnetic field, these magnetic nanoparticles had a high response to the external magnetic field and generated shear stress to dramatically damage the biofilm matrix causing the dispersal of most cells.

5. Conclusions

Iron oxide nanoparticles have been widely used in biomedical research because of their unique properties, good biocompatibility, low cytotoxicity, and straightforward synthesis. One of the most common human pathogens, *Staphylococcus aureu*s, leads to many types of infection and is also known to possess an increasing ability to resist antibiotics. Thus, it is necessary to find an alternative treatment (perhaps without the use of antibiotics) for *S. aureus* infection that is directed to the site of infection, localized, and difficult for bacteria to formulate resistance. Using iron-oxide magnetic nanoparticles, a modular tool for comprehensive infection treatment including antibacterial activity, disruption of biofilms, and targeting of the infection site could be possible. However, to optimize a system for a particular use, a full understanding of the underlying mechanism is required. Small changes in size and shape of nanoparticles can have significant effect on the behavior of these systems. In our study of antibacterial tests, all the three kinds of nanoparticles 0 °C, RT and 50 °C (40 nm, 41 nm and 94 nm, respectively) were successfully coated with QACs and chlorinated. These nanoparticles presented a high efficacy of killing the Methicillin resistant *S. aureus* (MRSA) strain. Magnetic properties allowed such particles to be directed to the target side with a magnetic field, possibly after coating with some types of antimicrobial agent.

In addition, for our anti-biofilm study, the 8 nm, 11 nm, and 70 nm MNPs@SiO_2 could be used as a physical means to target biofilms with a magnetic field, allowing controlled delivery which is not possible with traditional antibiotics. The 11 nm

nanoparticles had an enhanced efficacy over 8 nm and 70 nm particles because the 70 nm nanoparticles have a much bigger size compared to the 8 nm and 11 nm particles, so it is not easy for them to penetrate into the biofilm matrix to cause damage. In the AC field, the temperature of 70 nm particle solution did not increase as high as the 8 nm and 11 nm MNP solutions. This is a reason why the 70 nm MNPs had the least effective among the three sizes of nanoparticles. However, even though the 70 nm nanoparticles did not increase to a high temperature in AC field, they produced a very good response in the rotating magnetic field. Therefore, the large size 70 nm MNPs seemed more suitable to incorporate with rotation instead of the AC field. The 11 nm and 8 nm particles are close in size and also showed a similar antimicrobial effect; however, the improved effect of the 11 nm MNPs can be attributed to enhanced magnetic and an hyperthermic responses.

As we know, the current challenge in treating biofilm is the increased resistance to antimicrobial agents of the bacteria within the biofilm structures. What's more, the EPS matrix acts as a diffusion barrier to delay the infiltration of some antimicrobial agents. Therefore, our new approach using the iron-oxide magnetic nanoparticles to treat biofilms has two advantages. Firstly, nanoparticles could penetrate the biofilm matrix and play a role as "shield breakers" to damage it. Secondly, since our nanoparticles cause only biofilm dispersal instead of killing, the method can be used over the long term as the biofilm will not increase resistance to nanoparticles as it does with antibiotics.

In summary, we have shown that under a rotating magnetic field, the action of the nanoparticles results in local mechanical damage of the biofilm matrix and effective

detachment. These aggregated MNPs produce shear tress with relatively low magnetic field for mechanical disruption of biofilm matrix. Under rotating magnetic field, nanoparticles were dragged across the biofilms and generated a viscous drag force on the film. The lower speed of the rotating magnetic field allowed the nanoparticles to increase contact time with the biofilm resulting in a high efficiency of biofilm dispersal.

Iron-oxide magnetic nanoparticles might be an ideal antimicrobial treatment, with a superior ability to cause dispersal of biofilm, and damage to the matrix, which is the most difficult problem of biofilm treatment. For the first time, this study reveals that iron-oxide magnetic nanoparticles could disperse resistant *S. aureus* biofilms, providing evidence that MNPs may be an important design component in removing the biofilm that formation on the surface of medical devices. As our antibacterial tests have shown, the iron-oxide magnetic nanoparticles coated with biocides have an excellent effect on treating the bacteria. As well, iron-oxide magnetic nanoparticles alone have interesting anti-biofilm properties, especially when coupled with a magnetic field. These properties should be explored further for removal biofilms formation on medical devices. For the next step, MNPs could be incorporated with antibiotics under a magnetic field to achieve a synergistic effect and eliminate biofilms. Moreover, the rotating magnetic field promises a way for heat sensitive antibiotics to be used instead of AC field.

In the future, the physical disruption caused by nanoparticles under a rotating magnetic field could possibly be of use in the field of cancer treatment by inhibiting cancer cell growth. This magneto-mechanical actuation approach is attractive, having

unique advantages without heating neighboring tissues [120]. Furthermore, the low frequency rotating magnetic field has no side effects and could considerably reduce the costs for instrumentation [120]. On the other hand, MNPs can generate heat to increase temperature and induce cancer cell death at the high frequency of hundreds of kHz alternating magnetic field. Currently, magnetic hyperthermia therapy is under clinical investigation for treating brain cancer and has achieved moderate therapeutic outcomes [121,122]. Therefore, the present work offers a promising strategy for use of magnetic nanoparticles in the biomedical area.

References

1. Huttner, A., Harbarth, S., Carlet, J., Cosgrove, S., Goossens, H., Holmes, A., ... & Pittet, D. (2013). Antimicrobial resistance: a global view from the 2013 World Healthcare-Associated Infections Forum. *Antimicrobial resistance and infection control*, *2*(1), 31.

2. Klevens, R. M., Morrison, M. A., Nadle, J., Petit, S., Gershman, K., Ray, S., ... & Craig, A. S. (2007). Invasive methicillin-resistant Staphylococcus aureus infections in the United States. *Jama*, *298*(15), 1763-1771.

3. Klevens, R. M., Edwards, J. R., Richards Jr, C. L., Horan, T. C., Gaynes, R. P., Pollock, D. A., & Cardo, D. M. (2007). Estimating health care-associated infections and deaths in US hospitals, 2002. *Public health reports*, *122*(2), 160-166.

4. Stone, P. W. (2009). Economic burden of healthcare-associated infections: an American perspective. *Expert review of pharmacoeconomics & outcomes research*, *9*(5), 417-422.

5. Al-Tawfiq, J. A., & Tambyah, P. A. (2014). Healthcare associated infections (HAI) perspectives. *Journal of infection and public health*, *7*(4), 339-344.

6. Gastmeier, P., Stamm-Balderjahn, S., Hansen, S., Nitzschke-Tiemann, F., Zuschneid, I., Groneberg, K., & Rüden, H. (2005). How outbreaks can contribute to prevention of nosocomial infection: analysis of 1,022 outbreaks. *Infection Control & Hospital Epidemiology*, *26*(4), 357-361.

7. Roberts, C. G. (2013). The role of biofilms in reprocessing medical devices.

American journal of infection control, *41*(5), S77-S80.

8. Donlan, R. M., & Costerton, J. W. (2002). Biofilms: survival mechanisms of clinically relevant microorganisms. *Clinical microbiology reviews*, *15*(2), 167-193.

9. Ramasamy, P., Lim, D. H., Kim, B., Lee, S. H., Lee, M. S., & Lee, J. S. (2016). All-inorganic cesium lead halide perovskite nanocrystals for photodetector applications. *Chemical communications*, *52*(10), 2067-2070.

10. Costerton, J. W., & Stewart, P. S. (2001). Battling biofilms. *Scientific American*, *285*(1), 74-81.

11. Costerton, J. W. (1999). Introduction to biofilm. *International journal of antimicrobial agents*, *11*(3), 217-221.

12. Watnick, P., & Kolter, R. (2000). Biofilm, city of microbes. *Journal of bacteriology*, *182*(10), 2675-2679.

13. Flemming, H. C., Neu, T. R., & Wozniak, D. J. (2007). The EPS matrix: the "house of biofilm cells". *Journal of bacteriology*, *189*(22), 7945-7947.

14. Flemming, H. C., & Wingender, J. (2001). Relevance of microbial extracellular polymeric substances (EPSs)-Part I: Structural and ecological aspects. *Water science and technology*, *43*(6), 1-8.

15. Flemming, H. C., Neu, T. R., & Wozniak, D. J. (2007). The EPS matrix: the "house of biofilm cells". *Journal of bacteriology*, *189*(22), 7945-7947.

16. Flemming, H. C. (1993). Biofilms and environmental protection. *Water Science and Technology*, *27*(7-8), 1-10.

17. Stoodley, P., & Lewandowski, Z. (1994). Liquid flow in biofilm systems. *Applied and environmental microbiology*, *60*(8), 2711-2716.

18. Donlan, R. M. (2002). Biofilms: microbial life on surfaces. *Emerging infectious diseases*, *8*(9), 881.

19. Renner, L. D., & Weibel, D. B. (2011). Physicochemical regulation of biofilm formation. *MRS bulletin*, *36*(5), 347-355.

20. Habash, M., & Reid, G. (1999). Microbial biofilms: their development and significance for medical device—related infections. *The Journal of Clinical Pharmacology*, *39*(9), 887-898.

21. De Veer, M. W., & Van den Bos, R. (1999). A critical review of methodology and interpretation of mirror self-recognition research in nonhuman primates. *Animal Behaviour*, *58*(3), 459-468.

22. Branda, S. S., Vik, Å., Friedman, L., & Kolter, R. (2005). Biofilms: the matrix revisited. *Trends in microbiology*, *13*(1), 20-26.

23. Flemming, B. W. (2007). The influence of grain-size analysis methods and sediment mixing on curve shapes and textural parameters: implications for sediment trend analysis. *Sedimentary Geology*, *202*(3), 425-435.

24. Hall-Stoodley, L., Costerton, J. W., & Stoodley, P. (2004). Bacterial biofilms: from the natural environment to infectious diseases. *Nature reviews microbiology*, *2*(2), 95.

25. Srey, S., Jahid, I. K., & Ha, S. D. (2013). Biofilm formation in food industries: a

food safety concern. *Food control*, *31*(2), 572-585.

26. Cherifi, T., Jacques, M., Quessy, S., & Fravalo, P. (2017). Impact of nutrient restriction on the structure of Listeria monocytogenes biofilm grown in a microfluidic system. *Frontiers in microbiology*, *8*, 864.

27. Croes, S., Deurenberg, R. H., Boumans, M. L. L., Beisser, P. S., Neef, C., & Stobberingh, E. E. (2009). Staphylococcus aureus biofilm formation at the physiologic glucose concentration depends on the S. aureus lineage. *BMC microbiology*, *9*(1), 229.

28. Goldmann, D. A., Weinstein, R. A., Wenzel, R. P., Tablan, O. C., Duma, R. J., Gaynes, R. P., ... & Burke, J. (1996). Strategies to prevent and control the emergence and spread of antimicrobial-resistant microorganisms in hospitals: a challenge to hospital leadership. *Jama*, *275*(3), 234-240.

29. Klevens, R. M., Edwards, J. R., Tenover, F. C., McDonald, L. C., Horan, T., Gaynes, R., & National Nosocomial Infections Surveillance System. (2006). Changes in the epidemiology of methicillin-resistant Staphylococcus aureus in intensive care units in US hospitals, 1992–2003. *Clinical infectious diseases*, *42*(3), 389-391.

30. Klevens, R. M., Morrison, M. A., Nadle, J., Petit, S., Gershman, K., Ray, S., ... & Craig, A. S. Active Bacterial Core surveillance (ABCs) MRSA Investigators 2007. *Invasive methicillin-resistant Staphylococcus aureus infections in the United States. JAMA*, *298*, 1763-1771.

31. Onanuga, A., & Temedie, T. C. (2011). Nasal carriage of multi-drug resistant

Staphylococcus aureus in healthy inhabitants of Amassoma in Niger delta region of Nigeria. *African health sciences*, *11*(2).

32. Sadekuzzaman, M., Yang, S., Mizan, M. F. R., & Ha, S. D. (2015). Current and recent advanced strategies for combating biofilms. *Comprehensive Reviews in Food Science and Food Safety*, *14*(4), 491-509.

33. Wimpenny, J., Manz, W., & Szewzyk, U. (2000). Heterogeneity in biofilms. *FEMS microbiology reviews*, *24*(5), 661-671.

34. Costerton, J. W., Stewart, P. S., & Greenberg, E. P. (1999). Bacterial biofilms: a common cause of persistent infections. *Science*, *284*(5418), 1318-1322.

35. Donlan, R. M., & Costerton, J. W. (2002). Biofilms: survival mechanisms of clinically relevant microorganisms. *Clinical microbiology reviews*, *15*(2), 167-193.

36. Zhou, G., Shi, Q. S., Huang, X. M., & Xie, X. B. (2015). The three bacterial lines of defense against antimicrobial agents. *International journal of molecular sciences*, *16*(9), 21711-21733.

37. Chiu, K. W., Lu, L. S., & Chiou, S. S. (2015). High-level disinfection of gastrointestinal endoscope reprocessing. *World journal of experimental medicine*, *5*(1), 33.

38. Rutala, W. A., & Weber, D. J. (2001). New disinfection and sterilization methods. *Emerging infectious diseases*, *7*(2), 348.

39. Kovaleva, J., Peters, F. T., van der Mei, H. C., & Degener, J. E. (2013). Transmission of infection by flexible gastrointestinal endoscopy and bronchoscopy.

Clinical microbiology reviews, *26*(2), 231-254.

40. Zhang, Y., Kohler, N., & Zhang, M. (2002). Surface modification of superparamagnetic magnetite nanoparticles and their intracellular uptake. *Biomaterials*, *23*(7), 1553-1561.

41. Rodrigues, L. R. (2011). Inhibition of bacterial adhesion on medical devices. In *Bacterial adhesion* (pp. 351-367). Springer, Dordrecht.

42. Makkar, R. S., & Rockne, K. J. (2003). Comparison of synthetic surfactants and biosurfactants in enhancing biodegradation of polycyclic aromatic hydrocarbons. *Environmental Toxicology and Chemistry: An International Journal*, *22*(10), 2280-2292.

43. Sharma, S. K., Mulligan, C. N., & Mudhoo, A. (2014). *Biosurfactants: research trends and applications*. CRC press.

44. Li, X., Yan, Z., & Xu, J. (2003). Quantitative variation of biofilms among strains in natural populations of Candida albicans. *Microbiology*, *149*(2), 353-362.

45. Christensen, G. D., Simpson, W. A., Younger, J. J., Baddour, L. M., Barrett, F. F., Melton, D. M., & Beachey, E. H. (1985). Adherence of coagulase-negative staphylococci to plastic tissue culture plates: a quantitative model for the adherence of staphylococci to medical devices. *Journal of clinical microbiology*, *22*(6), 996-1006.

46. Macaluso, A. (2014) Characterization of Biofilms on Medical Device Materials with Application to Reusable Surgical Instruments.

47. Welch, K., Cai, Y., & Strømme, M. (2012). A method for quantitative determination of biofilm viability. *Journal of functional biomaterials*, *3*(2), 418-431.

48. Feoktistova, M., Geserick, P., & Leverkus, M. (2016). Crystal violet assay for determining viability of cultured cells. *Cold Spring Harbor Protocols*, *2016*(4), pdb-prot087379.

49. Ruso, J. M., & Piñeiro, Á. (Eds.). (2013). *Proteins in solution and at interfaces: methods and applications in biotechnology and materials science* (Vol. 8). John Wiley & Sons.

50. Schmid, F. X. (2001). Biological macromolecules: UV−visible spectrophotometry. *e LS*.

51. Bradford, M. M. (1976). A rapid and sensitive method for the quantitation of microgram quantities of protein utilizing the principle of protein-dye binding. *Analytical biochemistry*, *72*(1-2), 248-254.

52. Thakuria, D., Schmidt, O., Mac Siúrtáin, M., Egan, D., & Doohan, F. M. (2008). Importance of DNA quality in comparative soil microbial community structure analyses. *Soil Biology and Biochemistry*, *40*(6), 1390-1403.

53. Mueller, L. N., De Brouwer, J. F., Almeida, J. S., Stal, L. J., & Xavier, J. B. (2006). Analysis of a marine phototrophic biofilm by confocal laser scanning microscopy using the new image quantification software PHLIP. *BMC ecology*, *6*(1), 1.

54. Stiefel, P., Schmidt-Emrich, S., Maniura-Weber, K., & Ren, Q. (2015). Critical

aspects of using bacterial cell viability assays with the fluorophores SYTO9 and propidium iodide. *BMC microbiology*, *15*(1), 36.

55. Ramasamy, P., Lim, D. H., Kim, B., Lee, S. H., Lee, M. S., & Lee, J. S. (2016). All-inorganic cesium lead halide perovskite nanocrystals for photodetector applications. *Chemical communications*, *52*(10), 2067-2070.

56. Laurent, S., Forge, D., Port, M., Roch, A., Robic, C., Vander Elst, L., & Muller, R. N. (2008). Magnetic iron oxide nanoparticles: synthesis, stabilization, vectorization, physicochemical characterizations, and biological applications. *Chemical reviews*, *108*(6), 2064-2110.

57. Ali, A., Hira Zafar, M. Z., ul Haq, I., Phull, A. R., Ali, J. S., & Hussain, A. (2016). Synthesis, characterization, applications, and challenges of iron oxide nanoparticles. *Nanotechnology, science and applications*, *9*, 49.

58. Wahajuddin, S. A. (2012). Superparamagnetic iron oxide nanoparticles: magnetic nanoplatforms as drug carriers. *International journal of nanomedicine*, *7*, 3445.

59. Markides, H., Rotherham, M., & El Haj, A. J. (2012). Biocompatibility and toxicity of magnetic nanoparticles in regenerative medicine. *Journal of Nanomaterials*, *2012*, 13.

60. Hasany, S. F., Ahmed, I., Rajan, J., & Rehman, A. (2012). Systematic review of the preparation techniques of iron oxide magnetic nanoparticles. *Nanoscience and Nanotechnology*, *2*(6), 148-158.

61. Akbarzadeh, A., Samiei, M., & Davaran, S. (2012). Magnetic nanoparticles:

preparation, physical properties, and applications in biomedicine. *Nanoscale research letters*, *7*(1), 144.

62. Rodriguez-Luccioni, H. L., Latorre-Esteves, M., Méndez-Vega, J., Soto, O., Rodríguez, A. R., Rinaldi, C., & Torres-Lugo, M. (2011). Enhanced reduction in cell viability by hyperthermia induced by magnetic nanoparticles. *International journal of nanomedicine*, *6*, 373.

63. Lu, A. H., Salabas, E. E., & Schüth, F. (2007). Magnetic nanoparticles: synthesis, protection, functionalization, and application. *Angewandte Chemie International Edition*, *46*(8), 1222-1244.

64. Huber, D. L. (2005). Synthesis, properties, and applications of iron nanoparticles. *Small*, *1*(5), 482-501.

65. Xu, J., Sun, J., Wang, Y., Sheng, J., Wang, F., & Sun, M. (2014). Application of iron magnetic nanoparticles in protein immobilization. *Molecules*, *19*(8), 11465-11486.

66. Maity, D., & Agrawal, D. C. (2007). Synthesis of iron oxide nanoparticles under oxidizing environment and their stabilization in aqueous and non-aqueous media. *Journal of Magnetism and Magnetic Materials*, *308*(1), 46-55.

67. Wu, W., He, Q., & Jiang, C. (2008). Magnetic iron oxide nanoparticles: synthesis and surface functionalization strategies. *Nanoscale research letters*, *3*(11), 397.

68. Xia, T., Wang, J., Wu, C., Meng, F., Shi, Z., Lian, J., ... & Meng, J. (2012). Novel complex-coprecipitation route to form high quality triethanolamine-coated Fe 3 O 4

nanocrystals: their high saturation magnetizations and excellent water treatment properties. *CrystEngComm*, *14*(18), 5741-5744.

69. Mørup, S., Hansen, M. F., & Frandsen, C. (2010). Magnetic interactions between nanoparticles. *Beilstein journal of nanotechnology*, *1*, 182.

70. Bumb, A., Brechbiel, M. W., Choyke, P. L., Fugger, L., Eggeman, A., Prabhakaran, D., ... & Dobson, P. J. (2008). Synthesis and characterization of ultra-small superparamagnetic iron oxide nanoparticles thinly coated with silica. *Nanotechnology*, *19*(33), 335601.

71. Taupitz, M., Wagner, S., Schnorr, J., Kravec, I., Pilgrimm, H., Bergmann-Fritsch, H., & Hamm, B. (2004). Phase I clinical evaluation of citrate-coated monocrystalline very small superparamagnetic iron oxide particles as a new contrast medium for magnetic resonance imaging. *Investigative radiology*, *39*(7), 394-405.

72. Wiogo, H. T., Lim, M., Bulmus, V., Yun, J., & Amal, R. (2010). Stabilization of magnetic iron oxide nanoparticles in biological media by fetal bovine serum (FBS). *Langmuir*, *27*(2), 843-850.

73. Issa, B., Obaidat, I. M., Albiss, B. A., & Haik, Y. (2013). Magnetic nanoparticles: surface effects and properties related to biomedicine applications. *International journal of molecular sciences*, *14*(11), 21266-21305.

74. Hyeon, T. (2003). Chemical synthesis of magnetic nanoparticles. *Chemical Communications*, (8), 927-934.

75. Goya, G. F., Grazu, V., & Ibarra, M. R. (2008). Magnetic nanoparticles for cancer

therapy. *Current Nanoscience*, *4*(1), 1-16.

76. Bañobre-López, M., Teijeiro, A., & Rivas, J. (2013). Magnetic nanoparticle-based hyperthermia for cancer treatment. *Reports of Practical Oncology & Radiotherapy*, *18*(6), 397-400.

77. Nowak, H. (Ed.). (2007). *Magnetism in medicine: a handbook*. John Wiley & Sons.

78. Maier-Hauff, K., Ulrich, F., Nestler, D., Niehoff, H., Wust, P., Thiesen, B., ... & Jordan, A. (2011). Efficacy and safety of intratumoral thermotherapy using magnetic iron-oxide nanoparticles combined with external beam radiotherapy on patients with recurrent glioblastoma multiforme. *Journal of neuro-oncology*, *103*(2), 317-324.

79. Hilger, I., Hergt, R., & Kaiser, W. A. (2005, February). Use of magnetic nanoparticle heating in the treatment of breast cancer. In *IEE Proceedings-Nanobiotechnology* (Vol. 152, No. 1, pp. 33-39). IET Digital Library.

80. Abenojar, E. C., Wickramasinghe, S., Bas-Concepcion, J., & Samia, A. C. S. (2016). Structural effects on the magnetic hyperthermia properties of iron oxide nanoparticles. *Progress in Natural Science: Materials International*, *26*(5), 440-448.

81. Mahmoudi, K., Bouras, A., Bozec, D., Ivkov, R., & Hadjipanayis, C. (2018). Magnetic hyperthermia therapy for the treatment of glioblastoma: a review of the therapy's history, efficacy and application in humans. *International Journal of Hyperthermia*, 1-13.

82. Boethling, R. S. (1984). Environmental fate and toxicity in wastewater treatment

of quaternary ammonium surfactants. *Water research*, *18*(9), 1061-1076.

83. Hyeon, T. (2003). Chemical synthesis of magnetic nanoparticles. *Chemical Communications*, (8), 927-934.

84. Ioannou, C. J., Hanlon, G. W., & Denyer, S. P. (2007). Action of disinfectant quaternary ammonium compounds against Staphylococcus aureus. *Antimicrobial agents and chemotherapy*, *51*(1), 296-306.

85. Johansson, I., & Somasundaran, P. (Eds.). (2007). *Handbook for Cleaning/decontamination of Surfaces*. Elsevier.

86. Fu, E., McCue, K., & Boesenberg, D. (2007). Chemical Disinfection of Hard Surfaces–Household, Industrial and Institutional Settings. In *Handbook for cleaning/decontamination of surfaces* (pp. 573-592).

87. Boyce, J. M. (2016). Modern technologies for improving cleaning and disinfection of environmental surfaces in hospitals. *Antimicrobial Resistance & Infection Control*, *5*(1), 10.

88. West, A. M., Teska, P. J., Lineback, C. B., & Oliver, H. F. (2018). Strain, disinfectant, concentration, and contact time quantitatively impact disinfectant efficacy. *Antimicrobial Resistance & Infection Control*, *7*(1), 49.

89. Codling, C. E., Maillard, J. Y., & Russell, A. D. (2003). Aspects of the antimicrobial mechanisms of action of a polyquaternium and an amidoamine. *Journal of Antimicrobial Chemotherapy*, *51*(5), 1153-1158.

90. Guan, Y., Qian, L., & Xiao, H. (2007). Novel Anti−Microbial Host−Guest

Complexes Based on Cationic β−Cyclodextrin Polymers and Triclosan/Butylparaben. *Macromolecular rapid communications*, *28*(23), 2244-2248.

91. Fraise, A. P., Lambert, P. A., & Maillard, J. Y. (Eds.). (2008). *Russell, Hugo & Ayliffe's Principles and Practice of Disinfection, Preservation & Sterilization*. John Wiley & Sons.

92. Haldar, J., Kondaiah, P., & Bhattacharya, S. (2005). Synthesis and antibacterial properties of novel hydrolyzable cationic amphiphiles. Incorporation of multiple head groups leads to impressive antibacterial activity. *Journal of medicinal chemistry*, *48*(11), 3823-3831.

93. Rawlinson, L. A. B., Ryan, S. M., Mantovani, G., Syrett, J. A., Haddleton, D. M., & Brayden, D. J. (2009). Antibacterial effects of poly (2-(dimethylamino ethyl) methacrylate) against selected gram-positive and gram-negative bacteria. *Biomacromolecules*, *11*(2), 443-453.

94. Mehta, S. K., Kumar, S., Chaudhary, S., & Bhasin, K. K. (2009). Effect of cationic surfactant head groups on synthesis, growth and agglomeration behavior of ZnS nanoparticles. *Nanoscale research letters*, *4*(10), 1197.

95. Salager, J. L. (2002). Surfactants types and uses. *FIRP booklet*, (E300A).

96. Laemmli, U. K. (1970). Cleavage of structural proteins during the assembly of the head of bacteriophage T4. *nature*, *227*(5259), 680.

97. Gottardi, W., Debabov, D., & Nagl, M. (2013). N-chloramines: a promising class of well tolerated topical antiinfectives. *Antimicrobial agents and chemotherapy*,

AAC-02132.

98. Hui, F., & Debiemme-Chouvy, C. (2013). Antimicrobial N-halamine polymers and coatings: a review of their synthesis, characterization, and applications. *Biomacromolecules*, *14*(3), 585-601.

99. Sun, X., Cao, Z., Porteous, N., & Sun, Y. (2010). Amine, melamine, and amide N-halamines as antimicrobial additives for polymers. *Industrial & engineering chemistry research*, *49*(22), 11206-11213.

100. Ahmed, A. E. S. I., Hay, J. N., Bushell, M. E., Wardell, J. N., & Cavalli, G. (2010). Macroscopic N−halamine biocidal polymeric beads. *Journal of applied polymer science*, *116*(4), 2396-2408.

101. Ahmed, A. E. S. I., Wardell, J. N., Thumser, A. E., Avignone−Rossa, C. A., Cavalli, G., Hay, J. N., & Bushell, M. E. (2011). Metabolomic profiling can differentiate between bactericidal effects of free and polymer bound halogen. *Journal of Applied Polymer Science*, *119*(2), 709-718.

102. Dong, Q., & Dong, A. (2015). Evaluation of novel antibacterial N-halamine nanoparticles prodrugs towards susceptibility of escherichia coli induced by DksA protein. *Molecules*, *20*(4), 7292-7308.

103. Cerkez, I., Kocer, H. B., Worley, S. D., Broughton, R. M., & Huang, T. S. (2012). N-halamine copolymers for biocidal coatings. *Reactive and Functional Polymers*, *72*(10), 673-679.

104. Undabeytia, T., Posada, R., Nir, S., Galindo, I., Laiz, L., Saiz-Jimenez, C.,

& Morillo, E. (2014). Removal of waterborne microorganisms by filtration using clay–polymer complexes. *Journal of hazardous materials*, *279*, 190-196.

105. Chen, Y., & Han, Q. (2011). Designing N-halamine based antibacterial surface on polymers: Fabrication, characterization, and biocidal functions. *Applied Surface Science*, *257*(14), 6034-6039.

106. Gutman, O., Natan, M., Banin, E., & Margel, S. (2014). Characterization and antibacterial properties of N-halamine-derivatized cross-linked polymethacrylamide nanoparticles. *Biomaterials*, *35*(19), 5079-5087.

107. Zhou, C. E., & Kan, C. W. (2015). Plasma-enhanced regenerable 5, 5-dimethylhydantoin (DMH) antibacterial finishing for cotton fabric. *Applied Surface Science*, *328*, 410-417.

108. Rahma, H., Nickel, R., Skoropata, E., Wroczynskyj, Y., Rutley, C., Manna, P. K., ... & Liu, S. (2016). Quaternized N-chloramine coated magnetic nanoparticles: a trifecta of superior antibacterial activity, minimal residual toxicity and rapid site removal. *RSC Advances*, *6*(70), 65837-65846.

109. Gao, J., Gu, H., & Xu, B. (2009). Multifunctional magnetic nanoparticles: design, synthesis, and biomedical applications. *Accounts of chemical research*, *42*(8), 1097-1107.

110. Baker, C., Pradhan, A., Pakstis, L., Pochan, D. J., & Shah, S. I. (2005). Synthesis and antibacterial properties of silver nanoparticles. *Journal of nanoscience and nanotechnology*, *5*(2), 244-249.

111. Coey, J. M. (2010). *Magnetism and magnetic materials*. Cambridge University Press.

112. Horie, M., & Fujita, K. (2011). Toxicity of metal oxides nanoparticles. In *Advances in molecular toxicology* (Vol. 5, pp. 145-178). Elsevier.

113. Clogston, J. D., & Patri, A. K. (2011). Zeta potential measurement. In *Characterization of nanoparticles intended for drug delivery* (pp. 63-70). Humana Press.

114. Gandhi, A. D., Vizhi, D. K., Lavanya, K., Kalpana, V. N., Rajeswari, V. D., & Babujanarthanam, R. (2017). In vitro anti-biofilm and anti-bacterial activity of Sesbania grandiflora extract against Staphylococcus aureus. *Biochemistry and biophysics reports*, *12*, 193-197.

115. Pitts, B., Hamilton, M. A., Zelver, N., & Stewart, P. S. (2003). A microtiter-plate screening method for biofilm disinfection and removal. *Journal of microbiological methods*, *54*(2), 269-276.

116. Lawrence, J. R., Korber, D. R., Hoyle, B. D., Costerton, J. W., & Caldwell, D. E. (1991). Optical sectioning of microbial biofilms. *Journal of bacteriology*, *173*(20), 6558-6567.

117. Lawrence, J. R., & Neu, T. R. (1999). [9] Confocal laser scanning microscopy for analysis of microbial biofilms. In *Methods in enzymology* (Vol. 310, pp. 131-144). Academic Press.

118. Abràmoff, M. D., Magalhães, P. J., & Ram, S. J. (2004). Image processing

with ImageJ. *Biophotonics international*, *11*(7), 36-42.

119. Nguyen, T. K., Duong, H. T., Selvanayagam, R., Boyer, C., & Barraud, N. (2015). Iron oxide nanoparticle-mediated hyperthermia stimulates dispersal in bacterial biofilms and enhances antibiotic efficacy. *Scientific reports*, *5*, 18385.

120. Shen, Y., Wu, C., Uyeda, T. Q., Plaza, G. R., Liu, B., Han, Y., ... & Cheng, Y. (2017). Elongated nanoparticle aggregates in cancer cells for mechanical destruction with low frequency rotating magnetic field. *Theranostics*, *7*(6), 1735.

121. Jordan, A., & Maier-Hauff, K. (2007). Magnetic nanoparticles for intracranial thermotherapy. *Journal of nanoscience and nanotechnology*, *7*(12), 4604-4606.

122. Van Landeghem, F. K., Maier-Hauff, K., Jordan, A., Hoffmann, K. T., Gneveckow, U., Scholz, R., ... & Von Deimling, A. (2009). Post-mortem studies in glioblastoma patients treated with thermotherapy using magnetic nanoparticles. *Biomaterials*, *30*(1), 52-57.

123. Yavuz, C. T., Mayo, J. T., William, W. Y., Prakash, A., Falkner, J. C., Yean, S., ... & Natelson, D. (2006). Low-field magnetic separation of monodisperse Fe3O4 nanocrystals. *science*, *314*(5801), 964-967.

124. Jun, Y. W., Huh, Y. M., Choi, J. S., Lee, J. H., Song, H. T., Kim, S., ... & Suh, J. S. (2005). Nanoscale size effect of magnetic nanocrystals and their utilization for cancer diagnosis via magnetic resonance imaging. *Journal of the American Chemical Society*, *127*(16), 5732-5733.

125. Iacovita, C., Florea, A., Dudric, R., Pall, E., Moldovan, A. I., Tetean, R., ... & Lucaciu, C. M. (2016). Small versus large iron oxide magnetic nanoparticles: hyperthermia and cell uptake properties. *Molecules*, *21*(10), 1357.

126. Krupovič, M., Daugelavičius, R., & Bamford, D. H. (2007). Polymyxin B induces lysis of marine pseudoalteromonads. *Antimicrobial agents and chemotherapy*, *51*(11), 3908-3914.

127. Pecci, Y., Rivardo, F., Martinotti, M. G., & Allegrone, G. (2010). LC/ESI‐MS/MS characterisation of lipopeptide biosurfactants produced by the Bacillus licheniformis V9T14 strain. *Journal of mass spectrometry*, *45*(7), 772-778.

128. Quinn, G. A., Maloy, A. P., McClean, S., Carney, B., & Slater, J. W. (2012). Lipopeptide biosurfactants from Paenibacillus polymyxa inhibit single and mixed species biofilms. *Biofouling*, *28*(10), 1151-1166.

129. Xu Z, Shao J, Li B, Yan X, Shen Q, Zhang R (2013) Contribution of Bacillomycin D in Bacillus amyloliquefaciens SQR9 to Antifungal Activity and Biofilm Formation. Appl Environ Microbiol 79:808–815.

130. Rivardo F, Turner RJ, Allegrone G, Ceri H, Martinotti MG (2009) Antiadhesion activity of two biosurfactants produced by Bacillus spp. prevents biofilm formation of human bacterial pathogens. Appl Microbiol Biotechnol 83:541–553.

131. Kuiper I, Lagendijk EL, Pickford R, Derrick JP, Lamers GEM, Thomas-Oates JE, Lugtenberg BJJ, Bloemberg GV (2004) Characterization of two

Pseudomonas putida lipopeptide biosurfactants, putisolvin I and II, which inhibit biofilm formation and break down existing biofilms. Mol Microbiol 51:97–113.

132. F Sperandio, F., Huang, Y. Y., & R Hamblin, M. (2013). Antimicrobial photodynamic therapy to kill Gram-negative bacteria. *Recent patents on anti-infective drug discovery*, *8*(2), 108-120.

133. Dai T, Gupta A, Huang Y-Y, Yin R, Murray CK, Vrahas MS et al. (2013b). Blue light rescues mice from potentially fatal Pseudomonas aeruginosa burn infection: efficacy, safety, and mechanism of action. Antimicrob Agents Chemother 57: 1238–1245.

134. Mulvey M a, Schilling JD, Martinez JJ, Hultgren SJ (2000). From the cover: bad bugs and beleaguered bladders: interplay between uropathogenic Escherichia coli and innate host defenses. Proc Natl Acad Sci 97: 8829–8835.

135. Enwemeka CS, Williams D, Enwemeka SK, Hollosi S, Yens D (2009). Blue 470-nm light kills methicillin-resistant Staphylococcus aureus (MRSA) in vitro. Photomed Laser Surg 27: 221–226.

136. Maclean M, MacGregor SJ, Anderson JG, Woolsey G (2009). Inactivation of bacterial pathogens following exposure to light from a 405-nanometer light-emitting diode array. Appl Environ Microbiol 75: 1932–1937.

137. Halstead FD, Thwaite JE, Burt R, Laws TR, Raguse M, Moeller R et al. (2016). Antibacterial activity of blue light against nosocomial wound pathogens growing planktonically and as mature biofilms. Appl Environ Microbiol 82: 4006–4016.

138. Hughes, G., & Webber, M. A. (2017). Novel approaches to the treatment of

bacterial biofilm infections. *British Journal of Pharmacology*, *174*(14), 2237-2246.

139. Kalishwaralal K, BarathManiKanth S, Pandian SRK, Deepak V, Gurunathan S (2010) Silver nanoparticles impede the biofilm formation by *Pseudomonas aeruginosa* and *Staphylococcus epidermidis*. Colloids Surf, B 79:340–344.

140. Coey, J. M. (2010). *Magnetism and magnetic materials*. Cambridge University Press.

141. Yeates, C., Gillings, M. R., Davison, A. D., Altavilla, N., & Veal, D. A. (1998). Methods for microbial DNA extraction from soil for PCR amplification. *Biological procedures online*, *1*(1), 40.

142. Zhang, X. F., Liu, Z. G., Shen, W., & Gurunathan, S. (2016). Silver nanoparticles: synthesis, characterization, properties, applications, and therapeutic approaches. *International journal of molecular sciences*, *17*(9), 1534.

143. Schindelin, J., Arganda-Carreras, I., Frise, E., Kaynig, V., Longair, M., Pietzsch, T., ... & Tinevez, J. Y. (2012). Fiji: an open-source platform for biological-image analysis. *Nature methods*, *9*(7), 676.

144. Jr. Chase, M.W. NIST-JANAF themochemical tables, fourth edition, 1998.

145. Rueden, C. T., Schindelin, J., Hiner, M. C., DeZonia, B. E., Walter, A. E., Arena, E. T., & Eliceiri, K. W. (2017). ImageJ2: ImageJ for the next generation of scientific image data. *BMC bioinformatics*, *18*(1), 529.